FERMILAB-THESIS-2017-01

Electron Neutrino Appearance in the NOνA Experiment

Ji Liu

Hainan, China

Master of Science, College of William and Mary, 2010
Bachelor of Physics, University of Science and Technology of China, 2009

A Dissertation presented to the Graduate Faculty
of the College of William and Mary in Candidacy for the Degree of
Doctor of Philosophy

Department of Physics

The College of William and Mary
January 2017

Operated by Fermi Research Alliance, LLC under Contract No. DE-AC02-07CH11359 with the United States Department of Energy

©2017
Ji Liu
All rights reserved.

APPROVAL PAGE

This Dissertation is submitted in partial fulfillment of
the requirements for the degree of

Doctor of Philosophy

Ji Liu

Approved by the Committee, November, 2016

Committee Chair
Associate Professor Patricia Vahle, Physics
The College of William and Mary

Professor Jeff Nelson, Physics
The College of William and Mary

Professor Todd Averett, Physics
The College of William and Mary

Assistant Professor Justin Stevens, Physics
The College of William and Mary

Associate Professor Robert Craig Group, Physics
University of Virginia

ABSTRACT

The NuMI Off-Axis ν_e Appearance (NOνA) experiment is a long baseline, off-axis neutrino oscillation experiment. It is designed to search for oscillations of ν_μ to ν_e by comparing measurements of the NuMI beam composition in two detectors. These two detectors are functionally identical, nearly fully-active liquid-scintillator tracking calorimeters and located at two points along the beam line to observe the neutrinos. The Near Detector (ND), situated 1 km away from the proton target at Fermilab, measures neutrinos prior to oscillation. Then the Far Detector (FD), located 810 km away at Ash River, Minnesota, measures the neutrinos after they have traveled and potentially oscillated. The neutrino beam is generated at Fermi National Accelerator Laboratory in Batavia, Illinois by the Neutrinos at the Main Injector (NuMI) facility.

By observing the $\nu_\mu \rightarrow \nu_e$ oscillation, NOνA is capable of measuring the neutrino mass hierarchy, CP violation and the octant of mixing angle θ_{23}. This thesis presents the first measurement of ν_e appearance in the NOνA detectors with 3.52×10^{20} protons-on-target (POT) data accumulated from February 2014 till May 2015. In this analysis the primary ν_e CC particle selection LID observes 6 ν_e like events in the far detector with a background prediction of 0.99 ± 0.11 (syst.), which corresponds to a 3.3σ excess over the no-oscillation hypothesis. This results disfavors $0.1\pi < \delta_{cp} < 0.5\pi$ in the inverted mass hierarchy at 90% C.L with the reactor constrain on θ_{13}.

TABLE OF CONTENTS

Acknowledgments vi

Dedication vii

List of Tables viii

List of Figures xi

CHAPTER

1 The Physics of Neutrinos 1
1.1 A Brief Experimental History of Neutrinos 1
  1.1.1 Discovery of Neutrinos 1
  1.1.2 Neutrino Oscillation 4
1.2 Neutrinos in the Standard Model 7
  1.2.1 Basic Ingredients of the Standard Model 7
  1.2.2 Weak Force and Interactions 11
  1.2.3 Neutrino Mass in the Standard Model 14
1.3 Neutrino Oscillations 16
  1.3.1 Three-Flavor Neutrino Oscillations 19
  1.3.2 Two-Flavor Neutrino Oscillations 23
  1.3.3 Neutrino Oscillations in Matter 24

1.4 Neutrino Oscillations Experiments 27

1.4.1 Reactor Antineutrino Experiments 27

1.4.2 Accelerator Neutrino Experiments 29

1.5 Summary and Current Status 30

2 The NOνA Experiment 32

2.1 NOνA Overview and Physics goals 32

2.2 The NuMI Beamline 34

2.2.1 Basic Principle 35

2.2.2 The Target 36

2.2.3 Electromagnetic Focusing Horns 39

2.2.4 Decay Volume and Absorber 40

2.2.5 NuMI Upgrade 41

2.3 Off-Axis Features 42

3 The NOνA Detector 45

3.1 The NOνA Detector Design 45

3.1.1 The Basic NOνA Detector Element 47

3.1.2 Liquid Scintillator 48

3.1.3 Wavelength-Shifting Fiber 49

3.1.4 Photodetector and Electronics 49

3.1.5 PVC Modules 54

3.2 Assembly of NOνA Detectors 57

4 Monte Carlo Simulation 63
4.1 NOνA Simulation Chain 63
4.2 Neutrino Interaction Physics Models in GENIE 65
  4.2.1 Cross Section Model 66
  4.2.2 Neutrino-induced Hadron Production 68
  4.2.3 Intranuclear Hadron Transport 68
  4.2.4 Nuclear Physics Model 70

5 Calibration and Event Reconstruction 71
5.1 Calibration 71
  5.1.1 Attenuation Calibration 73
  5.1.2 Absolute Energy Calibration 75
  5.1.3 Timing Calibration 77
5.2 Reconstruction 77
  5.2.1 Slicer4D 78
  5.2.2 Hough Transform 81
  5.2.3 Elastic Arm Vertex Finding 84
  5.2.4 Fuzzy K-Means Algorithm 86

6 ν_e Event Selection 89
6.1 NOνA Event Topologies 90
6.2 Data Quality Selection 90
  6.2.1 Beam Quality 91

6.2.2 Subrun Data Quality 92
6.3 ν_e Event Selection 94
6.3.1 Reconstruction Quality Cuts 95
6.3.2 Containment Cuts 96
6.3.3 Cosmic Ray Rejection for Far Detector 99
6.3.4 Preselection Cuts 100
6.4 ν_e Particle Identification 102

7 ν_e Appearance Analysis 106
7.1 First Measurement Data 106
7.2 Data vs. MC Comparisons 108
7.2.1 ND Data vs. MC Comparison 109
7.2.2 FD Data vs. MC Comparison 114
7.3 Decomposition 117
7.4 Extrapolation 118
7.5 Far Detector Background and Signal Prediction 122

8 Systematics 126
8.1 Beam Systematic Uncertainties 127
8.2 Scintillator Saturartion Systematic Uncertainties 130
8.3 Calibration Systematic Uncertainties 131
8.4 Light Level Systematic Uncertainties 135
8.5 Neutrino Interaction Systematic Uncertainties 137

8.6 Containment 152

8.7 Rock Contamination 153

8.8 Decomposition 154

8.9 Alignment 155

8.10 Data and Monte Carlo Statistics 156

8.11 Normalization 157

8.12 Summary 157

9 Results 159

9.1 Sideband Study 159

9.2 NOνA ν_e Appearance Result 160

  9.2.1 ν_e Appearance Candidates 161

  9.2.2 Confidence Interval 171

9.3 Conclusion 178

BIBLIOGRAPHY 179

ACKNOWLEDGMENTS

First and foremost I want to thank my advisor Patricia Vahle. For your guidance and mentorship through the whole journey of my Ph.D. For your enthusiasm and knowledge to neutrino physics that benefited a lot to both my study and this thesis. For your patient and support during the past 7 years when I tried to balance my research and personal life. I'm truly grateful to have you as my Ph.D advisor.

I want to thank Professor Jeff Nelson, who introduced me to the Neutrino group of William and Mary and has been one of my committee for every annual review. Thank you for all your suggestions and ideas through all these years.

I want to thank the other members of my graduate committee: Todd Averett, Robert Craig Group and Justin Stevens, for your time and effort to review my thesis and give valuable suggestions.

I want to thank all the members in the NOνA collaboration, who has been doing an excellent job in putting together the detectors and collecting data. Especially I want to thank the ν_e appearance analysis group, this thesis would not be possible without the contribution from each group member. The group conveners Patricia Vahle and Mayly Sanchez, thank you for your guidance and valuable suggestions. All the members in the ν_e group, including but not limit to: Alex Radovic, Chris Backhouse, Evan Niner, Tian Xin, Kanika Sachdev, Hongyue Duyang, Jianming Bian, Erika Catano-Mur, and Xuebing Bu, thank you for all the discussion and help during this analysis.

I also would like to thank all the members in the Neutrino group of William and Mary: Patricia Vahle, Jeff Nelson, Mike Kordosky, Alex Radovic, Alena Devan, Anne Norrick, Marco Colo, Dun Zhang and Leonidas Aliaga-Soplin. Thank you for all the good time that we work and travel together.

Above all, I would like to extend a heartfelt thanks to my family. Thank you, mom and dad, for raising me up with all your love and supporting all my decisions. Lastly, thank you, my dearest husband Siyuan, for your love and encouragement, for always being there for me every step through this journey.

To My Parents

List of Tables

1.1 A summary of the 12 fermions of the Standard Model for Leptons (left) and Quarks (right). The charge is measured in terms of the electron charge. The approximate mass of each fermion as obtained from [1] is shown in MeV. Note that the uncertainty in the mass of each quark is quite large. The absolute mass of the neutrinos is still unknown [2]. 9

1.2 The 5 bosons of the Standard Model and the interactions that they mediate [2]. 10

1.3 Current experimental measurements based on the 3-neutrino mixing scheme, taken from [2]. 31

3.1 The composition of NOvA liquid scintillator [3]. 48

7.1 ν_e selection performance and efficiencies in the Near detector for both MC and data. MC is normalized to the data POT 1.66×10^{20}. 110

7.2 The FD extrapolation predicted result for signal and background components using different particle selectors (LID and LEM). The FD MC event counts are also listed for comparison. The numbers are normalized to 3.45×10^{20} POT to agree with the FD first analysis exposure. 123

8.1 Percentage difference between nominal and each systematically modified FD prediction for signal and background after LID or LEM selection for each beam related systematic uncertainty. The last row corresponds to the quadrature sum of all errors in the table. 128

8.2 Percentage difference between the nominal and the Birks-Chou systematically modified FD predictions for signal and background after LID or LEM selection. 131

8.3 Calibration systematic error relative change from nominal for the signal and background components of LEM and LID selections. 137

8.4 Percentage uncertainties for neutrino interaction systematics for each GENIE reweight knob and the quadrature total. 151

8.5 Percentage difference of Far Detector predicted events rate for LID and LEM selection to study the effect of containment. Eight sets of extrapolation is performed separately different geographic regions of the Near Detector. 152

8.6 Percentage difference of the extrapolated prediction of FD events using ND MC without rock neutrino interactions compared to nominal for both LID and LEM selection. 154

8.7 Percentage difference compared to nominal of FD extrapolated prediction events in each component for LID and LEM selection. Where the difference between data and MC are assigned entirely to each component ($\nu_e CC$, $\nu_\mu CC$, or NC) alternatively to make a shifted FD extrapolation. 155

8.8 Percentage difference of the Far detector extrapolated event prediction for LID and LEM selection using the mis-aligned geometry MC sample. 156

8.9 Statistical error on extrapolation of background components. 156

8.10 List of systematic uncertainties on the background and signal prediction for events selected by LID or LEM selector. The last row corresponds to the quadrature sum of all errors in the table. 158

9.1 Comparison for the number of events between FD prediction and measurement for events passing the sideband low PID cut [4]. 160

9.2 Summary of oscillation parameters used (for normal hierarchy assumption) in the first ν_e appearance analysis of NOνA. 172

List of Figures

1.1 Summary of the deficit in atmospheric muon neutrino rates compared to electron neutrinos observed in various experiments [5]. 5

1.2 The Standard Model of elementary particles, with the three generations of Quarks and Leptons, gauge bosons in the fourth column, and the Higgs boson in the fifth [6]. 9

1.3 Feynman diagrams for the possible weak interactions of neutrino: *Left:* A charged current interaction where a neutrino of flavor l interacts with a nucleon, exchanging a charged W boson and producing a lepton of type l. *Right:* A neutral current interaction where a neutrino of flavor l scatters off a nucleon, exchanging a neutral Z^0 boson. 13

1.4 Existing muon neutrino (left) and antineutrino (right) charged-current cross section measurements [7] and predictions [8] as a function of neutrino energy. The contributing processes in this energy region include quasi-elastic (QE) scattering, resonance production (RES), and deep inelastic scattering (DIS). The error bars in the intermediate energy range reflect the uncertainties in these cross sections (typically $10 \sim 40\%$, depending on the channel). Image taken from [9]. 14

1.5 Feynman diagrams for the three possible types of charged current interactions: *Left:* quasi–elastic scattering (QE); *Middle:* resonant pion production (RES); *Right:* deep inelastic stattering (DIS). 14

1.6 Schematic of the permitted mass orderings in the neutrino sector. The diagram on the left denotes the *normal hierarchy*, while the one on the right denotes the *inverted hierarchy*. The colors represent the approximate flavor compositions as a function of the CP phase δ_{cp} of each mass eigenstate [10]. 22

1.7 NOνA ν_e Appearance Probability 24

1.8 Coherent forward scattering diagrams for neutrinos going through matter. The charged current (CC) process (left) can only occur for ν_e whereas neutral current (NC) scattering affects all flavors ν_α equally. This introduces an additional potential to the ν_e propagation Hamiltonian. 25

2.1 Location of the two NOνA detectors. The Near Detector is located at Fermilab, while the Far Detector sits 810 km away at Ash River, Minnesota. 33

2.2 Layout of the NuMI beam facility [11]. 35

2.3 The major components of the NuMI beamline. 120 GeV protons extracted from the Main Injector are incident from the left hand side and hit the target. Secondary mesons are focused by the horns and subsequently decay in the decay pipe producing ν_μ. The remaining hadrons are absorbed at the end of the pipe [12]. 36

2.4 Longitudinal Cross-Section of the NuMI Target and the Target Canister [13]. 37

2.5 Horizontal Cross-Section of the NuMI Target and the Target Canister [13]. 38

2.6 Schematic view of the NuMI focusing horns which are pulsed in “forward” mode. Hadrons produced by the NuMI target are focused by these pair of magnetic horns, the relative position of which can be adjusted to change the energy profile of the beam [14]. 39

2.7 The total neutrino flux at a given angle as a function of parent pion energy. The NOνA site is at 14 mrad [13]. 43

2.8 The total neutrino flux at a given angle as a function of parent pion energy. The NOνA site is at 14 mrad [13]. 44

2.9 Simulated energy spectrum in the NOνA far detector for different event components: beam and signal ν_eCC , ν_μCC and NC. 44

3.1 The location of the two NOνA detectors. The NuMI beam created at Fermilab travels 810 km through the Earth and reaches the Far detector in Minnesota. The Near detector is located near the source of the NuMI beamline to measure the initial properties of the beam [15]. 46

3.2 A PVC cell of dimensions (W, D, L) containing liquid scintillator and a wavelength-shifting fiber (green). A charged particle incident on the front face produces light (blue line) that bounces off the cell walls until absorbed by the fiber. The fiber routes the light to the end of the APD to the optical read out [13]. 47

3.3 a)The ends of 32 wavelength-shifting fibers at the end of scinillation cells to interface with an APD. b) Front face of an APD that will be pressed against the fiber ends [13]. 50

3.4 The quantum efficiencies of the APDs (magenta) and PMTs (blue) are shown in comparison to the average detected wavelength as fiber length increases [13]. 51

3.5 Schematic of the APD module and the Front End Board (FEB) showing the major components [13]. 51

3.6 Architecture of NOνA Data acquisition system (DAQ) [13]. 53

3.7 Drawing of the NOνA rigid PVC extrusion. 54

3.8 Cells in adjacent planes are orthogonally rotated with respect to one another. Figure from [16] 55

3.9 Schematic of NOνA extrusion module. It is constructed from two side by side 16 cell PVC extrusions and capped at both ends to contain the liquid scintillator. The manifold end also routes the 64 fiber ends to a cookie, which couples to the avalanche photodiode array and associated electronics [13]. 56

3.10 There are two functionally identical NOνA detectors in the NOνA experiment: the Far Detector at Ash River, and the Near Detector at Fermilab. The diagram shows the relative sizes of the two detectors. 57

3.11 NOνA Far Detector (courtesy of Fermilab Visual Media Services). 59

3.12 A schematic view of the NOνA Near Detector. A) 3×3 module active region. B) 3×2 module muon catcher region. C) Electronics rack alcove. D) Catwalks. E) Movable access platform [17]. 61

3.13 NOνA Near Detector (courtesy of Fermilab Visual Media Services). 62

4.1 Steps in simulation chain for the NOνA experiment. 64

4.2 Simulated invariant mass distribution of inelastic events in the MINOS Near Detector using the NuMI muon neutrino beam. The shaded area shows the resonance contribution for which a different hadronization model (Rein-Sehgal) is employed [18]. 69

5.1 Selection of tri-cells associated with a track. The dark red cell is a tricell because its neighbors are triggered by the same cosmic ray. 73

5.2 Example attenuation fit for Near detector (left) and Far detector (right) using cosmic-ray data of a channel with deviations from an ideal shape, and the LOWESS fit through the residuals [19]. 75

5.3 Stopping power ($-dE/dx$) for positive muons in copper [2]. 76

5.4 Distribution for PECorr/cm vs. distance from the track end from Far detector cosmic-ray data. It is used to calculate the absolute energy calibration factor. 76

5.5 Far detector simulation showing the event display with 550 μs readout window before (top plot) and after (bottom plot) slicer4D reconstruction. In each plot the top and bottom panel respectively represent the XZ and YZ views of the detector. Different colors indicate different timing of the hits. For the bottom plot after slicing, the bold lines shows the clusters of hits that the slicer constructed. 80

5.6 2D distribution of completeness vs. purity of the Slicer4D algorithm. For Near detector (left), the model is tuned on rock-interation neutrino data. While for Far detector (right), it is tuned on cosmic-ray data. 81

5.7 The first iteration of the Hough transform shows in the event display (left) and the corresponding Hough map (right). Two peaks are clearly formed in the map [20]. 82

5.8 The second iteration of the hough reconstruction after removing the hits associated with the first iteration in which the noise is drastically reduced [20]. 83

5.9 Left: the perpendicular distance from the first Hough line to the true vertex with an average 4 cm for $\nu_\mu CC$, 2.7 cm for $\nu_e CC$ and 6.7 cm for NC. Right: Dot Product with the first Hough line and the best matched MC particle trajectory [20]. 83

5.10 Event display of a typical ν_e CC event with a electron shower. The outlines show the FuzzyK reconstructed prongs. 88

6.1 Event topology for the three basic event types: $\nu_\mu\, CC$ (top), $\nu_e\, CC$ (middle) and NC(bottom) from the NOνA simulation. 91

6.2 The position of the Near detector containment cuts. The selection requires the interaction vertex must be within the red box and the start and stop points of all showers must be within the green box. The origin of the coordinates is in the center of the upstream face of the detector and the beam travels from left to right in the positive z direction. Positive y is upwards, and positive x is into the page (West). 98

6.3 Distributions of the ElasticArms vertex X (left) and Z (right) for ND data and MC (decomposed into different background event type). Magenta Lines are containmnet cut position. 98

6.4 Primary cosmic rays interact with air molecules, producing secondary cosmic rays. 99

6.5 Distribution of the transverse momentum fraction for signal, beam background and cosmic background. Cosmic rays tend to show large p_t/p value, while signal peaks at low values. This plot has all other preslection cuts and a loose LID cut of > 0.7 applied (described in Section 6.4). 100

6.6 ND number of hits per plane for data (black) and MC (red) after all ν_e preselection cuts except the nHits cut. 101

6.7 ND calorimetric energy distribution for data (black) and MC (red) after ν_e preselection.

101

6.8 Simulated LID distribution (scaled to effective full detector exposure of 1.8×10^{20} POT) in Far detector after all preselection cuts for ν_e signal and backgrounds. The two green lines shows the selection that optimize $s/\sqrt{b}$ (solid) and $s/\sqrt{s+b}$ (dashed), while the red line is the cut value used in the first analysis. 103

6.9 Simulated LEM distribution (scaled to effective full detector exposure of 1.8×10^{20} POT) in Far detector after all preselection cuts for ν_e signal and backgrounds. The two green lines shows the selection that optimize $s/\sqrt{b}$ (solid) and $s/\sqrt{s+b}$ (dashed), while the red line is the cut value used in the first analysis. 104

6.10 ND calorimetric energy distribution for ND data and MC after ν_e preselection and LID cut (decomposed into different background event types). The error bar represents flux uncertainty, which largely cancels when extrapolated to the FD. 105

7.1 The NOνA Far detector cumulative POT exposure (black line) and fiducial mass (red dots) for the first analysis period from February 6th, 2014 to May 15th, 2015. The blank region corresponds to the NuMI shutdown period. 107

7.2 POT exposure for different configurations of active diblocks in data (black) and MC (red). Here MC is area normalized to data. 108

7.3 ND number of hits in slice distribution (*Left*) and calorimetric energy distribution (*Right*) for data (black) and MC (red) after all ν_e preselection cuts. 110

7.4 ND interaction vertex position X (*Left*) and Y (*Right*) distributions for data (black) and MC (red) after ν_e preselection. The slope shape is due to the off-axis feature of the NOνA detectors. 111

7.5 ND interaction vertex Z distributions (*Left*) and length of the longest prong in a slice (*Right*) for data (black) and MC (red) after ν_e preselection. 111

7.6 ND energy per hit in a slice (*Left*) and leading shower energy in a slice (*Right*) distributions for data (black) and MC (red) after ν_e preselection. 112

7.7 ND LID (*Left*) and LEM (*Right*) distributions for data (black) and MC (red) after ν_e preselection. 112

7.8 ND calorimetric energy distributions for data (black) and MC (red) after LID (*Left*) and LEM (*Right*) selection. This is the spectrum that we extrapolate to the FD. 113

7.9 FD number of hits (*Left*) and planes (*Right*) distributions for cosmic data (black) and cosmic MC (red), while ν_e MC (blue) are shown for reference. 114

7.10 FD reconstructed shower length (*Left*) and reconstructed shower radius (*Right*) distributions for cosmic data (black) and cosmic MC (red), while ν_e MC (blue) are shown for reference. 115

7.11 FD reconstructed shower energy (*Left*) and reconstructed shower angle (*Right*) distributions for cosmic data (black) and cosmic MC (red), while ν_e MC (blue) are shown for reference. 116

7.12 Feynman diagram for lepton-nucleon scattering labeled with its kinematic quantities [21]. 119

7.13 The ND MC distribution of W^2 (left) and Q^2 (right) vs. true neutrino energy after the LID selection cut shown in color. Overlaid boxes are FD MC selected events [21]. 119

7.14 The ND MC distribution of W^2 (left) and Q^2 (right) vs. true neutrino energy after the LEM selection cut shown in color. Overlaid boxes are FD MC selected events [21]. 120

7.15 Reconstructed energy spectrums in ND for data and MC (left), and in FD for prediction and MC (right) after LID selection for the major background channels: $\nu_e \to \nu_e$ (a, b), $\nu_\mu \to \nu_\mu$ (c, d), and neutral current (e, f). 124

7.16 Reconstructed energy spectrums in ND for data and MC (left), and in FD for prediction and MC (right) after LEM selection for the major background channels: $\nu_e \to \nu_e$ (a, b), $\nu_\mu \to \nu_\mu$ (c, d), and neutral current (e, f). 125

8.1 ND Data/MC comparisons distribution with beam systematic errors: Left plot shows the reconstructed energy after LID selection (left), and Right plot shows the LID distribution after preselection. 129

8.2 ND (left) and FD (right) data/MC comparisons distribution of the Michel Electron energy spectrum [22]. 132

8.3 Reconstructed energy spectra for the absolute calibration systematics study. Left plots show data (black dots) and mis-calibrated MC(red lines) in ND, while right plots show the predicted spectrum using mis-calibration ND/FD ratio (Blue) and nominal MC (Red) in FD. Top, middle and bottom plots display the different background channels respectively: $\nu_e \rightarrow \nu_e$ (a, b), $\nu_\mu \rightarrow \nu_\mu$ (c, d), and neutral current (e, f). 133

8.4 ND calorimetric energy spectrum for 8% gradient mis-calibration shift up (left) and down (right) compared to the nominal after the LID selection. 135

8.5 ND calorimetric energy spectrum for Random cell-by-cell mis-calibration MC compare to the nominal after the LID selection. 136

8.6 Comparison between nominal FD MC (black) and light-level shifted up/down (red/blue) by 20% for number of hits in slice (*Left*) and reconstructed energy of ν_μ CC events (*Right*) distribution [23]. 138

8.7 Event weights of a 2 sigma shift up/down of the axial mass in the CC and NC quasi-elastic cross section in ND MC 140

8.8 Event weights of a 2 sigma shift up/down of the axial mass in the elastic scattering cross section in ND MC 140

8.9 Event weights of a 2 sigma shift up/down of the η production in the elastic scattering cross section in ND MC 140

8.10 Event weights of a 2 sigma shift up/down of the Pauli blocking momentum cutoff at low Q^2 in ND MC 140

8.11 Event weights of a 2 sigma shift up/down of the axial mass parameter in the Rein-Sehgal resonance cross section model for CC event in ND MC 141

8.12 Event weights of a 2 sigma shift up/down of the axial mass parameter in the Rein-Sehgal resonance cross section model for NC event in ND MC 141

8.13 Event weights of a 2 sigma shift up/down of the vector mass parameter in the Rein-Sehgal resonance cross section model for CC event in ND MC 141

8.14 Event weights of a 2 sigma shift up/down of the vector mass parameter in the Rein-Sehgal resonance cross section model for CC event in ND MC 141

8.15 Event weights of a 2 sigma shift up/down of the rate of single pion production in CC and NC for non-resonant inelastic scattering off proton in ND MC 142

8.16 Event weights of a 2 sigma shift up/down of the rate of single pion production in CC and NC for non-resonant inelastic scattering off nucleon in ND MC 142

8.17 Event weights of a 2 sigma shift up/down of the rate of two pion production in CC and NC for non-resonant inelastic scattering off proton in ND MC 142

8.18 Event weights of a 2 sigma shift up/down of the rate of two pion production in CC and NC for non-resonant inelastic scattering off nucleon in ND MC 142

8.19 Event weights of a 2 sigma shift up/down of the A_{HT} parameter in the Bodek-Yang mode in ND MC 143

8.20 Event weights of a 2 sigma shift up/down of the B_{HT} parameter in the Bodek-Yang mode in ND MC 143

8.21 Event weights of a 2 sigma shift up/down of the C_{V1u} parameter in the Bodek-Yang mode in ND MC 143

8.22 Event weights of a 2 sigma shift up/down of the C_{V2u} parameter in the Bodek-Yang mode in ND MC 143

8.23 Event weights of a 2 sigma shift up/down of the x_F distribution for low multiplicity DIS events produced by the AGKY model in ND MC. 145

8.24 Event weights of a 2 sigma shift up/down of the p_T distribution for low multiplicity DIS events produced by the AGKY model in ND MC. 145

8.25 Event weights of a 2 sigma shift up/down of the resonance decay branching ratio to photons in ND MC. 145

8.26 Event weights of a 2 sigma shift up/down of the resonance decay branching ratio to etas in ND MC. 145

8.27 Event weights of a 2 sigma shift up/down of the delta decay angle distribution in ND MC. 145

8.28 Event weights of a 2 sigma shift up/down of the pion mean free path in ND MC. 147

8.29 Event weights of a 2 sigma shift up/down of the nucleon mean free path in ND MC. 147

8.30 Event weights of a 2 sigma shift up/down of the absorption probability for pions in ND MC. 148

8.31 Event weights of a 2 sigma shift up/down of the absorption probability for nucleons in ND MC. 148

8.32 Event weights of a 2 sigma shift up/down of the charge exchange probability for pions in ND MC. 148

8.33 Event weights of a 2 sigma shift up/down of the charge exchange probability for nucleons in ND MC. 148

8.34 Event weights of a 2 sigma shift up/down of the elastic scattering probability for pions in ND MC. 148

8.35 Event weights of a 2 sigma shift up/down of the elastic scattering probability for nucleons in ND MC. 148

8.36 Event weights of a 2 sigma shift up/down of the inelastic scattering probability for pions in ND MC. 149

8.37 Event weights of a 2 sigma shift up/down of the inelastic scattering probability for nucleons in ND MC. 149

8.38 Event weights of a 2 sigma shift up/down of the pion production probability for pions in ND MC. 149

8.39 Event weights of a 2 sigma shift up/down of the pion production probability for nucleons in ND MC. 149

8.40 Vertex Z distribution for ND data (black), MC without rock muon (red) and truth rock muon events (green) after reconstruction quality cuts (left) and LID selection (right). 154

9.1 FD NuMI beam POT exposure (black) and the ν_e appearance candidates accumulation (red) [24]. 161

9.2 Timing distribution of the ν_e appearance candidates inside the in-spill window (dash blue line). The two out-of-window events are cosmic background. 163

9.3 LID distribution of the ν_e appearance candidates (black arrows) in the signal (shaded) and background (line) region. 163

9.4 FD NuMI beam data event display for the LID selected ν_e appearance candidates. The color of the boxes are scaled by the energy deposition in the cell, and gray hits represent out-of-time hits. 164

9.5 FD NuMI beam data event display for the LID selected ν_e appearance candidates. The color of the boxes are scaled by the energy deposition in the cell, and gray hits represent out-of-time cosmics. 165

9.6 FD NuMI beam data event display for the LID selected ν_e appearance candidates. The color of the boxes are scaled by the energy deposition in the cell, and gray hits represent out-of-time cosmics. 166

9.7 Distributions of the LID ν_e appearance candidates (black arrows) in the FD data compared to the FD predictions for background (blue) and total signal(red). 167

9.8 Vertex distribution of the ν_e appearance candidates in XY (a), XZ (b) and YZ (c) planes. The dotted red lines defines the containment area in the detector. 168

9.9 Likelihood of the leading shower for being a specific event hypotheses with comparison between data (black), MC prediction (red) and MC background (blue). 169

9.10 Likelihood of the leading shower for being a specific event hypotheses with comparison between data (black), MC prediction (red) and MC background (blue). 170

9.11 Energy deposition rate dE/dx in longitudinal (left) and transverse (right) direction vs. cell number from shower core for the ν_e appearance candidate in run 15330. Black dots represent data and the colored box represent MC. 170

9.12 Critical value of χ^2 for 68% (a) and 90% (b) confidential level in $\sin^2 2\theta_{13}$ vs. δ space that calculated by Feldman-Cousins procedure under normal mass hierarchy assumption. 173

9.13 LID candidates allowed values of δ_{cp} vs. $\sin^2 2\theta_{13}$ (black) and its confidence intervals at 68% (blue) and 90% (red). Grey area is the $\sin^2 2\theta_{13}$ result from Daya Bay at 68% confidence level. Top plot is for the normal mass hierarchy while the bottom one is for inverted mass hierarchy. 175

9.14 LEM candidates allowed values of δ_{cp} vs. $\sin^2 2\theta_{13}$ (black) and its confidence intervals at 68% (blue) and 90% (red). Grey area is the $\sin^2 2\theta_{13}$ result from Daya Bay at 68% confidence level. Top plot is for the normal mass hierarchy while the bottom one is for inverted mass hierarchy. 176

9.15 Significance of the difference between the selected and the predicted event counts as a function of δ_{cp} for normal hierarchy (blue) and inverted hierarchy (red) in LID (solid) and LEM (dash). 177

CHAPTER 1

The Physics of Neutrinos

1.1 A Brief Experimental History of Neutrinos

1.1.1 Discovery of Neutrinos

Neutrinos are now known as elementary particles in the Standard Model, however they were first postulated as a “desperate remedy” by W. Pauli in his famous letter [25] to the Physical Society of T*ü*bingen in 1930. The existence of the neutrino, named *neutron* at that time, perfectly explained the continuous energy spectrum in nuclear β-decays, which would have violated the energy conservation principle as there only a single electron was observed as the decay product. In Pauli’s letter, this new particle is required to be electrically neutral and have spin 1/2 to ensure conservation of the electric charge and angular momentum. Additionally it could only interact weakly and must have a small mass. In 1932, Chadwick discovered what we now call the neutron [26], but it was too heavy to be the particle predicted by Pauli. Later, Enrico Fermi renamed Pauli's particle the *neutrino*, meaning the "little neutral one". In 1934, Fermi developed the mechanism for β-decays and built his theory of the weak interaction [27]. In the same year, Bethe and Peierls showed that neutrino-matter cross-sections should be extremely small [28].

Two decades after it was proposed by Pauli, the neutrino was first detected in 1956 by F. Reines and C.L. Cowan at Savannah River nuclear plant in South Carolina, via the inverse β-reaction ($\bar{\nu} + p \rightarrow n + e^{+}$) in a tank of 400 liters of a mixture of water and cadmium chloride [29]. The detector observed this reaction using an ingenious delayed-coincidence measurement of the positron annihilation to produce the first gamma pulse, and some $5\,\mu$s later the neutron capture on cadmium gave a second gamma pulse. This technique substantially reduced the background events and helped provide unambiguous confirmation of the antineutrino's existence. Frederick Reines was awarded the Nobel prize in 1995 for this work.

Since then, the exploration of the neutrino picked up speed. In 1958, Maurice Goldhaber, Lee Grodzins and Andrew Sunyar at Brookhaven National Laboratory determined the neutrino has left-handed helicity [30]. One year later, Ray Davis showed that the antineutrinos measured by Reines and Cowan could be distinguished from neutrinos because the former ones didn't react with ^{37}Cl [31]. During this time, both pions and muons were discovered in cosmic ray experiments. In 1962, an experiment at Brookhaven AGS facility by Lederman, Schwartz and Steinberger first observed the muon neutrino after the decay of pions [32]. In this experiment, they produced the first muon neutrino beam from the decay of pions produced by a 15 GeV proton beam focused onto a beryllium target, which is still the main production method of the neutrino beam today. When these neutrinos interacted in the spark chamber downstream, they predominantly produced muons and not electrons. This established the existence of two distinct generations of the lepton family, electron neutrinos coupling to the electrons, and muon neutrinos coupling to the muon.

During the sixties and seventies, numerous scattering experiments came, one after another, using both electrons and neutrinos of high energy to probe the quark structure of nucleons and built the foundation of the quark theory. In 1973, the Gargamelle bubble chamber experiment at CERN [33] detected the neutral-current interaction

$$\bar{\nu}_\mu + e \rightarrow \bar{\nu}_\mu + e$$

mediated by the Z-boson. This interaction requires the existence of a neutral particle to carry the weak fundamental force, thus presented important evidence in support of the theory for the electroweak unification, and became part of the more encompassing framework of the "Standard Model." Two years later, the SPEAR e^+e^- collider at SLAC [34] observed the appearance of a new charged lepton, the tau (τ). The discovery of the τ lepton suggested that there is a corresponding tau neutrino ν_τ. However, due to the technical difficulties of identifying a τ lepton, ν_τ was not directly observed until 2001 in the DONUT experiment at Fermilab [35].

1.1.2 Neutrino Oscillation

In the 1960s, a physicist named Ray Davis built a detector that consisted of a tank of Cl_2C_4 under 3000 m of earth in the Homestake Mine in South Dakota [31]. It was the first experiment to detect the flux of neutrinos from the sun. Upon being struck by an electron neutrino, the chlorine nuclei became an unstable isotope of argon: $\nu_e + {}^{37}Cl \rightarrow e^- + {}^{37}Ar$. The argon atoms were later extracted and counted to measure the neutrino flux. The prediction from John N. Bahcall's Standard Solar Model [36] is 8.1 ± 1.2 SNU (solar neutrino unit, equal to the neutrino flux producing 10^{36} captures per target atom per second), while surprisingly, the Homestake experiment only observed 2.56 ± 0.25 SNU [37], about one third of the predicted number of neutrinos. This discrepancy came to be known as the *Solar Neutrino Problem*.

Clearly there are only three possible answers to the solar neutrino problem: the Solar Standard Model was incorrect, the Homestake experiment had a problem, or something happened to the neutrinos before their detection. Many subsequent experiments including helioseismology experiments soon proved the SSM model to be accurate enough to rule out the first possibility [38, 39, 40]. Later in the 1980s, several new experiments, Kamiokande [41] in Japan with a water Cherenkov detector, the GALLEX [42] and SAGE [43] experiments using liquid gallium, also detected the solar neutrinos. They soon gathered more evidence that the solar neutrino discrepancy persisted. At that point, people finally had to face the fact that the solar neutrino problem is due in some way to disappearance of electron neutrinos from the Sun before they reach Earth.

In parallel, more neutrino disappearance evidence was detected by the Kamiokande experiment [44] and the IMB experiment [45], both of which consist of large underground water Cherenkov detectors. These experiment were intended to detect proton decay, with the major background source expected to be neutrinos produced in the atmosphere by high energy cosmic rays. However, they found that, while the flux of electron neutrinos they detected was in agreement with the prediction, there is a 60% deficit in the rate of muon neutrino interactions [46]. This problem became known as the *atmospheric neutrino anomaly*, which was further confirmed by updated results from several experiments in the 1990s as shown in Figure 1.1.

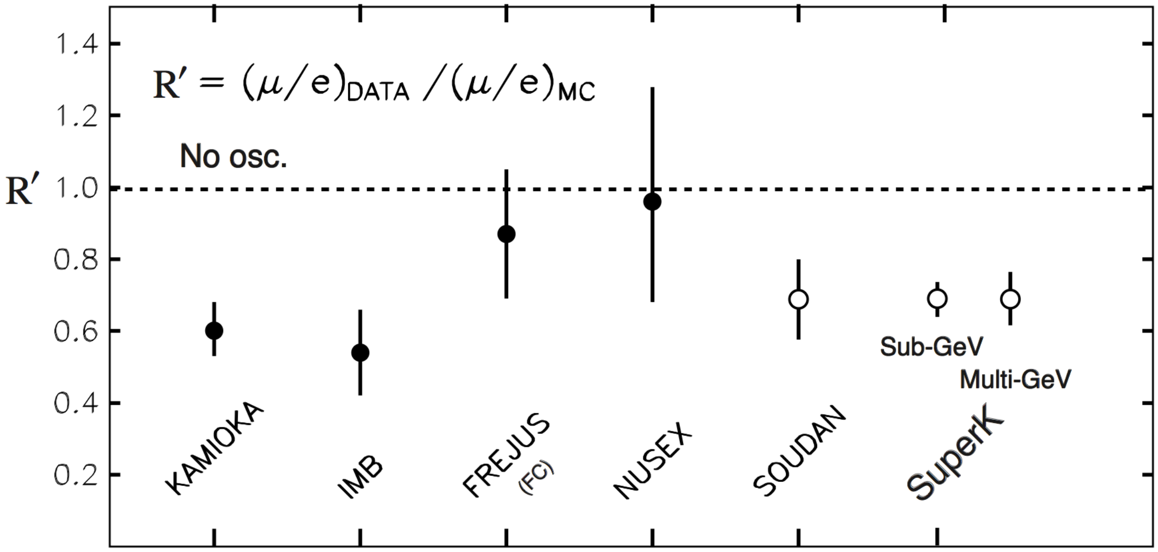

FIG. 1.1: Summary of the deficit in atmospheric muon neutrino rates compared to electron neutrinos observed in various experiments [5].

In 1985, Mikheyev and Smirnov [47] developed Wolfenstein's earlier work [48] on neutrino oscillations enhanced by the presence of matter: the MSW effect. Combining various experimental results from both the *Solar Neutrino Problem* and the *atmospheric neutrino anomaly*, the evidence for neutrino oscillations as an explanation to these two anomalies was getting stronger.

Around the turn of the millennium, in 2001 the SNO (Sudbury Neutrino Observatory) experiment in Ontario, Canada finally solved the solar neutrino problem and provided the first clear evidence that neutrinos oscillate, or change flavor, as they travel to Earth [49]. The SNO detector was located 2100 m underground and filled with 1102 tons of heavy water. The key improvement of SNO over earlier experiments was it could detect not only the solar electron neutrinos, which produced electrons when they struck the heavy water, but also some of the muon and tau neutrinos that participated the elastic scattering interactions and NC interactions. The total flux of all neutrino flavors measured agrees well with the theoretical SSM predictions. Not long after, neutrino oscillations were also confirmed to be the cause for the atmospheric neutrino anomaly by Super-K [50] experiment. This result was later supported by long baseline accelerator neutrino experiments such as K2K (KEK-to-Kamioka) [51] and MINOS (Main Injector Neutrino Oscillation Search) [52], and other subsequent experiments. Takaaki Kajita from the Super-Kamiokande Observatory and Arthur McDonald from the Sudbury Neutrino Observatory won the 2015 Nobel Prize for Physics for the discovery of neutrino oscillations. The fact that neutrinos oscillate, opens up a whole new era of neutrino physics.

1.2 Neutrinos in the Standard Model

1.2.1 Basic Ingredients of the Standard Model

The Standard Model of Particle Physics provides a complete description of the interactions of the fundamental fermions through three out of the four fundamental forces, with the exception of gravity, as well as their associated gauge bosons. It is constructed as a gauge theory of massless fields with the local gauge symmetry $SU(3)\otimes SU_L(2)\otimes U(1)$. Particle masses are introduced via spontaneous symmetry breaking and the Higgs mechanism [53].

The three forces encapsulated by the Standard Model are the electromagnetic force, the strong force and the weak force. Each force acts between particles because of some property of them: the electromagnetic force participates only between particles that are electrically charged and works at long range; the strong force is sensitive to the color charge of the particle and works at a very short range; and finally the weak force acts on the flavor of both hadrons and leptons over a very short range.

As shown in Figure 1.2, the Standard Model incorporates all of the 17 known fundamental fermions and bosons. The fundamental fermions, listed in Table 1.1, include three generations of quarks:

$$\begin{pmatrix} u \\ d \end{pmatrix}, \begin{pmatrix} c \\ s \end{pmatrix}, \begin{pmatrix} t \\ b \end{pmatrix}$$

and three generations of leptons:

$$\begin{pmatrix} \nu_e \\ \\ e \end{pmatrix}, \begin{pmatrix} \nu_\mu \\ \\ \mu \end{pmatrix}, \begin{pmatrix} \nu_\tau \\ \\ \tau \end{pmatrix}$$

The other important category of the particles in the picture are the gauge bosons as summarized in Table 1.2. Four of them are the mediators of the three forces we mentioned above: photons are the exchange particle of the electromagnetic force, gluons are the mediators of the strong force, and finally the massive W^{+-} and Z^0 are the carriers of the weak force. The last one in the boson family is the Higgs boson, through which the origin of mass in the Universe is explained. On July 2012, CERN officially announced the confirmation of the Higgs boson, which makes it the last, also the most expensive, fundamental particle to be detected [54].

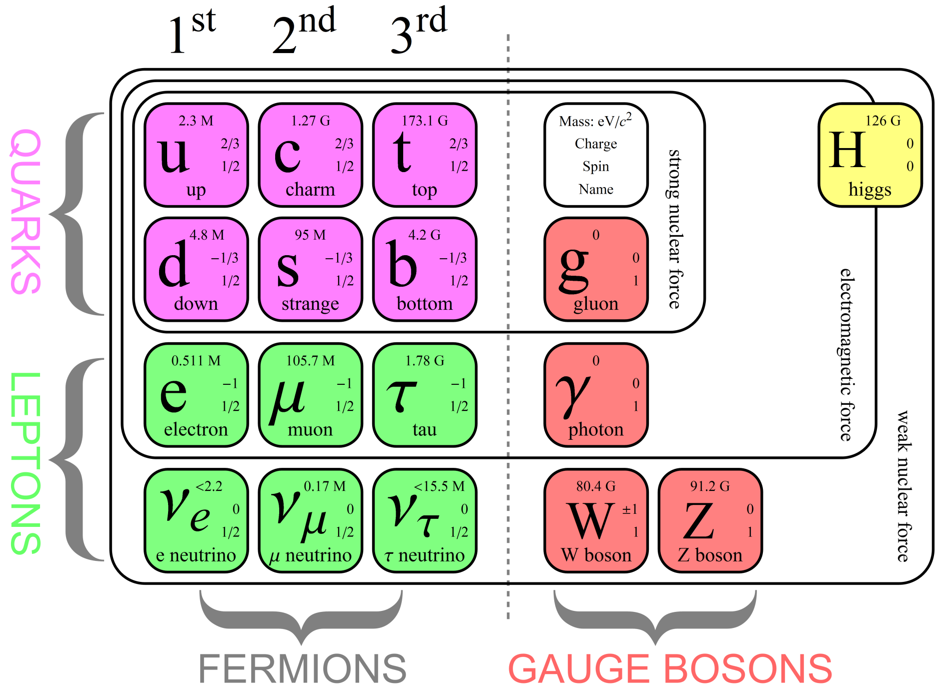
1st
2nd
3rd
QUARKS
LEPTONS
2.3 M
2/3
1/2
u
up
1.27 G
2/3
1/2
c
charm
173.1 G
2/3
1/2
t
top
4.8 M
−1/3
1/2
d
down
95 M
−1/3
1/2
s
strange
4.2 G
−1/3
1/2
b
bottom
0.511 M
−1
1/2
e
electron
105.7 M
−1
1/2
μ
muon
1.78 G
−1
1/2
τ
tau
<2.2
0
1/2
νe
e neutrino
0.17 M
0
1/2
νμ
μ neutrino
<15.5 M
0
1/2
ντ
τ neutrino
Mass: eV/c2
Charge
Spin
Name
0
0
1
g
gluon
0
0
1
γ
photon
80.4 G
±1
1
W
W boson
91.2 G
0
1
Z
Z boson
126 G
0
0
H
higgs
strong nuclear force
electromagnetic force
weak nuclear force
FERMIONS
GAUGE BOSONS

FIG. 1.2: The Standard Model of elementary particles, with the three generations of Quarks and Leptons, gauge bosons in the fourth column, and the Higgs boson in the fifth [6].

Lepton	Mass (MeV)	Charge	Quark	Mass (MeV)	Charge
e	0.511	-1	u	1.7-3.1	2/3
ν_e	?	0	d	4.1-5.7	-1/3
μ	105.7	-1	c	1,290	2/3
ν_μ	?	0	s	100	-1/3
τ	1,776.8	-1	t	172,900	2/3
ν_τ	?	0	b	4,200	-1/3

TABLE 1.1: A summary of the 12 fermions of the Standard Model for Leptons (left) and Quarks (right). The charge is measured in terms of the electron charge. The approximate mass of each fermion as obtained from [1] is shown in MeV. Note that the uncertainty in the mass of each quark is quite large. The absolute mass of the neutrinos is still unknown [2].

Boson	Charge	Spin	Mass (GeV)	Force
γ	0	1	0	Electromagnetic
$W^{\pm}$	± 1	1	80.4	Weak
Z	0	1	91.2	Weak
Gluon(8)	0	1	0	Strong
Higgs	0	0	125	-

TABLE 1.2: The 5 bosons of the Standard Model and the interactions that they mediate [2].

1.2.2 Weak Force and Interactions

We mentioned earlier that the Standard Model is a gauge theory with the gauge symmetry $SU(3)\otimes SU_L(2)\otimes U(1)$, unifying the strong force, which is described by Quantum Chromodynamics (QCD) and with local symmetry $SU(3)$, with the electromagnetic and weak forces that are confined under an $SU_L(2)\otimes U(1)$ gauge group. The weak force, acts on all known fermions, dominates the radioactive decay of subatomic particles and plays an essential role in nuclear fission. Since neutrinos are both electrically neutral and colorless, they only interact with matter through the weak force. The reminder of this thesis will concentrate the discussion on the weak interaction portion of the Standard Model.

The Standard Model describes two types of weak interactions associated with neutrinos. For each of the lepton species the neutrino couples to $W^{\pm}$ bosons in the Charged Current interactions *(CC)*:

$$L_{CC} = -\frac{g}{\sqrt{2}}\sum_{i}\left(\bar{e}_{jL}\gamma^{\mu}W_{\mu}^{-}\nu_{jL} + e_{jL}\gamma^{\mu}W_{\mu}^{+}\bar{\nu}_{jL}\right) \tag{1.1}$$

and to the Z^0 boson in the Neutral Current interactions *(NC)*:

$$L_{NC} = -\frac{g}{2\cos\theta_W}\sum_{\alpha}\bar{\nu}_{jL}\gamma^{\mu}Z_{\mu}^{0}\nu_{jL} \tag{1.2}$$

where the sum over j implies the sum over all lepton flavors: $e_j = (e, \mu, \tau)$ and $\nu_j =$

$(\nu_e, \nu_\mu, \nu_\tau)$. In the V-A Theory (Universal Theory of Weak Interaction) these Lagrangians mean the weak interactions act only on Left-handed particles (and right-handed antiparticles). Furthermore it explains the maximal violation of parity (P) and charge conjugation (C), but allowed a compound symmetry CP to be conserved. However, in 1964 James Cronin and Val Fitch discovered the evidence of CP violation in quark sector with a neutral kaon decay experiment [55], we will further discuss that this violation might exist in the lepton sector as well later in this section.

Charged current (CC) interactions, which is the major process studied in the Cowan–Reines neutrino experiment [29], occur when the neutrino is converted into its partner lepton via mediation by the $W^{\pm}$ boson with a quark or lepton. For the process shown in Figure 1.3 *left*, the W^{+} brings a positive electric charge from the electric neutral neutrino with flavor l, leaves the outgoing lepton, with flavor l as well, of negative charge -1 in order to conserve charge, and vice versa for the W^{-} process. Also, because of the conservation of the lepton number, the flavor of the incoming neutrino can be identified by the detection of the outgoing lepton.

The charged current interactions can be further divided into subcategories such as: Quasi–elastic scattering (QE), Resonant pion production (RES), Deep inelastic stattering (DIS), etc. Figure 1.4 shows the measured cross-section for each process along with the total ν_μ and $\bar{\nu}_\mu$ cross section. The QE interaction, which is the dominant process in low energy CC interactions, takes in a neutrino to transform a neutron in the nucleus into a proton and a lepton as shown in Figure 1.5 *top left*. At higher energy, the RES interaction

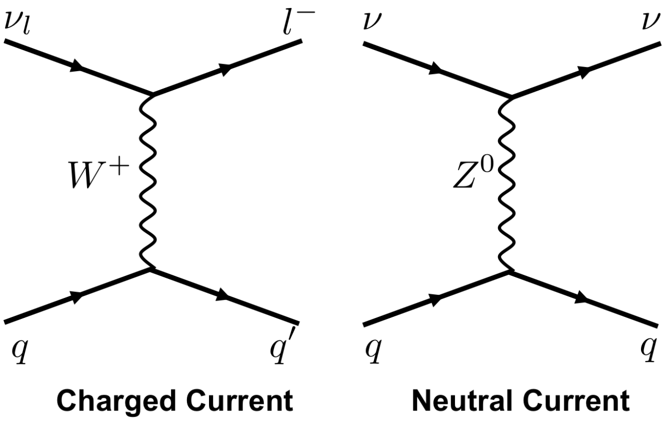

FIG. 1.3: Feynman diagrams for the possible weak interactions of neutrino: *Left:* A charged current interaction where a neutrino of flavor l interacts with a nucleon, exchanging a charged W boson and producing a lepton of type l. *Right:* A neutral current interaction where a neutrino of flavor l scatters off a nucleon, exchanging a neutral Z^0 boson.

gradually increases in strength, the neutron in the target nucleon will be converted into a Δ resonance that will later decay into a nucleon and a pion (Figure 1.5 *middle*). Above $\sim 10\,\mathrm{GeV}$ neutrino energy, the main process shifts to the DIS interaction, during which the W boson will probe the quark in the nucleus directly and break it up to release a large number of secondary particles and form a hadronic shower (Figure 1.5 *right*).

On the other hand, neutral current (NC) interactions, first identified two decades after the charged current interactions by the Gargamelle bubble chamber experiment at CERN [33], are more subtle and happen where the neutrino exchanges a Z^0 boson with a quark and scatters. As shown in Figure 1.3 *right*, the Z^0 boson has zero electric charge, therefore it doesn't transfer the charge of the particle, which also means the the flavor of the incoming neutrino cannot be directly determined.

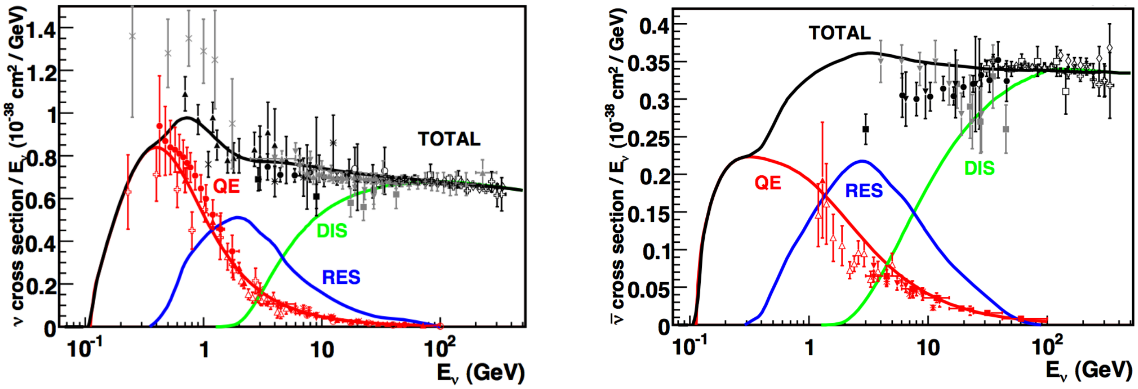

FIG. 1.4: Existing muon neutrino (left) and antineutrino (right) charged-current cross section measurements [7] and predictions [8] as a function of neutrino energy. The contributing processes in this energy region include quasi-elastic (QE) scattering, resonance production (RES), and deep inelastic scattering (DIS). The error bars in the intermediate energy range reflect the uncertainties in these cross sections (typically 10 $\sim$ 40%, depending on the channel). Image taken from [9].

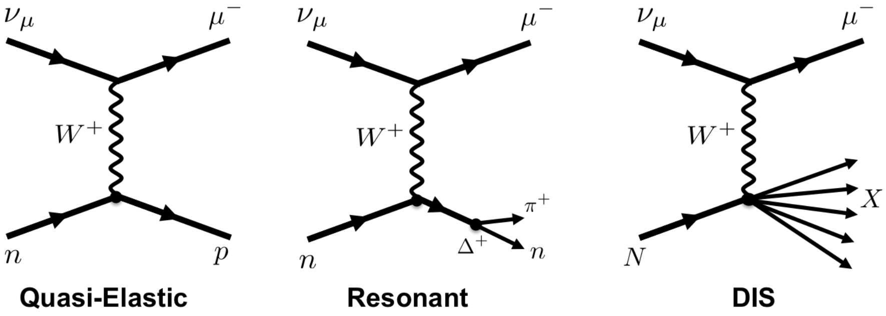

FIG. 1.5: Feynman diagrams for the three possible types of charged current interactions: *Left:* quasi–elastic scattering (QE); *Middle:* resonant pion production (RES); *Right:* deep inelastic stattering (DIS).

1.2.3 Neutrino Mass in the Standard Model

In the current form of the Standard Model, the neutrino is assumed to be massless.

The mass of a particle in Standard Model is typically written as the Dirac mass term:

$$\mathcal{L}_{Dirac} = m\bar{\psi}\psi = m\bar{\psi}_L\psi_R + m\bar{\psi}_R\psi_L \tag{1.3}$$

In this term, the mass arises from the Higgs mechanism and Yukawa coupling, which applies to all quarks and charged leptons. However, in order to fit the neutrino mass in the Dirac mass terms, we need the right-handed neutrinos, which are absent in all three generation of neutrinos. Thus the neutrino mass cannot be easily described by the Dirac mass term.

An alternative way is to write down the neutrino mass is through a Majorana mass term, which is built from the left-handed field only:

$$\mathcal{L}_{Majorana} = \frac{1}{2}\left(m\bar{\psi}_L\psi_R^C + m\bar{\psi}_R^C\psi_L\right) = \frac{1}{2}\left(m\bar{\psi}_L C\bar{\psi}_L^T + m\psi_L^T C^\dagger\psi_L\right) \tag{1.4}$$

where ψ represents the neutrino, C is the charge conjugation matrix, † denotes the hermitian conjugate. The field, $\psi = \psi + \psi_R^C$, is a charged-conjugate, two component state satisfying: $\psi = \psi^C = C\bar{\psi}^T$ [56]. The Majorana mass term can assume the particle is identical to its own antiparticle hence requires only one helicity state of the neutrino. However, by assuming the neutrino is the same as antineutrino, the Majorana mass term in Equation 1.4 violates the lepton number conservation and changes it by two units, which is totally illegal in the Standard Model. In conclusion, in the current Standard Model, there is no other way but to consider neutrinos as massless particles.

1.3 Neutrino Oscillations

As described in Section 1.1, in the past two decades there are many compelling pieces of evidence showing that neutrinos with one flavor can later be detected with another flavor, which is a quantum mechanical phenomenon known as *Neutrino Oscillations*. This would imply that neutrinos possess a small but non-zero mass and causes the lepton flavor number conservation to be violated, which is not consistent with the Standard Model. This section will review the fundamental formalism of the Neutrino Oscillations both in vacuum and matter and other side topics.

The most essential feature of neutrino oscillation theory is that a neutrino can be described in two sets of eigenstates: the flavor eigenstates, labeled $|\nu_\alpha\rangle$ ($\alpha = e, \mu, \tau$) that correspond to the flavor of the produced lepton and govern the neutrino's interaction with matter; and mass eigenstates $|\nu_i\rangle$ ($i = 1, 2, 3$) that describe how the neutrino propagates through space. If we introduce non-zero masses to neutrinos, the flavor eigenstates can be written as a superposition of the mass eigenstates as following:

$$|\nu_\alpha\rangle = \sum_{i=1}^{N} U^*_{\alpha i}|\nu_i\rangle \tag{1.5}$$

where N is the number of neutrino mass/flavor states, and U is the $N \times N$ PMNS unitary matrix, named after Pontecorvo [57], Maki, Nakagawa and Sakata [58].

In the rest frame, the time evolution of a neutrino mass eigenstate $|\nu_i\rangle$ with mass m_i

can be written as [2]:

$$|\nu_i(t)\rangle = e^{-i(E_i t - p_i L)}|\nu_i(0)\rangle \tag{1.6}$$

where L is the distance travelled during the time interval t. It is known that each eigenstate of a neutrino beam that contributes to the oscillation signal coherently shares a common energy E [59]. The mass of neutrino, even if non-zero, is very small ($m_i \ll E$), thus the momentum of $|\nu_i\rangle$ with mass m_i can be approximated by:

$$\begin{aligned} p_i &= \sqrt{E^2 - m_i^2} \approx \sqrt{\left(E - \frac{m_i^2}{2E}\right)^2} \\ &= E - \frac{m_i^2}{2E} \end{aligned} \tag{1.7}$$

Furthermore, for highly relativistic neutrinos, we can assume $t \approx L$. Thus the phase in Equation 1.6 simplifies to:

$$\begin{aligned} |\nu_i(L)\rangle &= e^{-i(Et-(E-\frac{m_i^2}{2E})L)}|\nu_i(0)\rangle \\ &= e^{-i\frac{m_i^2 L}{2E}}|\nu_i(0)\rangle \end{aligned} \tag{1.8}$$

Combining Equation 1.5 and Equation 1.8, we have the expression of flavor eigenstate $|\nu_\alpha\rangle$ with time evolution as:

$$|\nu_\alpha(L)\rangle = \sum_{i=1}^{N} U_{\alpha i}^* e^{-im_i^2(\frac{L}{2E})}|\nu_i(0)\rangle \tag{1.9}$$

The transition probability for measuring a neutrino in flavor state ν_β after traveling through distance L while this neutrino was created as ν_α flavor eigenstate is given by:

$$\begin{aligned}
P(\nu_\alpha \to \nu_\beta) &= |\langle \nu_\beta | \nu_\alpha(L)\rangle|^2 = \left| \left(\sum_j \langle \nu_j | U_{\beta j} \right) \left(\sum_i U^*_{\alpha i} e^{-im_i^2(\frac{L}{2E})} |\nu_i\rangle \right) \right|^2 \\
&= \left| \sum_j U_{\beta j} \sum_i U^*_{\alpha i} e^{-im_i^2(\frac{L}{2E})} \delta_{ij} \right|^2 = \left| \sum_i U_{\beta i} U^*_{\alpha i} e^{-im_i^2(\frac{L}{2E})} \right|^2 \\
&= \sum_i \sum_j U_{\beta i} U^*_{\alpha i} U_{\beta j} U^*_{\alpha j} e^{-i(m_i^2 - m_j^2)(\frac{L}{2E})} \\
&= \sum_i \sum_j U_{\beta i} U^*_{\alpha i} U_{\beta j} U^*_{\alpha j} e^{-i\Delta m_{ij}^2(\frac{L}{2E})} \qquad (1.10)
\end{aligned}$$

where $\Delta m^2_{ij} = m_i^2 - m_j^2$ is the mass squared splitting between the ith and jth eigenstates. The dependence on Δm^2_{ij} is direct evident that if neutrinos are massless, the oscillation does not happen at all. We can further expand Equation 1.10 by separating its real and imaginary parts, and using the properties of the unitary matrix U ($\sum\limits_i U_{\beta i} U^*_{\alpha j} = \delta_{\alpha\beta}$):

$$\begin{aligned}
P(\nu_\alpha \to \nu_\beta) &= \delta_{\alpha\beta} + 2 \sum_{i>j} \Re \left[U_{\beta i} U^*_{\alpha i} U_{\beta j} U^*_{\alpha j} (e^{-i\Delta m_{ij}^2(\frac{L}{2E})} - 1) \right] \\
&= \delta_{\alpha\beta} \\
&\quad -4 \sum_{i>j} \Re \left[U_{\beta i} U^*_{\alpha i} U_{\beta j} U^*_{\alpha j} \right] \sin^2 \left(\frac{\Delta m^2_{ij}}{4E} L \right) \\
&\quad +2 \sum_{i>j} \Im \left[U_{\beta i} U^*_{\alpha i} U_{\beta j} U^*_{\alpha j} \right] \sin \left(\frac{\Delta m^2_{ij}}{2E} L \right) \qquad (1.11)
\end{aligned}$$

Similarly, we can define the transition probability for the antineutrino oscillation.

Assuming CPT invariance holds, it can be shown that:

$$P(\bar{\nu}_\alpha \to \bar{\nu}_\beta) = P(\nu_\beta \to \nu_\alpha) \tag{1.12}$$

By reversing ν_α and ν_β in Equation 1.11 and combining Equation 1.12, we have:

$$\begin{aligned} P(\nu_\beta \to \nu_\alpha) &= P(\nu_\alpha \to \nu_\beta; U \to U^*) \\ &= P(\bar{\nu}_\alpha \to \bar{\nu}_\beta) \end{aligned} \tag{1.13}$$

This indicates that by substituting the mixing matrix U with its complex conjugate U^*, we can obtain the antineutrino oscillation probabilities from the neutrino oscillation probabilities. However, the mixing matrix U is complex, thus $U \neq U^*$, which gives an opposite sign in the last term of Equation 1.11 in antineutrino case. This implies the appearance oscillation probabilities are different for neutrinos and antineutrinos and presents a *CP* violation in the neutrino sector. Neutrino CP violation has important implications for cosmological models. If it is non-zero, it could be the explanation to the observed matter-antimatter imbalance in the Universe. All the other known source of CP violation in other sectors are too small to account for the matter density in the universe.

1.3.1 Three-Flavor Neutrino Oscillations

The previous expressions are derived under the assumption that neutrinos have N generations, where N can be any integer. As we discussed in Section 1.2.1, the Standard

Model describes, supported by the best experimental knowledge to date, that there are three generations of neutrinos. Thus in the general case, we have:

$$\begin{pmatrix} \nu_e \\ \nu_\mu \\ \nu_\tau \end{pmatrix} = U_{PMNS} \begin{pmatrix} \nu_1 \\ \nu_2 \\ \nu_3 \end{pmatrix} \tag{1.14}$$

and

$$\begin{aligned} U_{PMNS} &= \begin{pmatrix} U_{e1} & U_{e2} & U_{e3} \\ U_{\mu 1} & U_{\mu 2} & U_{\mu 3} \\ U_{\tau 1} & U_{\tau 2} & U_{\tau 3} \end{pmatrix} \\ &= \begin{pmatrix} c_{12}c_{13} & s_{12}s_{13} & s_{13}e^{-i\delta} \\ -s_{12}c_{23} - c_{12}s_{23}s_{13}e^{i\delta} & c_{12}c_{23} - s_{12}s_{23}s_{13}e^{i\delta} & s_{23}c_{13} \\ s_{12}s_{23} - c_{12}c_{23}s_{13}e^{i\delta} & -c_{12}s_{23} - s_{12}c_{23}s_{13}e^{i\delta} & c_{23}c_{13} \end{pmatrix} \end{aligned} \tag{1.15}$$

Here the PMNS mixing matrix is parameterized in terms of three mixing angles θ_{ij} ($c_{ij} \equiv \cos\theta_{ij}$ and $s_{ij} \equiv \sin\theta_{ij}$), and a phase δ, allowing for CP violation in the neutrino sector as we discussed earlier. Note that there are two Majorana phases α_1 and α_2, ignored here since they are unobservable in neutrino oscillations.

A more convenient way of presenting the PMNS matrix is to express it as a product of three matrices with each of them only depending on one mixing angle:

$$U_{PMNS} = \begin{pmatrix} 1 & 0 & 0 \\ 0 & c_{23} & s_{23} \\ 0 & -s_{23} & c_{23} \end{pmatrix} \times \begin{pmatrix} c_{13} & 0 & s_{13}e^{-i\delta} \\ 0 & 1 & 0 \\ -s_{13}e^{i\delta} & 0 & c_{13} \end{pmatrix} \times \begin{pmatrix} c_{12} & s_{12} & 0 \\ -s_{12} & c_{12} & 0 \\ 0 & 0 & 1 \end{pmatrix} \tag{1.16}$$

This form is instructive to visualize the territory of various neutrino experiments. Historically the sector (23) is referred to *atmospheric neutrino oscillations* with mixing angle θ_{23} and mass-spliting Δm^2_{32} or Δm^2_{atm}. The sector (12) is associated with *solar neutrino oscillations* with θ_{12} and mass-spliting Δm^2_{12} or Δm^2_{sol}. In sector (13), mass-spliting Δm^2_{13} is the approximately the same to Δm^2_{atm}, and mixing angle θ_{13} is the last one to be precisely measured by the long-baseline and reactor neutrino experiments [2]. Also, the non-zero value of θ_{13} is necessary to observe the CP-violating phase δ and mass hierarchy.

With the 3 flavor form of PMNS mixing matrix, Equation 1.11 gives the explicit expression of the neutrino oscillation probability in vacuum. Considering that ν_e appearance is the main topic of this thesis, the probability of $\nu_\mu \to \nu_e$ is shown here as an example:

$$\begin{aligned} P(\nu_\mu \to \nu_e) \quad = \quad & s^2_{23}\sin^2 2\theta_{13}\sin^2\frac{\Delta m^2_{31}L}{4E} + c^2_{13}c^2_{23}\sin^2 2\theta_{12}\sin^2\frac{\Delta m^2_{21}L}{4E} \\ & +8c^2_{13}s_{13}c_{12}s_{12}s_{23}c_{23}\sin\frac{\Delta m^2_{21}L}{4E}\sin\frac{\Delta m^2_{31}L}{4E}\cos\left(\frac{\Delta m^2_{32}L}{4E}+\delta\right) \\ & -2s^2_{12}s^2_{23}\sin^2 2\theta_{13}\sin\frac{\Delta m^2_{21}L}{4E}\sin\frac{\Delta m^2_{31}L}{4E}\cos\frac{\Delta m^2_{32}L}{4E} \\ & +4c^2_{13}s^2_{12}s_{13}s_{23}(s_{23}s_{13}s_{12} - 2c_{12}c_{23}\cos\delta)\sin^2\frac{\Delta m^2_{21}L}{4E} \end{aligned} \tag{1.17}$$

As shown in Equation 1.17, the oscillation probability is only sensitive to mass splitting terms but not the absolute mass of the neutrinos. So far the experimental results only provide the measurement of the two mass splitting Δm^2_{23} and Δm^2_{12}, but the absolute masses and even the relative orientation of Δm^2_{23} remains unknown. This leads to two possible scenarios of the mass ordering, or *neutrino mass hierarchy*, the *normal hierarchy* as shown in the left of Figure 1.6, and the *inverted hierarchy* in the right of Figure 1.6.

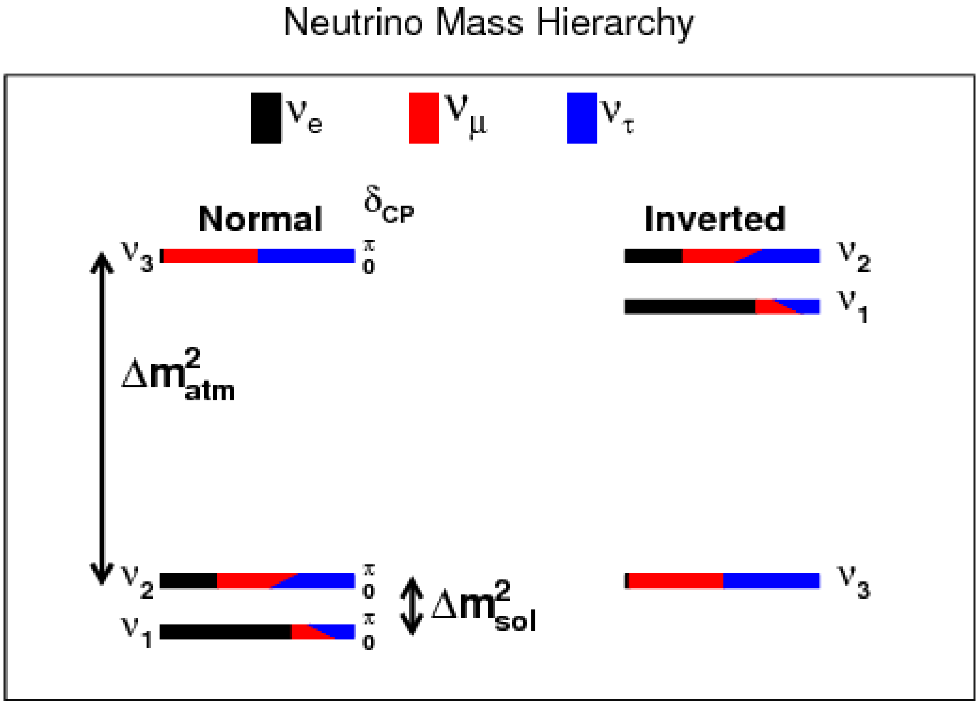
Neutrino Mass Hierarchy
ν_e
ν_μ
ν_τ
Normal
δ_{CP}
Inverted
ν_3
π
0
ν_2
ν_1
Δm^2_{atm}
ν_2
π
0
ν_1
π
0
Δm^2_{sol}
ν_3

FIG. 1.6: Schematic of the permitted mass orderings in the neutrino sector. The diagram on the left denotes the *normal hierarchy*, while the one on the right denotes the *inverted hierarchy*. The colors represent the approximate flavor compositions as a function of the CP phase δ_{cp} of each mass eigenstate [10].

1.3.2 Two-Flavor Neutrino Oscillations

The complete expression of the three-flavor oscillation probability as shown in Equation 1.17 is rather cumbersome, and gets even more complex when matter effects (to be discussed in Section 1.3.3) are considered. As will be shown in Section 1.4, current experimental data indicates that one of the two mass splitting, Δm^2_{23}, is much larger than the other one, Δm^2_{12}. The baseline length L that the neutrino travels and the neutrino energy E are experimental variables and can be chosen to make $\Delta m^2_{ij}L/E \sim O(1)$. Thus with a fixed value of L/E, one experiment is only sensitive to one of the two $\Delta m^2_{ij}L/E$ terms. It has also been found experimentally that θ_{23} and θ_{12} are relatively large but θ_{13} is small, this allows us to further reduce the terms by assuming $\sin\theta_{13} \approx 0$.

With the above two-flavor approximations, the probability of ν_e appearance through $\nu_\mu \to \nu_e$ oscillation from Equation 1.17 can be reduced to:

$$P(\nu_\mu \to \nu_e) = \sin^2\theta_{23}\sin^2 2\theta_{13}\sin^2\frac{1.27\Delta m^2_{32}L}{E} \tag{1.18}$$

where the units conversion $\frac{\Delta m^2 L}{4E} = 1.27\frac{\Delta m^2(eV^2)L(km)}{E(GeV)}$ is applied here. Figure 1.7 shows the ν_e appearance probability as a function of energy for the NOνA experiment with baseline L =810 km.

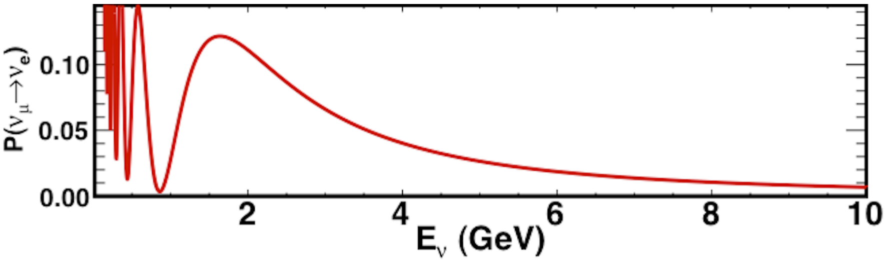

FIG. 1.7: The $\nu_\mu \to \nu_e$ appearance probability under the two-flavor oscillation assumption as in Equation 1.18 with the NOνA baseline $L = 810km$

1.3.3 Neutrino Oscillations in Matter

In Section 1.3.1 and 1.3.2, when we described the neutrino flavor oscillations, the neutrinos were assumed to propagate in a vacuum. In the case of two-flavor vacuum oscillations, the Schroedinger equation for the time evolution of flavor eigenstates is:

$$i\frac{d}{dt}\begin{pmatrix} \nu_e \\ \nu_\mu \end{pmatrix} = H_V \begin{pmatrix} \nu_e \\ \nu_\mu \end{pmatrix} \tag{1.19}$$

where

$$H_v = \left(\frac{\Delta m^2}{4E}\right)\begin{pmatrix} -\cos 2\theta & \sin 2\theta \\ \sin 2\theta & \cos 2\theta \end{pmatrix} \tag{1.20}$$

When traversing matter, neutrinos of all flavors can coherently forward-scatter from electrons (e^-), protons (p), and neutrons (n) by exchanging a $W^\pm$ or Z^0 between the time of their creation and the time of their detection. But only the electron neutrino will scatter elastically via charged current interaction from electrons, while the effect of coherent NC interactions in matter are the same for all flavors of neutrinos as shown in Figure 1.8. As a result, the oscillation probability can be different for the different flavors. This flavor-changing mechanism in matter was first described by Mikheyev, Smirnov [47] and Wolfenstein [48] and known as the MSW effect.

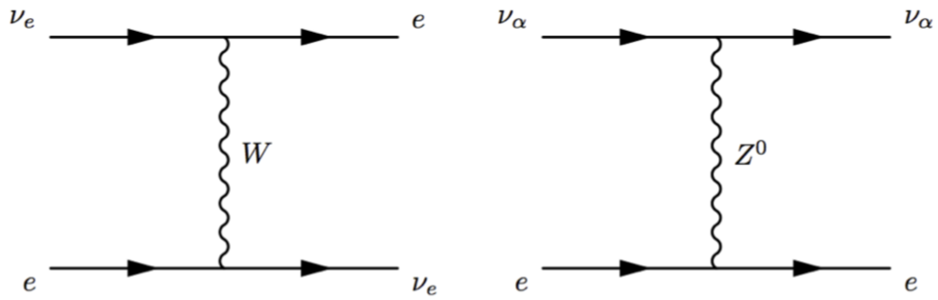

FIG. 1.8: Coherent forward scattering diagrams for neutrinos going through matter. The charged current (CC) process (left) can only occur for ν_e whereas neutral current (NC) scattering affects all flavors ν_α equally. This introduces an additional potential to the ν_e propagation Hamiltonian.

These interactions give rise to an extra term in the potential:

$$V_e = \pm\sqrt{2} G_F N_e, \tag{1.21}$$

which depends on the number density of electrons in the matter N_e and the Fermi Constant G_F. The positive (negative) sign applies to electron-neutrinos (antineutrinos). The new Hamiltonian that counts the interactions of neutrinos in matter, H_M, can be written as

$$H_M = \left(\frac{\Delta m^2}{4E}\right) \begin{pmatrix} -\cos 2\theta + A & \sin 2\theta \\ \sin 2\theta & \cos 2\theta - A \end{pmatrix} \tag{1.22}$$

with

$$A = \pm \frac{2\sqrt{2} G_F N_e E}{\Delta m^2}.$$

By diagonalizing equation (1.22), H_M can be rewritten in a form similar to the Hamiltonian in vacuum (Equation (1.20)),

$$H_M = \left(\frac{\Delta m_m^2}{4E}\right) \begin{pmatrix} -\cos 2\theta_m & \sin 2\theta_m \\ \sin 2\theta_m & \cos 2\theta_m \end{pmatrix}, \tag{1.23}$$

where θ_m is an effective mixing angle in matter and $\Delta m_m{}^2$ is a effective difference of squared masses. By comparing Equations (1.22) and (1.23), we then have:

$$\sin^2 2\theta_m = \frac{\sin^2 2\theta}{f_{MSW}}, \tag{1.24}$$

$$\Delta m_m^2 = \Delta m^2 f_{MSW}, \tag{1.25}$$

where

$$f_{MSW} = \sqrt{\left(\pm \frac{2\sqrt{2} G_F N_e E}{\Delta m_{12}^2}\right) + \sin^2(2\theta_{12})} \tag{1.26}$$

with the positive sign applying to ν_e case and negative sign applying to $\overline{\nu}_e$ case. Hence the size of the MSW effect is different for neutrinos and antineutrinos, and sensitive to the sign of Δm^2_{23}. Long baseline oscillation experiments like NOνA, take advantage of this matter effect to try to solve the puzzle of the mass hierarchy and possibly the CP-violating phase δ_{cp}.

1.4 Neutrino Oscillations Experiments

In the recent years, neutrino experiments are focused on solving the three remaining missing puzzles: more precise measurement of θ_{13}, CP-violating phase δ_{cp}, and the neutrino mass hierarchy. The two artificial neutrino sources, *reactor neutrinos* and *accelerator neutrinos*, provide two directions to search for the answers.

1.4.1 Reactor Antineutrino Experiments

Reactor antineutrino experiments can be traced back to the Cowan-Reines experiment in 1956. The **KamLAND** experiment in Japan, who first observed the antineutrino disappearance at high significance in 2002 [60, 61], and later presented the best measurement of the sector (12) oscillation parameter to date [62]. Another remarkable contribution of this kind of experiments was presented in 2012, when the **Daya Bay** experiment in China, the **RENO** experiment in Korea and the **Double-Chooz** experiment in France provided precision measurements of the last unknown mixing angle θ_{13}.

These reactor experiments normally have short baselines $L \sim 1\ km$ and low energies of $E \sim 3\ MeV$. Using the derivation in Section 1.3.2 we can neglect the Δm^2_{12} terms, and write down the two-flavor approximation for the $\bar{\nu}_e$ survival probability which mainly depends on the Δm^2_{23}:

$$P(\bar{\nu}_e \to \bar{\nu}_e) = 1 - \sin^2 2\theta_{13} \sin^2 \frac{1.27\Delta m^2_{32} L}{E}$$

The reactor electron antineutrinos are normally produced by β-decay in the nuclear fission process:

$$n^0 \to p^+ + e^- + \bar{\nu}_e$$

Then later, the rector $\bar{\nu}_e$ can be detected via the inverse beta decay reaction:

$$\bar{\nu}_e + p^+ \to e^+ + n$$

To obtain higher precision, besides the delayed-coincidence technique with the positron and neutron signal, Daya Bay and RENO also employee multiple detectors. With the Near detectors to measure the total source flux and Far detectors that are about $1 \sim 2\ km$ away to determine the oscillated flux, these experiments can then make a relative measurement of the $\bar{\nu}_e$ disappearance.

The reactor process provides a low energy yet, abundant, neutrino source, which enables the experiments to build up the exposure in shorter period of time than the accelerator experiments. In May 2015, Daya Bay released its latest measurements based on 404 days data and $6.9 \times 10^5\ GW_{th} - ton - days$ total exposure, finding $\sin^2 2\theta_{13} =$

0.084±0.005 [63], which is the most precise measurement to date, and further demonstrates the power of the reactor experiments.

1.4.2 Accelerator Neutrino Experiments

Accelerator neutrino beams, produced with the same technique used to detect the first muon neutrinos in 1962, were constructed at several locations such as Brookhaven, CERN, Fermilab, and Los Alamos and were used by many different accelerator neutrino experiments. More details about the technique of the accelerator neutrino beams will be described in Section 2.2.

The very first long baseline neutrino oscillation experiment configured with a man-made neutrino beam was the **Kamioka-to-Kamiokande** (**K2K**) experiment in Japan. The K2K experiment, which ran from 1999 to 2004, produced a muon neutrino beam from a 12 GeV proton synchrotron from the KEK facility, and detected it with the Super-kamiokande detector located 250 km away. It used the two-detectors technique, a Near detector to measure the flux and a Far detector to measure the oscillation, to detect the $\nu_\mu \rightarrow \nu_\mu$ oscillation. It concluded that at 4.3σ there had been a disappearance of muon neutrinos and reports the best fit of mass splitting $\Delta m^2_{23} = 2.8 \times 10^{-3} eV^2$ [64].

The **MINOS** (**Main Injector Neutrino Oscillation Search**) experiment, started to collect data in 2005 and used the NuMI neutrino beamline at Fermilab, the same as **NOνA**. It is designed to search for the $\nu_\mu \rightarrow \nu_\mu$ oscillation, and consists of a 980 ton Near detector and a 5.4 kt Far detector 735 km away, both of which are steel-scintillator, sampling calorimeters made out of alternating planes of magnetized steel and plastic scintillators. MINOS has collected 10.71×10^{20} *POT (Proton On Target)* of neutrino beam and 3.36×10^{20} *POT* antineutrino beam data and reported these measurement as: $\Delta m^2_{23} = [2.28 - 2.46] \times 10^{-3}\ eV^2$ (68% $C.L.$) and $\sin^2\theta_{23} = 0.35 - 0.65$ (90% $C.L.$) in the normal hierarchy; and $\Delta m^2_{23} = [2.32 - 2.53] \times 10^{-3}\ eV^2$ (68% $C.L.$) and $\sin^2\theta_{23} = 0.34 - 0.67$ (90% $C.L.$) in the inverted hierarchy [65].

There are several other accelerator neutrino experiments using various detector or beamline designs, such as: **NOνA**, the subject of this thesis; **T2K**, the second generation experiment follow up to the K2K; and **DUNE (Deep Underground Neutrino Experiment)**, a proposed experiment that adopts a 1300 km baseline. The high energy neutrinos ($E \sim GeV$) supplied by the beamline gives them the ability to adopt longer baselines ($L \sim km$), which allows the MSW effect to build up while the neutrino beam travels through the earth, and consequently gives these experiments better sensitivity to all neutrino oscillation parameters: the three mixing angles, the large and small mass differences, the neutrino mass hierarchy, and CP violation phase δ_{CP}.

1.5 Summary and Current Status

Since the millennium, the field of neutrino oscillation physics has made great advances through various experiments. Solar neutrino experiments and KamLAND have measured the sector (12) parameters Δm^2_{12} along with its sign, and θ_{12} to high precision. Atmospheric neutrino results from SuperK, T2K and MINOS provide the best measurement of Δm^2_{23}

Parameters	Current Experimental Value
Δm^2_{12}	$(7.53 \pm 0.18) \times 10^{-5} eV^2$
Δm^2_{23}	$(2.44 \pm 0.06) \times 10^{-3} eV^2$ (normal hierarchy) $(2.52 \pm 0.07) \times 10^{-3} eV^2$ (inverted hierarchy)
$\sin^2(\theta_{12})$	0.304 ± 0.014
$\sin^2(\theta_{23})$	0.51 ± 0.05 (normal hierarchy) 0.50 ± 0.05 (inverted hierarchy)
$\sin^2(\theta_{13})$	$(2.19 \pm 0.12) \times 10^{-2}$

TABLE 1.3: Current experimental measurements based on the 3-neutrino mixing scheme, taken from [2].

and θ_{23}. Finally, the recent results from Daya Bay [63], RENO [66] and Double Chooz [67] bring the measurement of θ_{13} to a more precise level. The best fit values of these parameters are listed in Table 1.3.

However, there still are some remaining questions in neutrino physics, for example what is the more precise value of θ_{23}? Do we have normal hierarchy or inverted hierarchy? What is the value of the CP-violating phase δ_{cp}? All these questions motivate a new generation of the neutrino experiments that will push the measurements of neutrino oscillations to the next level. Among them, NOνA is a pioneer that could possibly answer these questions.

CHAPTER 2

The NOνA Experiment

2.1 NOνA Overview and Physics goals

The NuMI Off-Axis ν_e Appearance (NOνA) experiment is a long-baseline, off-axis neutrino oscillation experiment. It is designed to search for oscillations of ν_μ to ν_e by comparing measurements of the NuMI beam composition in two detectors [13]. The primary goal of NOνA is to observe the $\nu_\mu \to \nu_e$ oscillation in order to measure the oscillation parameter $\sin^2 2\theta_{13}$, the neutrino mass ordering, and the CP violation phase δ.

The NOνA experiment is illustrated in Figure 2.1. The neutrino beam is generated at Fermi National Accelerator Laboratory in Batavia, Illinois by the Neutrinos at the Main Injector (NuMI) facility. Two NOνA detectors, located at two points along the beam line, observe the neutrinos. The Near Detector (ND), situated 1 km away from the proton target at Fermilab, measures neutrinos prior to oscillation. The Far Detector (FD), is located 810 km away at Ash River, Minnesota and measures the neutrinos after they have traveled through the Earth and potentially oscillated.

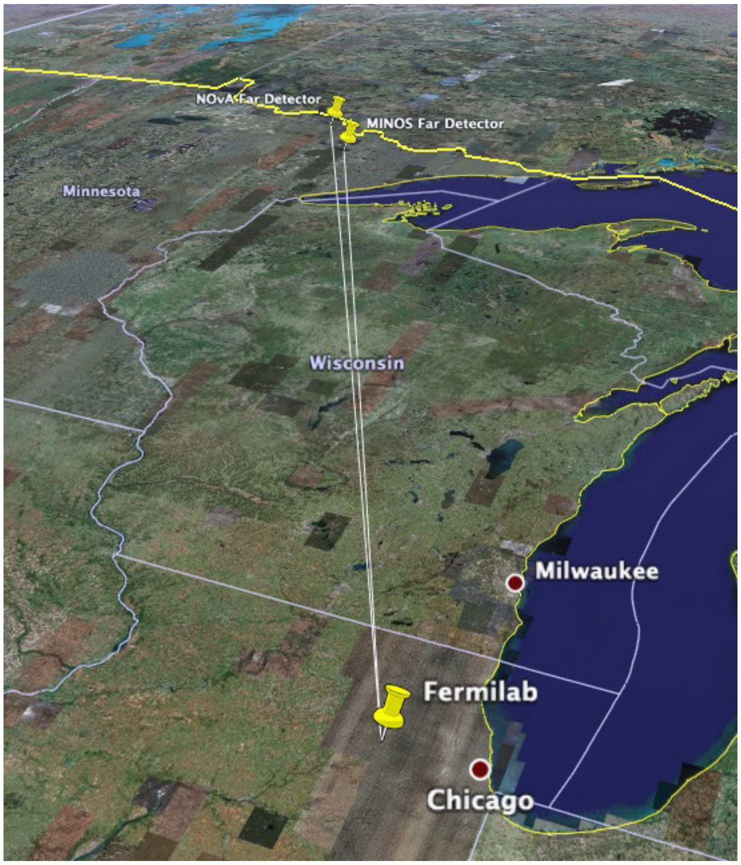
NOvA Far Detector
MINOS Far Detector
Minnesota
Wisconsin
Milwaukee
Fermilab
Chicago

FIG. 2.1: Location of the two NOνA detectors. The Near Detector is located at Fermilab, while the Far Detector sits 810 km away at Ash River, Minnesota.

These two detectors are functionally equivalent and are located on the same off-axis angle from the beam line. By extrapolating the measured Near Detector spectrum to predict the Far Detector spectrum, the impact of systematics effects such as neutrino flux mismodeling, uncertainties in cross sections and detector efficiencies are largely cancelled in the physics analysis.

2.2 The NuMI Beamline

The NOνA neutrino beam is produced by the dedicated Main Injector Neutrino (NuMI) beam facility based at Fermilab [68, 14, 69]. The construction of the NuMI facility was completed in Winter 2005, and began routine operations in May, 2005. The NuMI beam is of conventional design, resulting from the decays of pion and kaon secondaries produced in the NuMI target, but with far greater beam power than historical neutrino beams. During its years of operation for the MINOS experiment, the intensity of the NuMI beam was around 350 kW. It has delivered a high-intensity flux of muon neutrinos of variable energy (2-20 GeV) directed into the Earth at 58 mrad for both short (1 km) and long (700-900 km) baseline experiments such as NOνA, MINOS, and MINERνA.

The process of the neutrino production and the major components of the NuMI beamline are illustrated as Figure 2.2 and 2.3. It starts from a series of accelerators involving a linear accelerator (Linac) and two circular machines called the Booster and Main Injector. The protons are accelerated by the Linac and the Booster from the source to 8 GeV/c, which is the injection energy of the Main Injector. In the Main Injector, these protons are accelerated to their final energy of 120 GeV/c, extracted, and bent 58 mrad below the horizontal to account for the curvature of the Earth when directed towards the Soudan Underground Laboratory, where the MINOS Far Detector was located.

2.2.1 Basic Principle

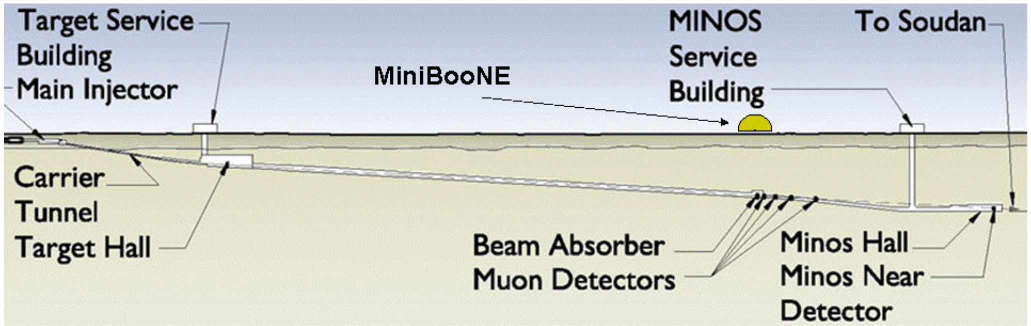
Target Service
Building
Main Injector
MiniBooNE
MINOS
Service
Building
To Soudan
Carrier
Tunnel
Target Hall
Beam Absorber
Muon Detectors
Minos Hall
Minos Near
Detector

NuMI event composition at MB
ν_μ-81%, ν_e-5%, $\bar{\nu}_\mu$-13%, $\bar{\nu}_e$-1%

FIG. 2.2: Layout of the NuMI beam facility [11].

The proton beam spills extracted from the Main Injector storage ring are $10\,\mu s$ per cycle, and each contains 2.5×10^{13} protons (at design intensity). These protons are transported along a carrier tunnel and then directed to strike a carbon target (about 6×10^{20} protons on target per year). The collisions produce a shower of hadrons via strong interactions, most of which are pions and kaons. Charged pions and kaons from these secondaries are focused by a system of two magnetic horns, the relative position of which can be adjusted to change the energy profile of the beam. These hadrons then enter a 675 m long helium filled decay pipe where they decay primarily into muons and muon neutrinos through the channels:

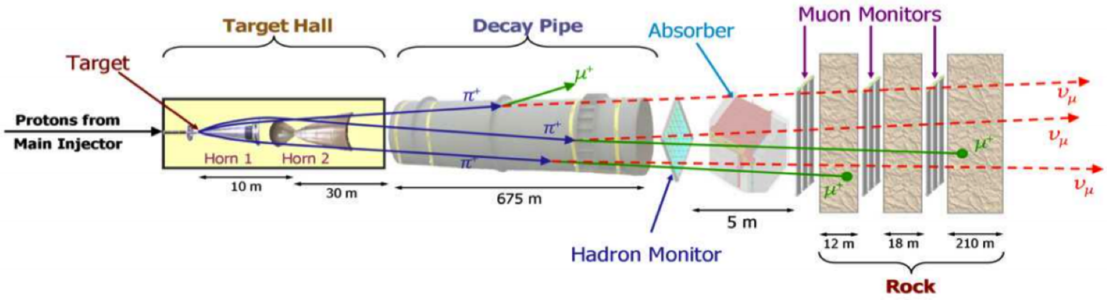
Target Hall
Decay Pipe
Absorber
Muon Monitors
Target
Protons from Main Injector
Horn 1
Horn 2
π^+
μ^+
ν_μ
10 m
30 m
675 m
5 m
Hadron Monitor
12 m
18 m
210 m
Rock

FIG. 2.3: The major components of the NuMI beamline. 120 GeV protons extracted from the Main Injector are incident from the left hand side and hit the target. Secondary mesons are focused by the horns and subsequently decay in the decay pipe producing ν_μ. The remaining hadrons are absorbed at the end of the pipe [12].

$$\pi^+ \rightarrow \mu^+ + \nu_\mu,$$

$$K^+ \rightarrow \mu^+ + \nu_\mu.$$

At the end of the decay pipe, a hadron absorber, made of a water-cooled core of steel and aluminum surrounded by blocks of steel and concrete, stops any hadrons that failed to decay to neutrinos in the pipe. After that, the beam passes through another 240m of rock that removes the vast majority of the remaining muons and leaves only neutrinos in the beam. In the following section, each of these components will be described in more detail.

2.2.2 The Target

As mentioned in last section, the neutrinos come from secondary mesons produced by the interaction of the accelerated protons with nuclei in the target. To supply a high-intensity flux of muon neutrinos to the downstream experiments, the target needs to be designed to maximize the ν_μ charged current event rate, which means it should be sufficiently long to allow most of the primary protons from the Main Injector to interact, but thin and narrow to minimize the re-absorption by the target, so that the secondary pions and kaons can easily escape through the sides.

The target used during the NOνA era is upgraded for a medium energy neutrino configuration that NOνA required, and fixed between 135 cm and 15 cm upstream of the first horn. Figure 2.4 and 2.5 shows the longitudinal and horizontal cross-section view of the target. It consists of twelve 6.4 mm thick and 100 mm long graphite plates, and water cooled through channels that running along the bottom plate of the plates. To better relieve the thermal stresses from high energy proton collisions, the upper half of each graphite plate is segmented longitudinally into 4 graphite fins with each 22 mm in length and 30 mm in height.

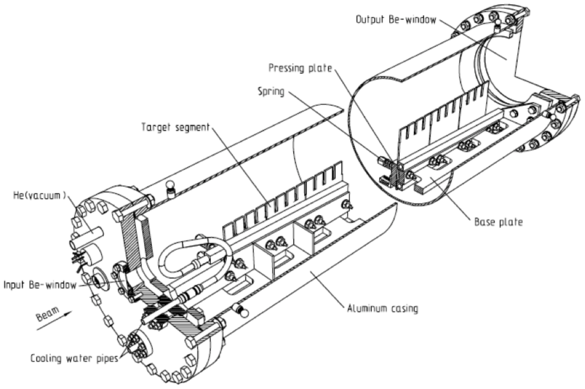
Output Be-window
Pressing plate
Spring
Target segment
He(vacuum)
Base plate
Input Be-window
Beam
Aluminum casing
Cooling water pipes

FIG. 2.4: Longitudinal Cross-Section of the NuMI Target and the Target Canister [13].

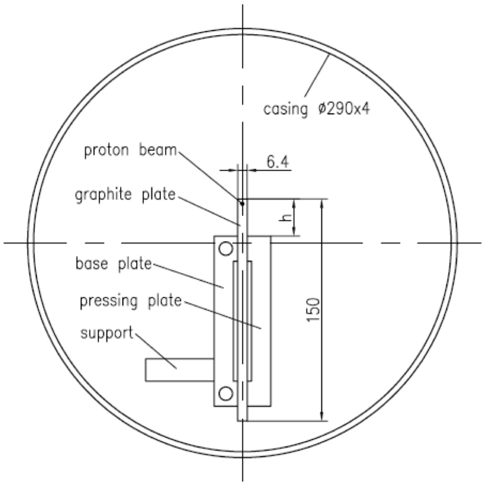
casing ø290x4
proton beam
6.4
graphite plate
h
base plate
pressing plate
150
support

FIG. 2.5: Horizontal Cross-Section of the NuMI Target and the Target Canister [13].

2.2.3 Electromagnetic Focusing Horns

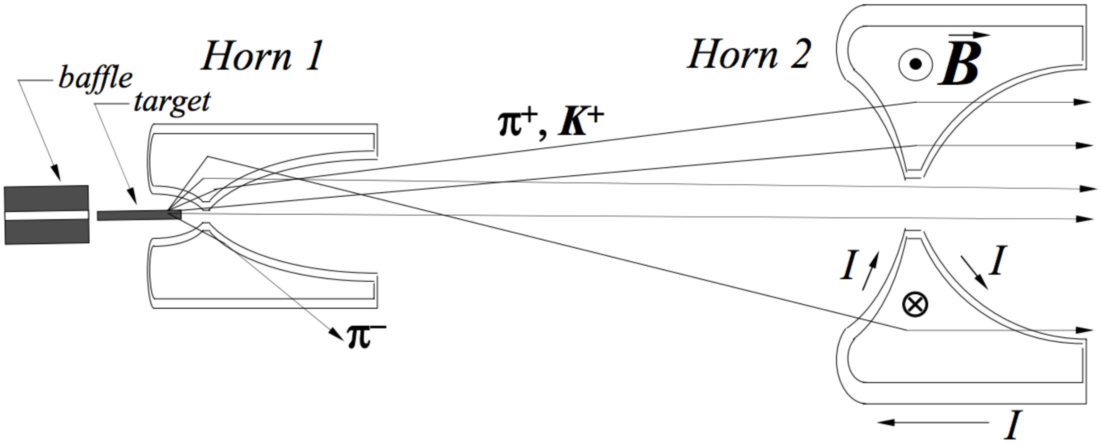

FIG. 2.6: Schematic view of the NuMI focusing horns which are pulsed in “forward” mode. Hadrons produced by the NuMI target are focused by these pair of magnetic horns, the relative position of which can be adjusted to change the energy profile of the beam [14].

The secondary particles (primarily π and K) produced in the target are then focused into a collimated beam by a pair of magnetic focusing horns for charge-sign and momentum selection. As shown in Figure 2.6, these horns consist of cylindrical shaped outer conductors, and parabolic-shaped inner conductors that produce magnetic fields to function as lenses. The two focusing horns are operated in pulsed mode with a nominal current of 200 kA to produce a maximum 30 kG toroidal magnetic focusing fields. Two polarity modes of the horns can be set to select different charge-signs of the particles. The “forward” horn current setting, which is the standard configuration, focuses positively charged mesons (mainly π^+ and K^+), which will later decay into muon neutrinos, while the “reverse” horn current mode selects π^- and K^- and produce the muon antineutrinos. Some opposite sign mesons can escape through the center of the horn necks and decay into the antiparticles backgrounds [68].

2.2.4 Decay Volume and Absorber

After focusing by the horns, the hadron beam is directed down a 675 m long, 2 m diameter decay pipe filled with 0.9 atm helium. The pions and kaons decay along their path via the channels as below:

$$\pi^{\pm} \rightarrow \mu^{\pm} + \nu_{\mu}(\overline{\nu}_{\mu})$$
$$K^{\pm} \rightarrow \mu^{\pm} + \nu_{\mu}(\overline{\nu}_{\mu})$$

with a small fraction of $\overline{\nu}_{\mu}$ and ν_e produced primarily by the secondary decay:

$$\mu^{+} \rightarrow e^{+} + \overline{\nu}_{\mu} + \nu_e$$

The decay pipe is made of steel and sealed by a thin, aluminum-steel window in its entrance. The pipe is 675 m long, which is approximately one decay length of a 10 GeV pion, hence most of pions and kaons are able to decay by the end of the decay volume [68]. The 2 m diameter is a compromise between the loss of secondaries that interact with the wall of the pipe and the cost considerations. Surrounding the pipe, there is at least 2.5 m of concrete shielding, to prevent activation of ground water and soil, and water cooling lines to remove 150 kW of heating deposited by the beam. Since December 2007, the decay pipe, which was initially evacuated, is filled with helium gas to reduce the stress and the risk of the corrosion on the aluminum window in the entrance of the pipe.

At the end of the decay pipe, an ionization chamber array (labeled as "Hadron Monitor" in Figure 2.3) measures the flux and spatial profile of the hadrons. All remaining hadrons and protons are stopped by a metal absorber made of water-cooled steel and aluminum. The hadron absorber is too short to remove all the muons of the beam. Thus an additional 240 m of rock lies after the absorber to stop the muons from the meson decays, with three muon monitors at intervals in the rock to observe the rates and spatial profiles of the remaining muons [70, 71]. After passing through this set of instruments, the beam heads towards the detectors.

2.2.5 NuMI Upgrade

To supply the designed beam intensity for the NOνA experiment, the NuMI beam was subjected to a series of technical upgrades and adjustments. The location of Horn 2 was adjusted to generate the desired medium energy beam. The cycle-time for Main Injector was been reduced from 2.2 seconds to 1.33 seconds. These changes had already been completed in November 2014 and increase the beam power from 350 kW in the MINOS era to about 520 kW. Further upgrades of the Booster Radio-Frequency (RF) and full slip-stacking in the recycles are scheduled for completion in 2016 to eventually increase the beam power to 700 kW with 4.9×10^{13} protons per pulse [72].

2.3 Off-Axis Features

Instead of sitting on the central axis of the NuMI beam, both NOνA detectors are located 14.6 mrad off the NuMI beam axis. This technique generates a narrow-band neutrino beam and increases the signal to the background ratio. The rationale behind this technique is based on a feature of relativistic hadron decay kinematics [73]. In the two-body decay of the pions or kaons, we have conservation of four-momentum. Ignoring the mass of the neutrino and plugging in known parameters, we can then describe the neutrino energy E_ν and flux ϕ in the pion rest frame as:

$$E_\nu = \frac{(1 - \frac{m_\mu^2}{m_\pi^2})E_\pi}{1 + \gamma^2\theta^2}, \tag{2.1}$$

$$\phi = \left(\frac{2\gamma}{1 + \gamma^2\theta^2}\right)^2 \frac{A}{4\pi\gamma^2} \tag{2.2}$$

where θ is the angle between the pion direction and the neutrino direction, m_π (m_μ) is the pion (muon) mass, E_π is the pion energy, γ is the Lorentz boost of the pion ($\gamma = \frac{1}{\sqrt{1-\beta^2}}$), and A is the cross-sectional area of the detector.

As illustrated in Figure 2.7, in the case $\theta = 0$, which means we detect the neutrino in the beam direction (like in MINOS), the neutrino energy spectrum seen in the lab frame has a broad distribution. However, when $\theta \neq 0$, there is a maximum neutrino energy for each different value of θ, and the energy of the neutrino only weakly depends on the pion energy. The beam has a narrow energy range and the mean energy can be varied by changing the off-axis angle as illustrated in Figure 2.8. In NOνA, the off-axis angle is set

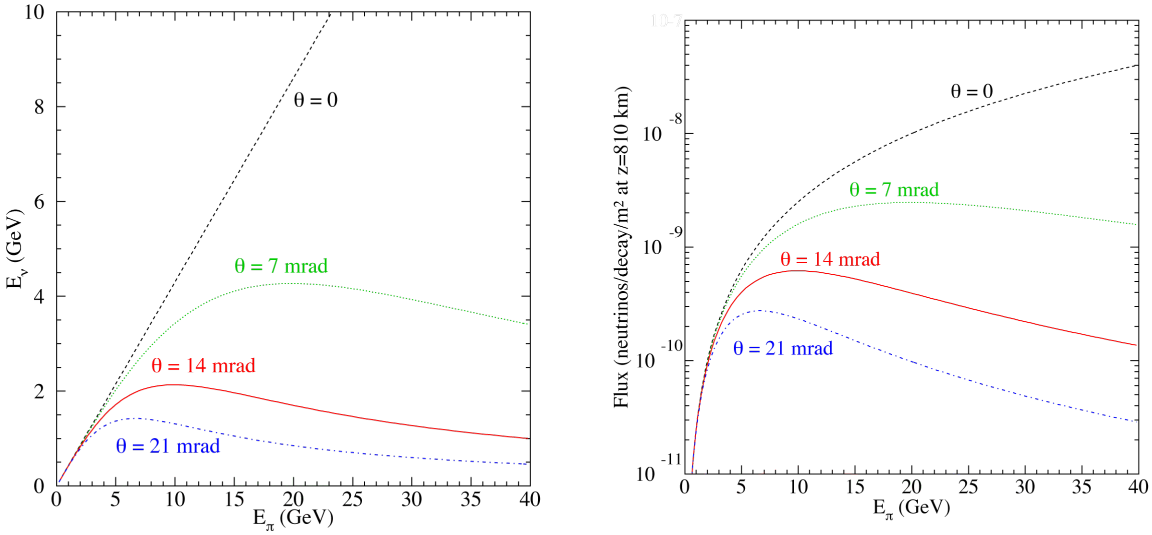

FIG. 2.7: The total neutrino flux at a given angle as a function of parent pion energy. The NOνA site is at 14 mrad [13].

to be 14.6 mrad off the NuMI beam axis so that the energy of the neutrino beam peaks around 2 GeV, which is near the first oscillation probability maximum at 810 km baseline.

In addition to concentrating the neutrino flux at the energy most sensitive to oscillations, another main advantage of siting the detectors off-axis is to enhance the background rejection and consequently increase the signal-to-background ratio. In the ν_e appearance measurement, high energy neutral-current events, in which the neutrino takes away a majority part of the initial energy and produces an event topology quite similar to a low energy ν_e CC event, is a background source that is hard to eliminate during analysis. Figure 2.9 shows the number of different types of events as a function of their visible energy. We can see that by constraining the neutrino energy spectrum into a narrow band, the high energy neutral-current events are significantly reduced.

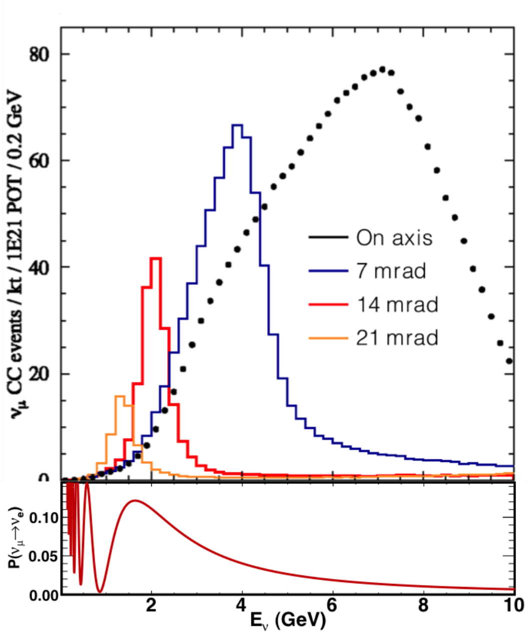

FIG. 2.8: The total neutrino flux at a given angle as a function of parent pion energy. The NOνA site is at 14 mrad [13].

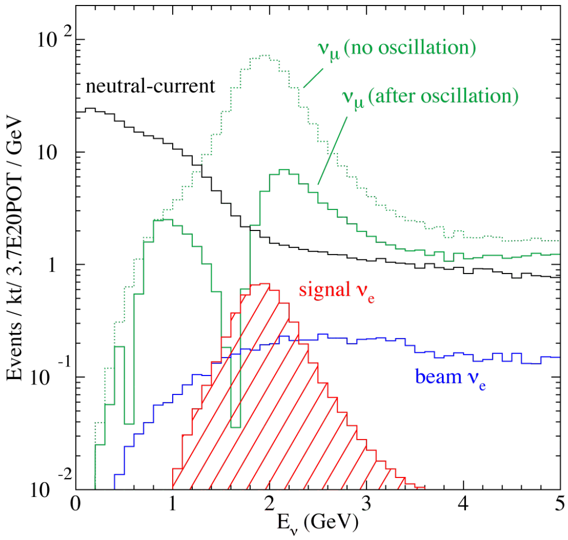

FIG. 2.9: Simulated energy spectrum in the NOνA far detector for different event components: beam and signal ν_eCC , ν_μCC and NC.

CHAPTER 3

The NOνA Detector

3.1 The NOνA Detector Design

The NOνA experiment uses two functionally equivalent detectors. Both sit off-axis from the NuMI beam, as illustrated in Figure 4.1, to perform the measurement. The following sections describe each of the major detector components and how they record neutrino interactions.

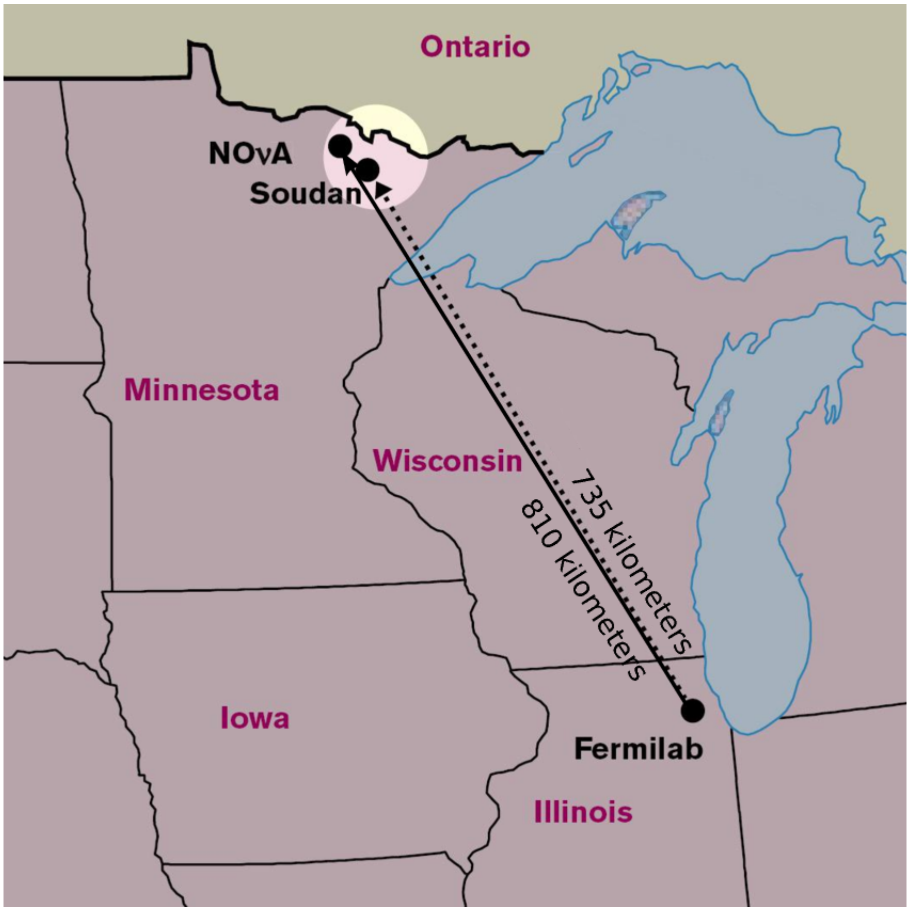
Ontario
NOνA
Soudan
Minnesota
Wisconsin
735 kilometers
810 kilometers
Iowa
Fermilab
Illinois

FIG. 3.1: The location of the two NOνA detectors. The NuMI beam created at Fermilab travels 810 km through the Earth and reaches the Far detector in Minnesota. The Near detector is located near the source of the NuMI beamline to measure the initial properties of the beam [15].

3.1.1 The Basic NOνA Detector Element

The basic unit of both NOνA detectors is an extruded cell of PVC plastic that is filled with liquid scintillator and a looped wavelength-shifting optical fiber (as shown in Figure 3.2). Each cell is 3.9 cm wide and 5.9 cm in deep. They are 15.5 m long in the Far detector and 4 m long in the Near detector. The wall of the cell is 3.3 - 4.8 mm thick and made highly reflective using titanium dioxide, which is 90% reflective for scintillator light of $400 - 450\,\mathrm{nm}$ [13]. The large numbers of cells ($344,064$ in FD, $18,432$ in ND) are designed to provide scintillator containment and structural support to the massive detectors. The high segmentation allows for high resolution tracking of final state particles created in neutrino interactions.

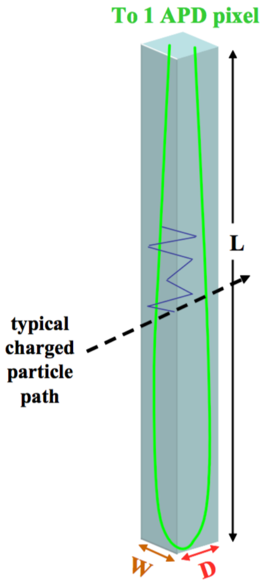

FIG. 3.2: A PVC cell of dimensions (W, D, L) containing liquid scintillator and a wavelength-shifting fiber (green). A charged particle incident on the front face produces light (blue line) that bounces off the cell walls until absorbed by the fiber. The fiber routes the light to the end of the APD to the optical read out [13].

Component	Purpose	Mass fraction	Mass (kg)	Mass fraction	Mass (kg)
		blends: #1, #2		blends: #3 ∼ #25	
mineral oil	solvent	94.91%	691, 179	94.63%	7, 658, 656
pseudocumene	scintillant	4.98%	36, 2677	5.23%	423, 278
PPO	waveshifter	0.11%	801	0.14%	11, 331
bis-MSB	waveshifter	0.0016%	11.7	0.0016%$	129
Stadis-425	antistatic	0.001%	7.3	0.001%$	81
Vitamin E	antioxidant	0.001%	7.1	0.001%	78
Total			728, 247		8, 093, 264

TABLE 3.1: The composition of NOvA liquid scintillator [3].

3.1.2 Liquid Scintillator

The 2.7 million gallons of liquid scintillator inside the cells makes up 65% of the total NOνA detector mass. The scintillator is mainly used to absorb the energy of the charged particles passing through and convert it to observable light. Its primary components are 95% mineral oil as solvent to blend all the components, and 5% pseudocumene as scintillant to generate UV light in the range $270-320$ nm [3]. In order to convert these UV light into the visible range ($380-450$ nm) of the wavelength-shifting fiber, two wavelength shifters PPO and bis-MSB are added into the solution at sub-percent levels. The scintillator also contains small amounts of Stadis-425 as antistatic, and Vitamin E as antioxidant. More details of the composition of the NOνA liquid scintillator is given in Table 3.1 [3].

3.1.3 Wavelength-Shifting Fiber

In each of the detector cells, a wavelength-shifting fiber is placed in a loop and runs the length of the cell (as illustrated in Figure 3.2). This looped placement maximizes the light-collection ability while improving the efficiency compared to two separate strands of fiber. The optical fiber is double-clad, 0.7 mm in diameter, and contains wave-length shifting agents Y11 dye within its core [13]. The blue light ($380 - 450$ nm) emitted by the scintillator is captured by the fiber and wavelength shifted to green light with wavelength in range $450 - 650$ nm [13]. The light is trapped inside the fiber by internal reflection and travels down to the ends of the fiber, where it is directed to an avalanche photodiode (APD) for readout (see Figure 3.3(a)).

3.1.4 Photodetector and Electronics

The photodetector that NOνA uses is a 32 pixel Hamamatsu avalanche photodiode (APD) (see Figure 3.3(b)). It is custom designed for NOνA to fit both ends of the looped fiber onto the same APD pixel to maximize light collection. Figure 3.3 shows that fibers from 32 cells of a single PVC module map directly onto the 32 pixels of APD [13].

For the $500-550$ nm wavelengths of light directed by the fiber, the NOνA APD has an 85% quantum efficiency. This efficiency is much higher than the traditional photomultiplier tubes (PMT) (see Figure 3.4) and therefore enables the detection of light produced at the end of a very long module, which is 15 m long in the NOνA Far detector. The APDs are operated at a gain of 100, which is achived at a voltage of 400 V. To reduce the noise

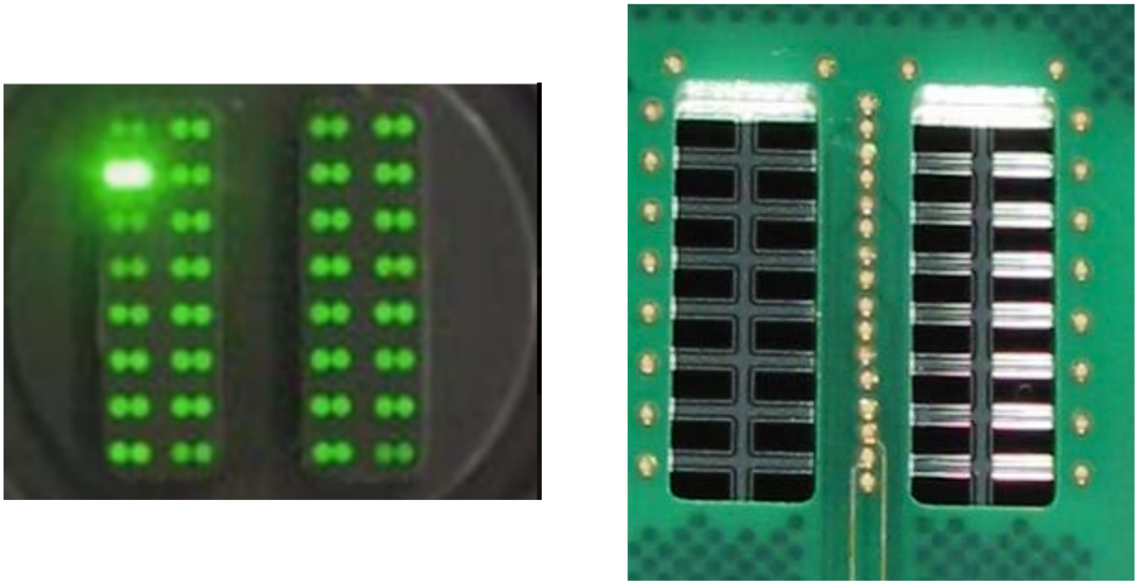

FIG. 3.3: a)The ends of 32 wavelength-shifting fibers at the end of scinillation cells to interface with an APD. b) Front face of an APD that will be pressed against the fiber ends [13].

generated by thermal current, each APD is cooled to $-15°C$ with its own thermoelectric cooler (TEC). The heat from the TECs is continuously removed by a water cooling system to maintain a $-15°C$ operation temperature [13]. To keep the APD surface clean and dry, which is important for reducing surface charge buildup, the APD is coated with transparent parylene and ventilated with dry-air to remove moisture.

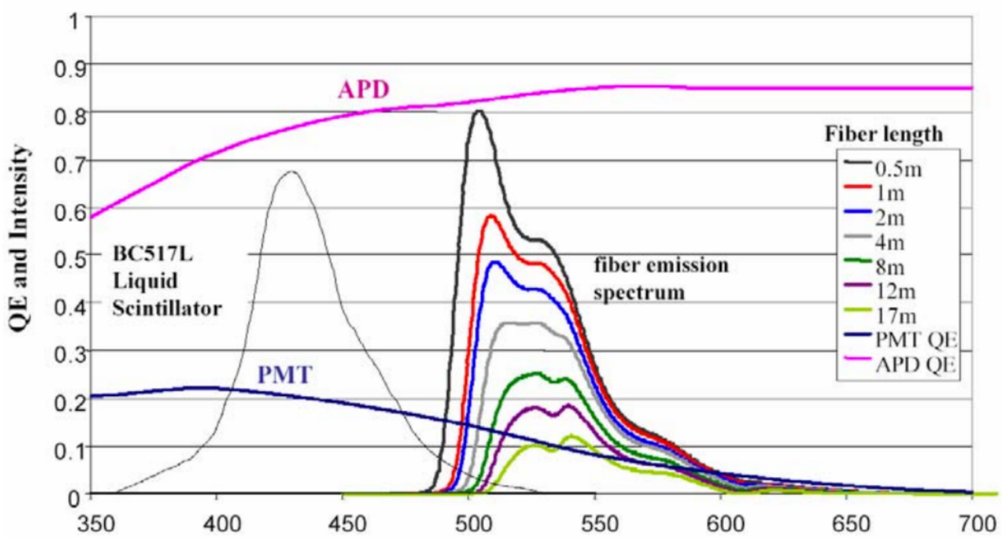

FIG. 3.4: The quantum efficiencies of the APDs (magenta) and PMTs (blue) are shown in comparison to the average detected wavelength as fiber length increases [13].

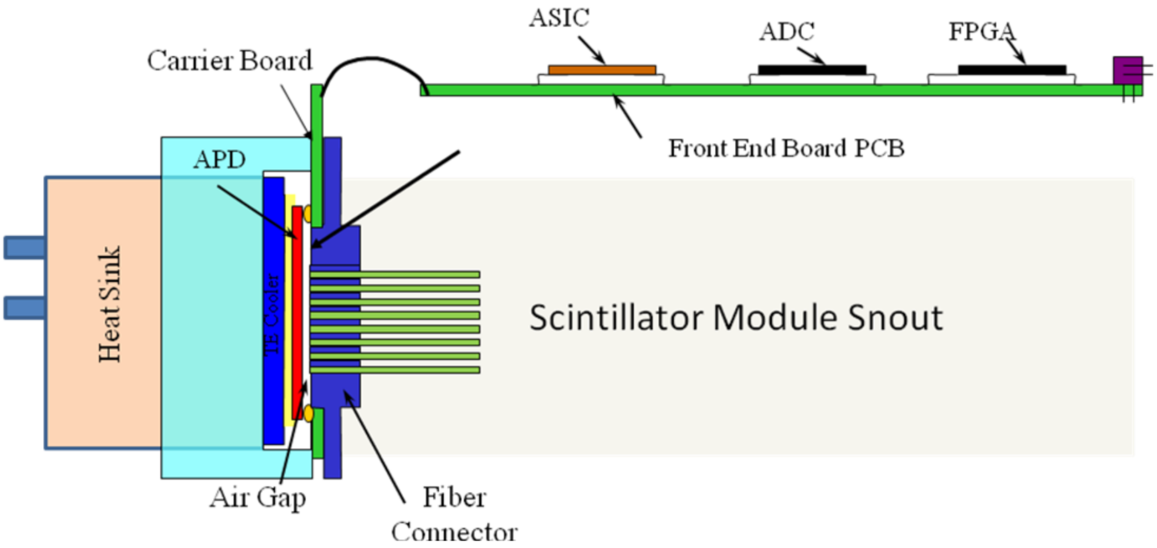
ASIC
ADC
FPGA
Carrier Board
Front End Board PCB
APD
Heat Sink
TE Cooler
Scintillator Module Snout
Air Gap
Fiber
Connector

FIG. 3.5: Schematic of the APD module and the Front End Board (FEB) showing the major components [13].

In the APD, optical signals from the detector module are converted into electronic signals, amplified by a factor of 100, and passed to a Front End Board (FEB) through a short ribbon cable (as shown in Figure 3.5). The FEB, each of which connects to one APD, time stamps and digitizes the signals above a threshold based on a dual correlated sampling (DCS) algorithm [13]. The signals from up to 64 FEB then pass to a Data Concentrator Module (DCM) with 1 GB uplink speed [13].

This whole readout chain is called the data acquisition system (DAQ), which collects the data from all the APD channels in the detector and transform them into a data stream that can be analyzed and archived (as shown in Figure 3.6). The DAQ system also consists of a timing and command distribution system that records the time stamp of the hits. Each of the basic unit of the system, time distribution unit (TDU), synchronizes one diblock or 1 kT of the NOνA detector to the main time distribution unit (MTDU). The MTDU is further synchronized to a Global Positioning System (GPS) trained clock, the same as the NuMI beam facility, to keep the timing information of the NOνA detectors consistent with the NuMI beam [13].

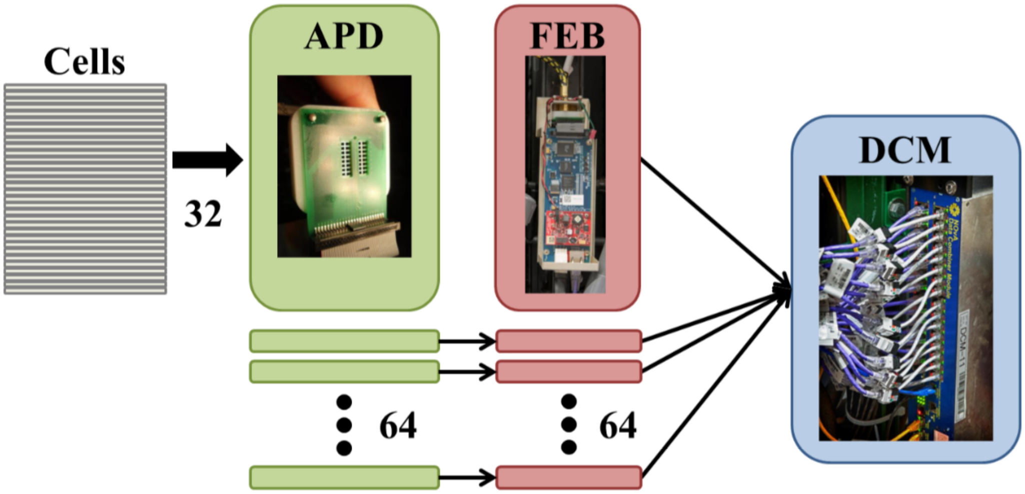
Cells
32
APD
FEB
DCM
64
64

FIG. 3.6: Architecture of NOνA Data acquisition system (DAQ) [13].

3.1.5 PVC Modules

The basic building blocks of the NOνA detectors are rigid PVC extrusions with 16 cells extruded together. They make about 30% of the total NOνA detector mass and serve as the structure of the whole detector. Hence the design of the PVC must meet the the minimum strength requirements in both thickness and shape. Figure 3.7 shows the shape of the PVC extrusion. The scalloped rounded corners is designed to reduce the stress concentration on corners and therefore minimizes the creep [13].

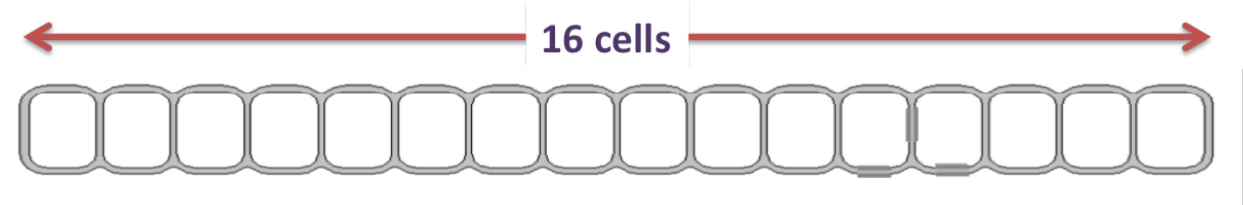

FIG. 3.7: Drawing of the NOνA rigid PVC extrusion.

Each NOνA detector plane is made of several flat 32-cell modules, formed by gluing together a pair of PVC extrusions side-by-side. As shown in Figure 3.8, these modules are rotated orthogonally to its neighbors when stacked into detecter blocks, which enables the three dimensional tracking of particles. After adding a manifold to the top and a reflective plastic plate to the end, the extrusion module forms the primary containment vessels for the liquid scintillator. A snout installed at one end of the manifold routes the WLS fiber to the optical connector and holds the electronic box, which houses the APD and FEB. The whole module assembly is shown in Figure 3.9.

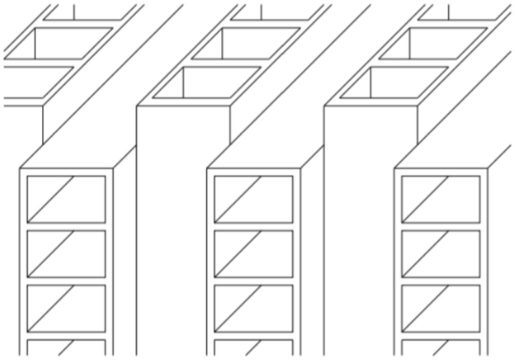

FIG. 3.8: Cells in adjacent planes are orthogonally rotated with respect to one another. Figure from [16]

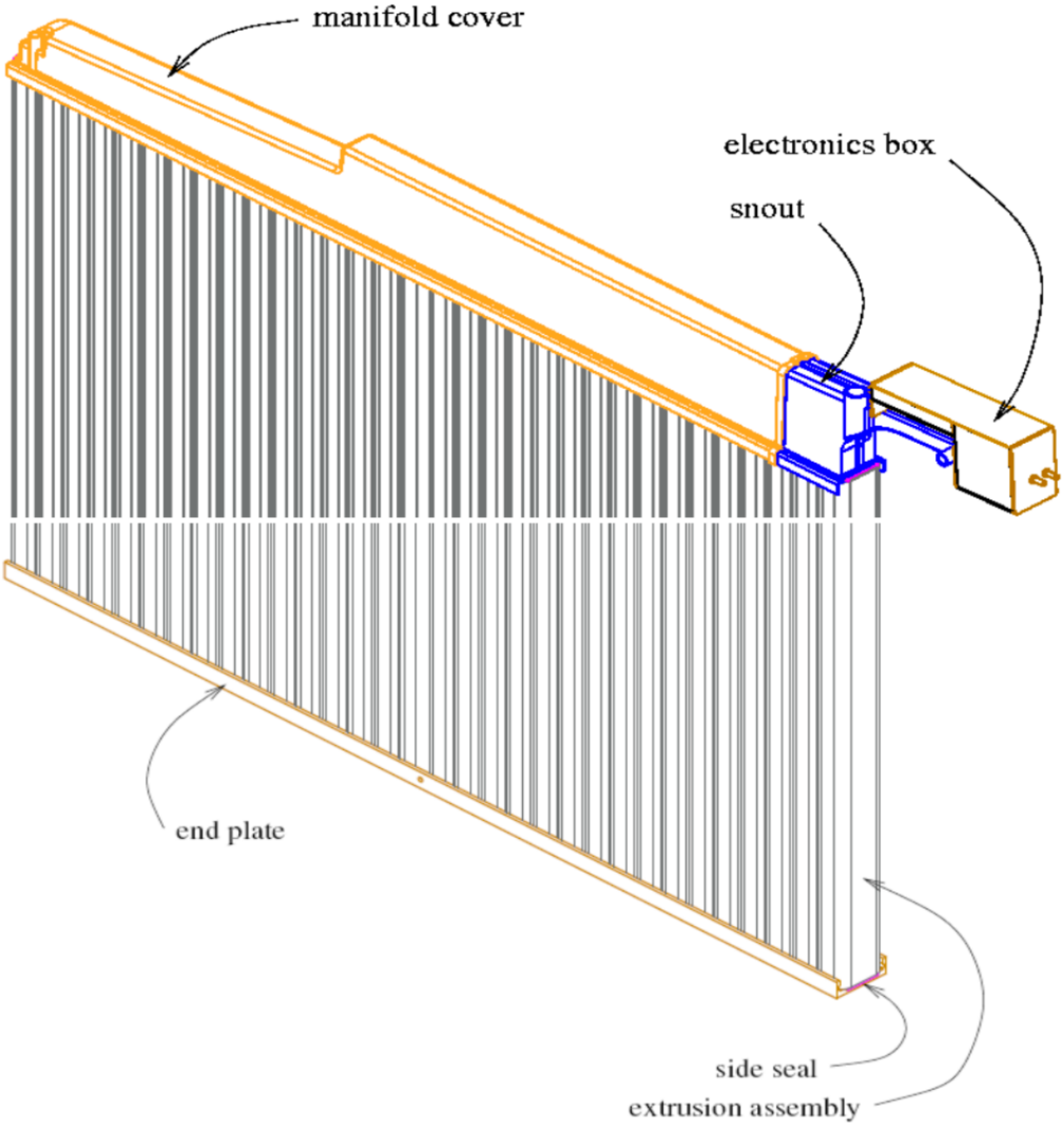
manifold cover
electronics box
snout
end plate
side seal
extrusion assembly

FIG. 3.9: Schematic of NOνA extrusion module. It is constructed from two side by side 16 cell PVC extrusions and capped at both ends to contain the liquid scintillator. The manifold end also routes the 64 fiber ends to a cookie, which couples to the avalanche photodiode array and associated electronics [13].

3.2 Assembly of NOνA Detectors

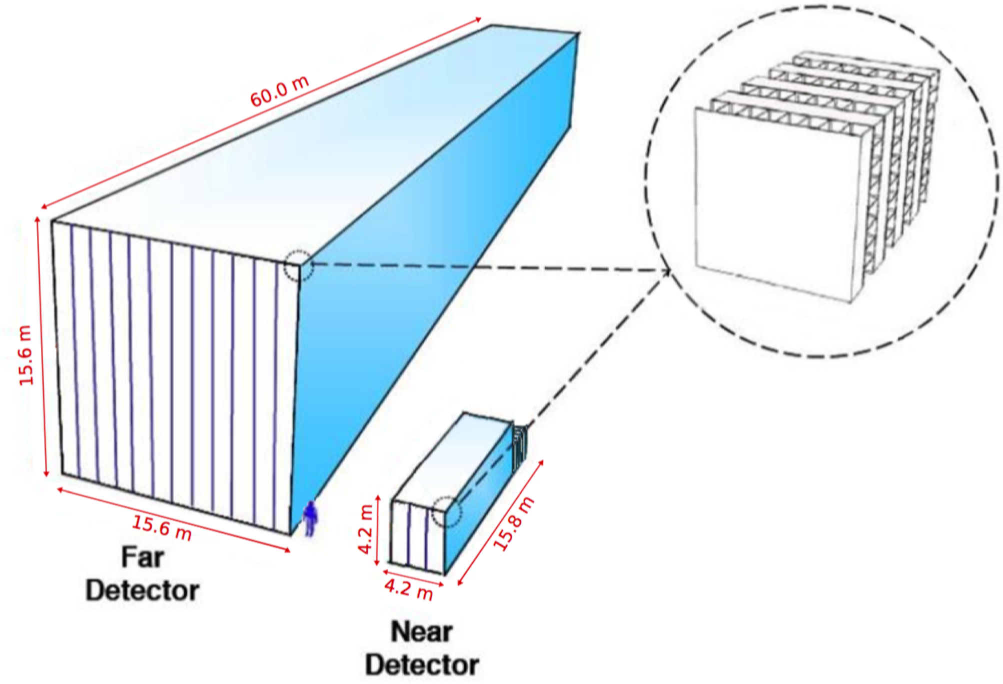

FIG. 3.10: There are two functionally identical NOνA detectors in the NOνA experiment: the Far Detector at Ash River, and the Near Detector at Fermilab. The diagram shows the relative sizes of the two detectors.

The Far Detector

810 km from the NuMI beam source at Fermilab, the NOνA Far detector is located in northern Minnesota in Ash River. Unlike most of the neutrino detectors that sit deep underground, the NOνA Far detector is constructed on the surface under a thick concrete and rock layer used as a cosmic-ray shield. NOνA relies on the high-resolution 3-D tracking and a narrow trigger window of the detectors to reject cosmic rays effectively.

The Far detector has a mass of 14 kilotons and dimensions of $15.6 \times 15.6 \times 60$ meters.

Twelve 32-cell modules were glued side-by-side together to form a plane. Thirty two of these planes are grouped in alternating vertical and horizontal orientations to form a block. A diblock, each of which combines the two adjacent blocks, is the unit used in electronics instrumentation and readout. The whole Far detector is constructed in 14 diblocks, which is 28 blocks, and consists of 896 planes in total [13]. Figure 3.11 shows the fully assembled Far detector with its pivoter, which was used to move the blocks into place, left against the last block as support.

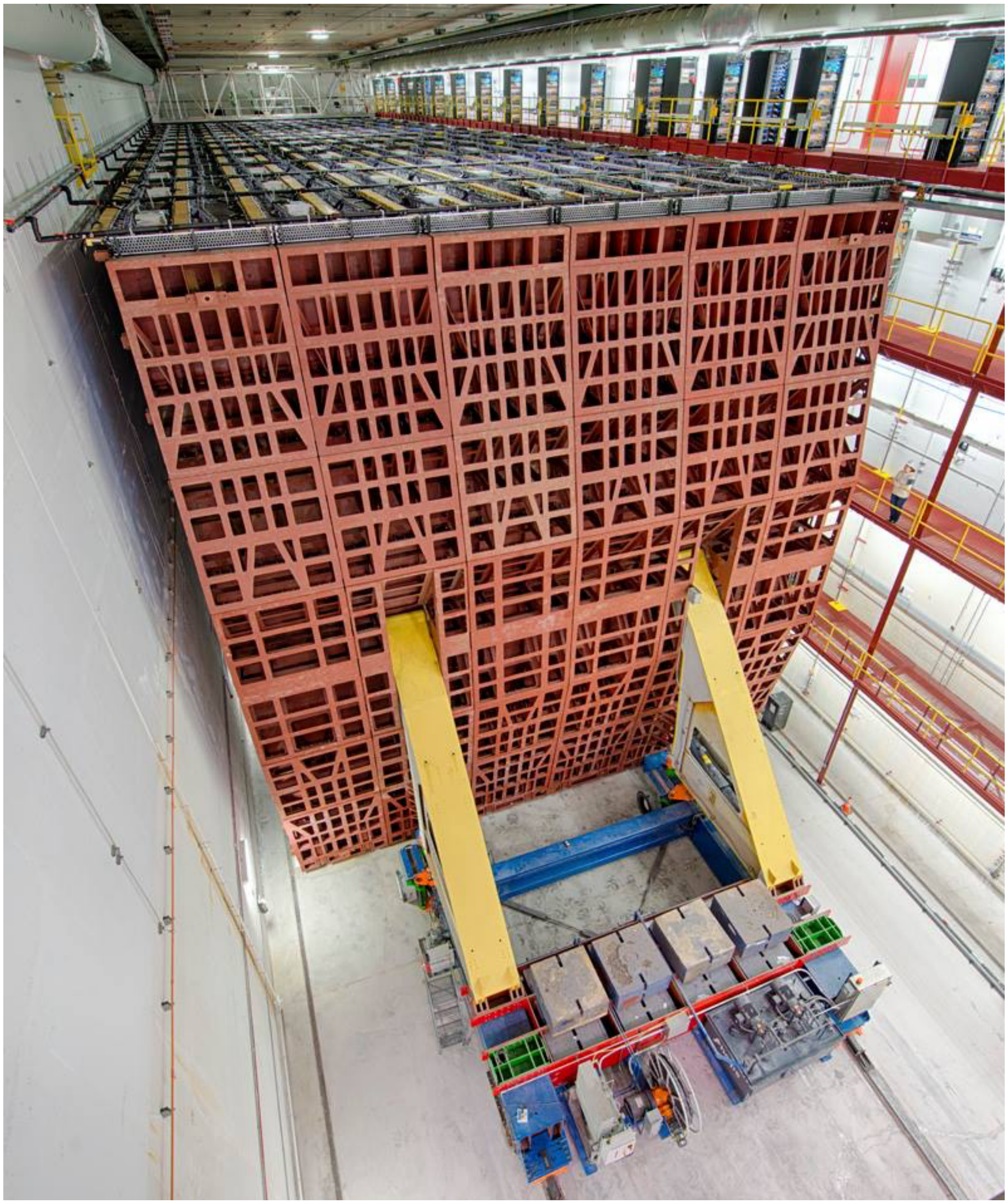

FIG. 3.11: NOνA Far Detector (courtesy of Fermilab Visual Media Services).

The Near Detector

The NOνA Near detector sits 100 m underground on the Fermilab site, adjacent to the MINOS cavern. The Near detector consists of two regions, an active region that makes the measurement (Figure 3.12(A)), followed by a muon catcher region at the downstream end to capture the runaway muons (Figure 3.12(B)). Figure 3.12 shows the fully constructed Near detector in its cavern viewed from upstream in the NUMI beam.

The active region of the Near detector is an identical copy of the Far detector except it is much smaller as shown in Figure 3.10. It has 8 blocks, with each block made of 24 planes, and each plane consists of 3 PVC modules. In total, the active region has 192 planes and dimensions of $4.1 \times 4.1 \times 12.8$ meters. For electronics readout, the active region has been partitioned into three 64-plane diblocks, each with 2 DCMs for the vertical view and 2 DCMs for the horizontal view.

The muon catcher consists of 22 scintillator planes and ten 4.03 inch-thick steel planes interspersed between horizontal and vertical scintillator planes. The muon catcher is 3.1 m in length, the same as the active region in width, and 2/3 the height of the active region. There are 2 DCMs instrumented for each of the horizontal and vertical views in the muon catcher.

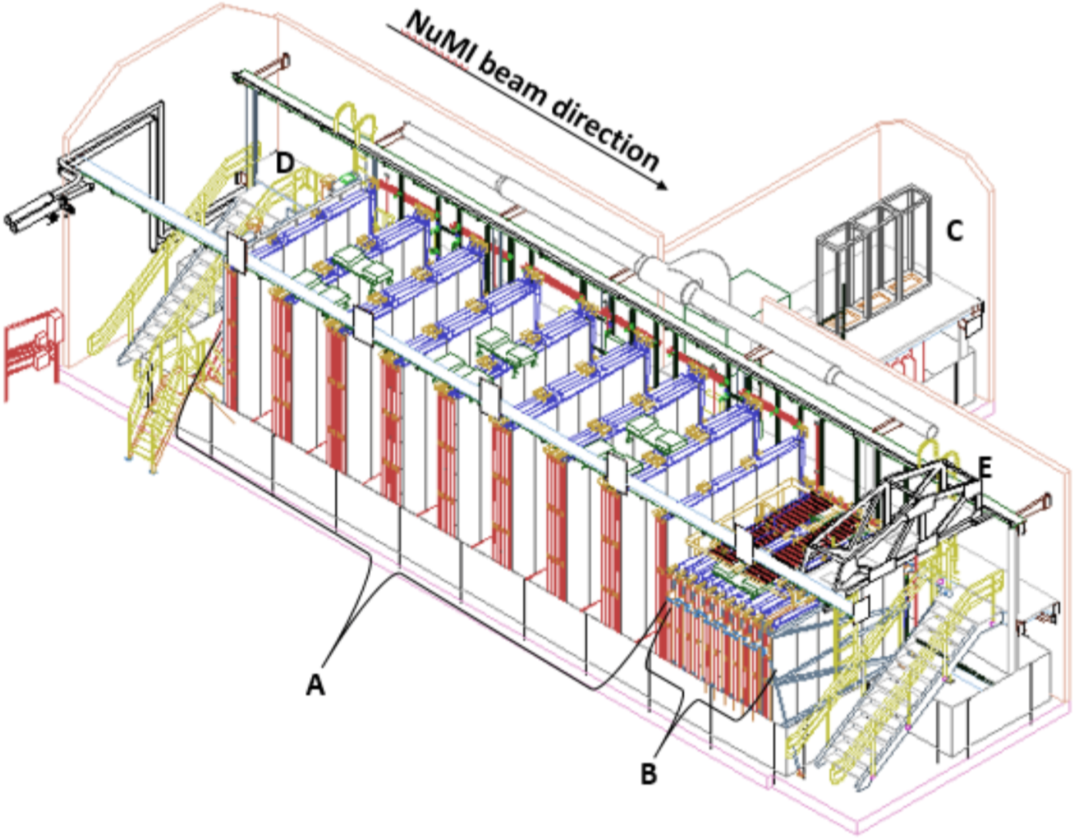
NuMI beam direction
A
B
C
D
E

FIG. 3.12: A schematic view of the NOνA Near Detector. A) 3×3 module active region. B) 3×2 module muon catcher region. C) Electronics rack alcove. D) Catwalks. E) Movable access platform [17].

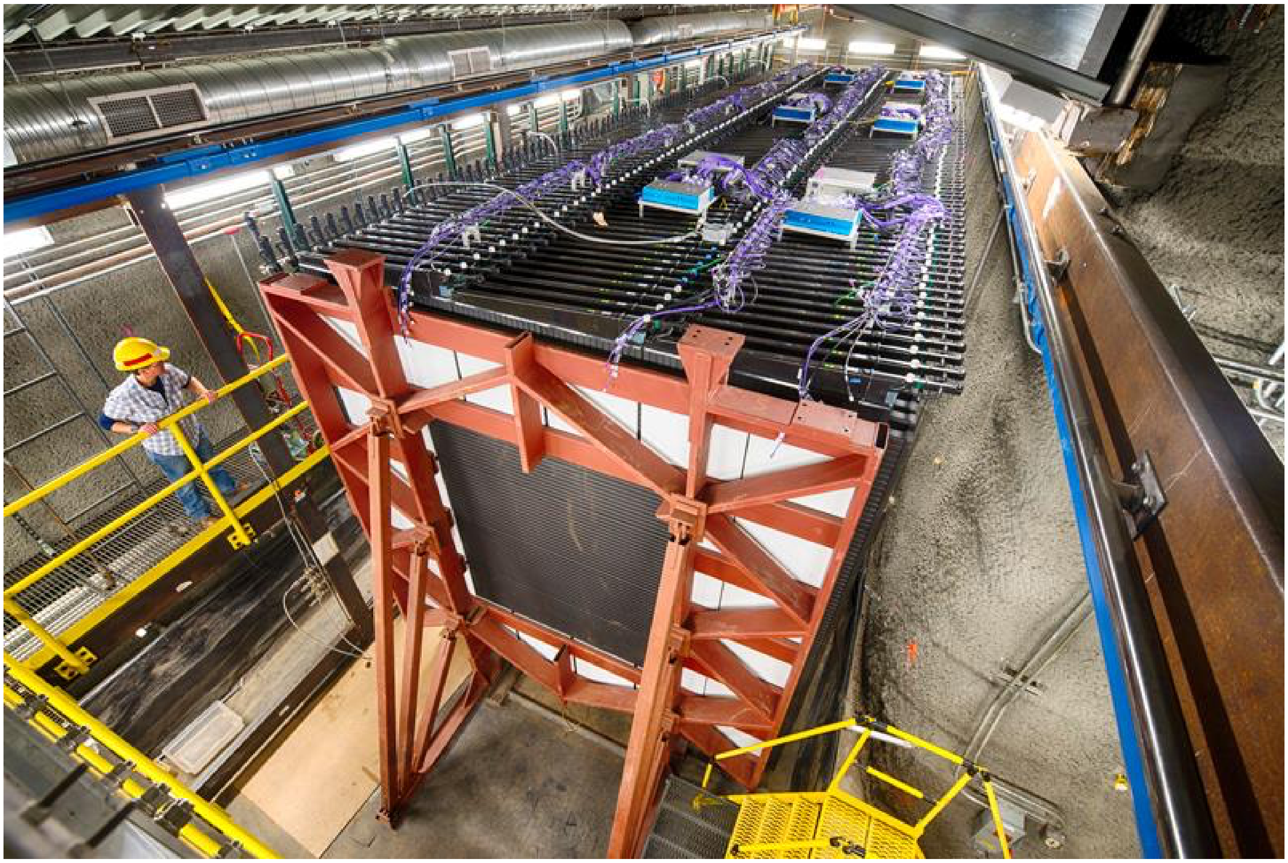

FIG. 3.13: NOνA Near Detector (courtesy of Fermilab Visual Media Services).

CHAPTER 4

Monte Carlo Simulation

4.1 NOνA Simulation Chain

In High Energy experiments, a Monte Carlo simulation is built to better understand how the particles interact with detectors. In NOνA, the simulation files are generated through several steps as illustrated in Figure 4.1.

Simulation at NOνA is a multi-stage chain. It starts with the simulation of neutrino production in the NuMI beamline. This step models hadrons produced by protons interacting with the target, focused in the horns, and decayed into neutrinos using the FLUKA simulation package [74] and FLUGG GEANT4 geometry interface [75]. The output is a flux file documenting the properties of the simulated neutrino beam, such as flavor composition, energy, momentum, and its parentage information. This allows us to reweight the beam neutrino spectra for systematic error calculations, without rerunning

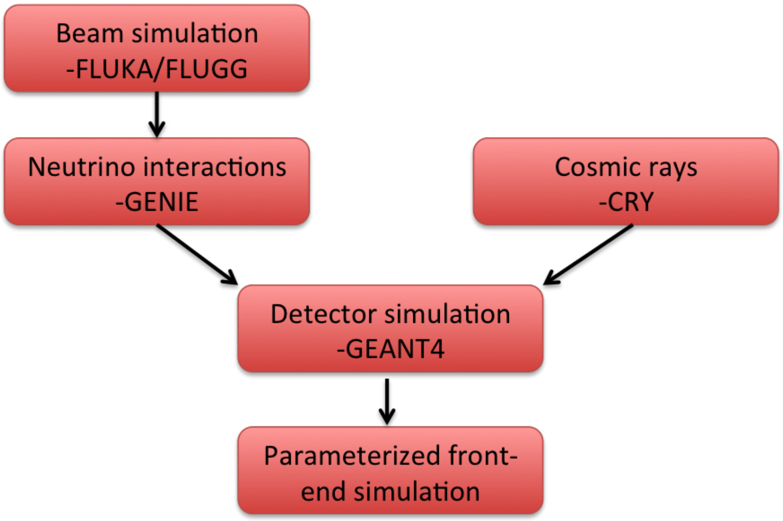
Beam simulation
-FLUKA/FLUGG
Neutrino interactions
-GENIE
Cosmic rays
-CRY
Detector simulation
-GEANT4
Parameterized front-end simulation

FIG. 4.1: Steps in simulation chain for the NOνA experiment.

the computationally intensive simulation.

The flux files are then passed to the next stage which uses the GENIE, neutrino event generator package [76, 18], combining cross section models to simulate neutrino interactions in the NOνA detectors. More details about GENIE will be discussed in the next section. For the NOνA Far detector, the cosmic rays are significant backgrounds since it sits on surface. Thus we specifically use the CRY (Cosmic Ray) generator [77] to simulate these cosmic ray events.

Next, the cosmic events are overlaid with the beam neutrino events, and these are used as the inputs to the detector simulation performed by GEANT4 [78]. It uses the NOνA detector geometry and material features to determine how each particle interacts with the detector, to propagate the secondary products of neutrino interactions through the detector step by step, and to simulate the energy deposition in the active material. The physics list that NOνA uses to model all the possible hadronic interaction for each particle is *QGSP_BERT_HP*. While QGSP (Quark-Gluon String Precompound) model is used to handle the collision of a high-energy hadrons, BERT (Bertini) cascade takes care of the hadrons below ~10 GeV, and HP (High Precision) is used to transport neutrons below ~20 MeV at high precision [78].

The last step in the chain simulates the response of the NOνA detectors. Signal attenuation in the fiber, and background noise fluctuations are taken into account. These simulate the whole process of correcting energy deposited into scintillation light, propagation to the APD, and modeling of the electronic response. The final product of the simulation chain is saved in a ROOT file, in the same format as raw data from the NOνA detectors, except it contains additional truth information for later analysis.

4.2 Neutrino Interaction Physics Models in GENIE

GENIE *(Generates Events for Neutrino Interaction Experiments)* is a ROOT-based Neutrino MC Generator [76] and has been widely adopted by many neutrino experiments. GENIE includes many theoretical models, each of which describe a subset of the neutrino-nucleus interaction processes. These physics models can be roughly classified into three categories: cross section models, hadronization models and nuclear physics models, each of which will be discussed in more detail in the following sections.

4.2.1 Cross Section Model

The cross section model in GENIE is used with the flux information to calculate the differential and total cross sections. It then uses the cross sections for specific processes to determine which interaction type will occur, while using the differential cross section for that interaction to calculate the final state kinematics. There are a number of different 'targets' that a neutrino within different energy ranges can scatter off of, including the whole nucleus, individual nucleons, quarks within the nucleons, and atomic electrons. Below the three major scattering processes are described in more detail.

Quasi-elastic Scattering

Quasi-elastic scattering is one of the most common neutrino interactions in the NOνA detectors. This interaction can be formulated as:

$$\nu + n \rightarrow l^- + p \qquad\qquad or \qquad\qquad \bar{\nu} + p \rightarrow l^+ + n$$

with ν, $\bar{\nu}$, $l^{\pm}$, p and n standing for: neutrino, antineutrino, charged lepton, proton and neutron, respectively.

In GENIE, quasi-elastic scattering is implemented by the Llewellyn-Smith model [18], in which the hadronic weak current is modeled in terms of three Lorentz-invariant form factors. The two vector form factors $F_{1,2}(Q^2)$ are pseudo-scalar form factors, which is based on the partially conserved axial current (PCAC) hypothesis. As a result, the axial-vector form factor $F_A(Q^2)$ at $Q^2 = 0$ with one free parameter axial mass M_A is left as the only unknown quantity [79].

Baryon Resonance Production

The process of baryon resonance production is:

$$\nu + N \rightarrow l + N^*$$

where N^* denotes the nucleon resonance and the lepton l is either charged or neutral.

In GENIE the baryon resonance production is modeled by the Rein-Sehgal model that inherits the relativistic quark model of Feynman-Kislinger-Ravndal for baryon resonances [18]. This model obeys $SU(6)$ spin flavor symmetry and includes the helicity amplitudes of 16 resonances to construct the cross sections for neutrino-production of baryon resonances. In the model the lepton mass terms are neglected when calculating the differential cross section, but its effect on the phase space boundaries is taken into account [18].

Non-Resonace Inelastic Scattering

Non-Resonace Inelastic Scattering, also referred to Deep Inelastic Scattering (DIS), is a process where a neutrino scatters off a nucleon and breaks it into many hadrons. GENIE calculates this process at low Q^2 using the Bodek-Yang model. In this model the non-perturbative contributions to the inelastic cross section, including kinematic target mass corrections, dynamic higher twist effects, higher order Quantum Chromodynamic (QCD) terms, and nuclear effects on nuclear targets are calculated [18].

4.2.2 Neutrino-induced Hadron Production

In GENIE, the hadronization model is responsible for the calculation of the final state particles and their kinematics using the nature of neutrino-nucleon interaction (CC/NC, $\nu/\bar{\nu}$, target neutron/proton) and the event kinematics (W^2, Q^2, x, y). It is an important aspect of neutrino interaction simulation in the few-GeV range.

AGKY Hadronization Model

The hadronization model that NOνA used was developed by the MINOS experiment and named Andreopoulos-Gallagher-Kehayias-Yang (AGKY) model after its four developers [80]. At low invariant mass region, the AGKY model uses the Koba-Nielsen-Olesen (KNO) model [81] but with many improvements, while in the higher mass region it switches over to the PYTHIA/JETSET model [82] gradually to ensure the continuity of all simulated observables as a function of the invariant mass (see Figure 4.2). The AGKY hadronization model is tuned and validated using bubble chamber experimental data.

4.2.3 Intranuclear Hadron Transport

Although hadron production in neutrino-nucleon interactions are modeled by the AGKY model, these hadrons may reinteract with other nucleons on their way out of the nucleus, which could significantly modify the observable distributions in sampling

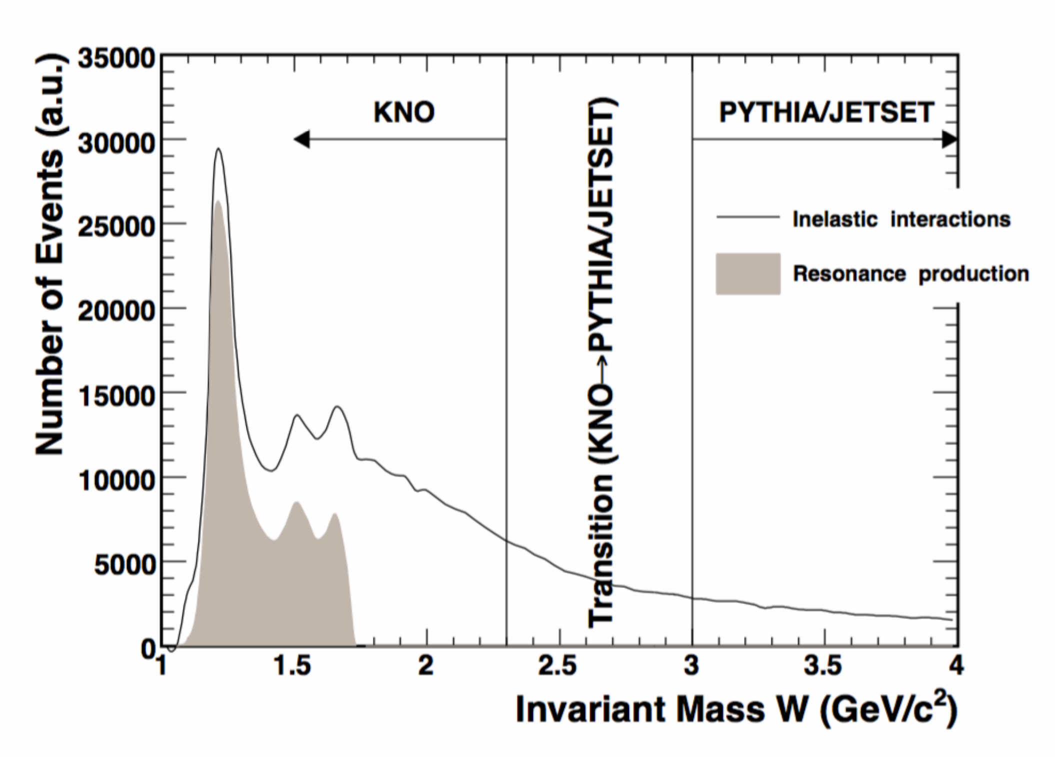

FIG. 4.2: Simulated invariant mass distribution of inelastic events in the MINOS Near Detector using the NuMI muon neutrino beam. The shaded area shows the resonance contribution for which a different hadronization model (Rein-Sehgal) is employed [18].

calorimeters like NOνA. This part in GENIE is simulated by a subpackage called INTRANUKE which was first developed by the Soudan 2 Collaboration and updated several times since [18].

INTRANUKE simulates the hadron intranuclear rescattering using a semiclassical model (intranuclear cascade model- INC). Hadrons are assigned a typical mean free path (MFP) of a few femtometers inside the nucleus. Then they propagate through the nucleus with a reduced interaction probability which is implemented as a "free step" in INTRANUKE. Lastly, combining the free hadron cross-sections and the density of nucleons, the final state interaction (FSI) rates are derived [78].

4.2.4 Nuclear Physics Model

Nuclear physics modeling plays an important role in the neutrino scattering simulation and introduces coupling between other models of the simulation. In GENIE, the nuclear physics simulation for all process is performed by the Relativistic Fermi Gas (RFG) nuclear model with the version of Bodek and Ritchie, which has been modified to introduce short range nucleon-nucleon correlations. This model is simple, yet applicable to a large range of target atoms and neutrino energies.

CHAPTER 5

Calibration and Event Reconstruction

This chapter describes in detail the calibration process that translates an amount of charge recorded in a pixel of an APD into a physically meaningful energy deposition in units of GeV. We also describe the reconstruction process that groups the hits coming from the same neutrino interaction and organizes them into an event and identifies daughter particle tracks.

5.1 Calibration

In NOνA, the calibration process consists of two main parts: the energy calibration and the timing calibration. The energy calibration [19] [83] applies several scale factors to convert the light measurement of each hit into an energy deposition based on its physical location. It can be further divided into two main sequential stages: an attenuation calibration and an absolute calibration. All of the energy calibration steps use cosmic rays as probes since they represent a source of well understood energy deposit across the detector. Those that stop, then decay into Michel electrons can be used to precisely calculate the absolute energy deposited in a cell.

The NOνA coordinate system sets the center of the detector's front face as the origin, and the downstream direction as the z-axis. Some of the calibration process units are defined below:

- ADC: A unit for "Analog to Digital" Conversion.
- PE: Stands for "Photo-Electrons", an unit that translates the ADC recorded by an APD to an amount of light incident on the APD.
- PECorr: The first calibrated unit correcting for attenuation and relative cell-to-cell differences.
- MIP: Energy in terms of the energy deposited by a minimum-ionizing particle traveling along the z-direction through the depth of one cell.
- GeV: Estimated energy deposited in the scintillator.

5.1.1 Attenuation Calibration

The first step of the energy calibration is the attenuation calibration that is applied to each detector cell to correct for cell-to-cell attenuation differences do to the WLS Fiber. After attenuation the energy unit is converted from ADC to PECorr. To do this calibration, the signal in a cell must be divided by the pathlength in a cell. Pathlength of each hit refers to the distance the particle travels in the cell, and is an important value for the attenuation calibration process since its distribution can be affected by reconstruction efficiency.

To select cells on a muon cosmic track, the tri-cell technique is applied as a quality cut. The tri-cell selection, as illustrated in Figure 5.1, requires that the adjacent cells in the same plane of the target cell are also on the track. Using tri-cell also gives us a accurate pathlength estimation through the cell.

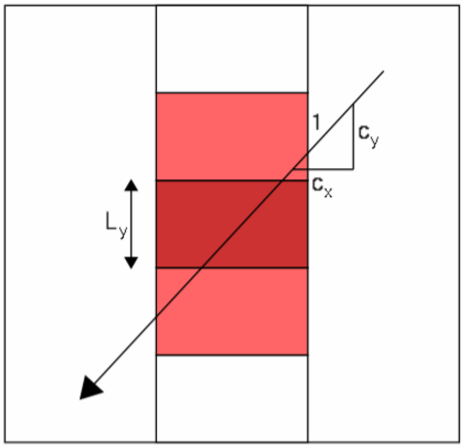

FIG. 5.1: Selection of tri-cells associated with a track. The dark red cell is a tricell because its neighbors are triggered by the same cosmic ray.

The ADC/cm of each selected cell can be expressed as a function of the distance W, which represents the distance along the cell's length to the readout and is determined by

3D track reconstruction. We then construct the profile of the 2D histogram (ADC/cm vs. W) by taking the median value in each W bin and fit it to the form:

$$y = C + A \left(exp\left(\frac{W}{X}\right) + exp\left(-\frac{L+W}{X}\right)\right) \tag{5.1}$$

where L is the length of the cell, and X is the attenuation length. Figure 5.4 shows an example of the attenuation fit for a good channel in the Near detector. For hits that are near the top and bottom of the cell, a "rolloff" effect is observed in data because of the different reflection behavior at the ends of the cells. To correct for this effect, an empirical function was introduced with the following form:

$$y' = \begin{cases} 1 - \alpha_R (W - W_R)^4 & W > +W_R \\ 1 & otherwise \\ 1 - \alpha_L (W - W_L)^4 & W > +W_R \end{cases} \tag{5.2}$$

Some of the cells still have large residuals after fitting to Equation 5.1 and 5.2, which could be due to varying fiber position within the cell or noisy behavior [19]. These residuals do not follow any consistent pattern thus can not be fitted by an additional function. To solve this issue, a LOWESS (Locally Weighted Scatter plot Smoothing) method is applied to better fit the curve.

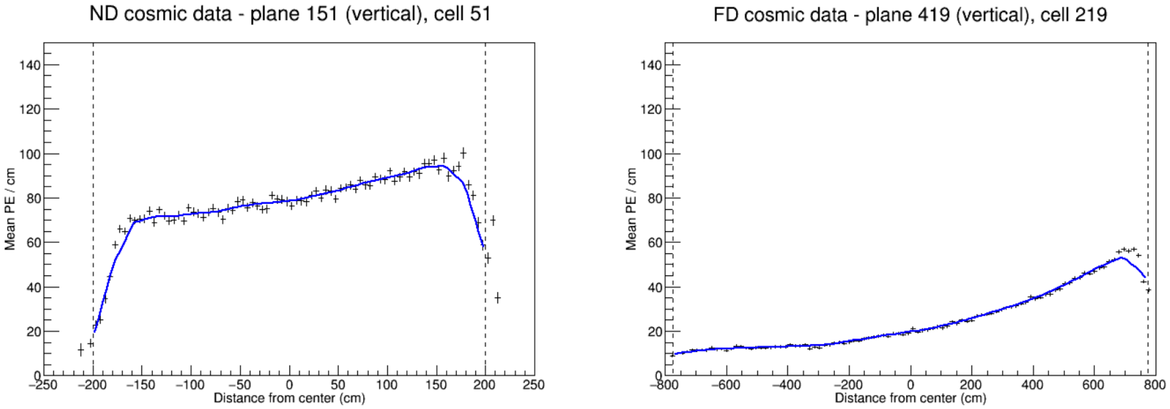

FIG. 5.2: Example attenuation fit for Near detector (left) and Far detector (right) using cosmic-ray data of a channel with deviations from an ideal shape, and the LOWESS fit through the residuals [19].

5.1.2 Absolute Energy Calibration

After the cell-to-cell attenuation calibration, the absolute energy calibration is performed to the whole detector to convert the energy scale from PECorr to GeV, the final reconstruction energy unit. For this process, the cosmic muons that stop in the NOνA detectors are used to calculate the calibration scale. This is because the energy loss dE/dx of the stopping muon decay is well described by the Bethe-Bloch curve (Figure 5.3) [83].

The cosmic-ray tracks are selected for the calibration if they stop inside the fiducial volume of the detectors. Using these track's information we can plot the 2D histogram, as of Figure 5.4, that shows the correlation between the energy loss along the pathlength, PECorr/cm, and the distance from the end of the track. By comparing this plot to the same distribution from simulation, the scale factor between PECorr and GeV can be calculated [83].

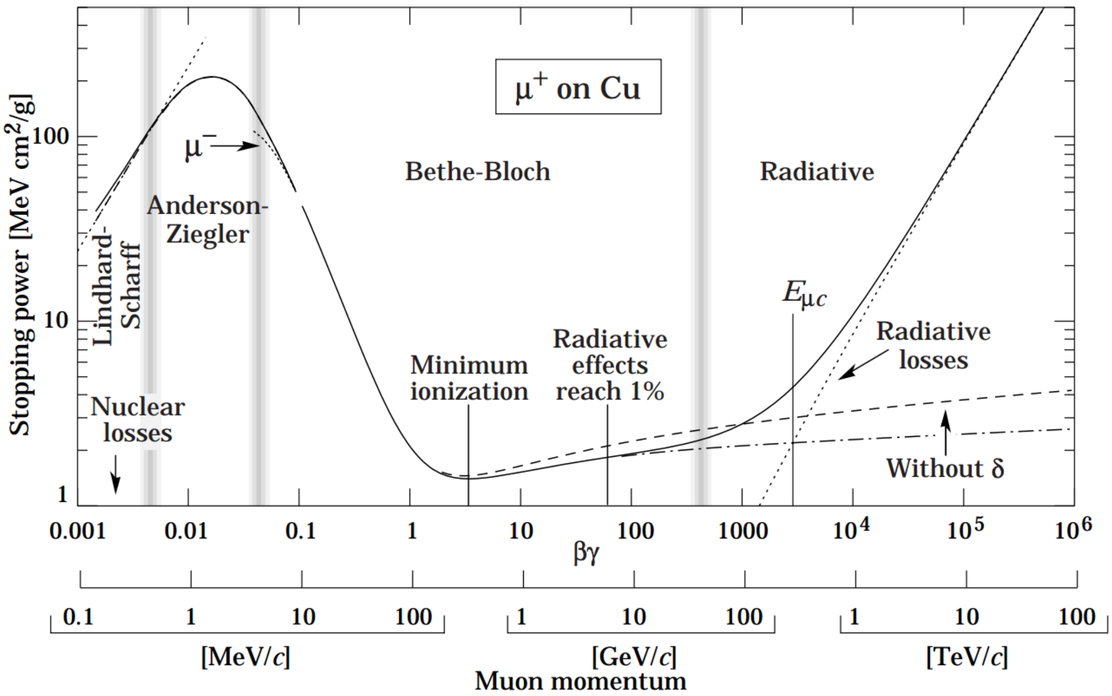

FIG. 5.3: Stopping power ($-dE/dx$) for positive muons in copper [2].

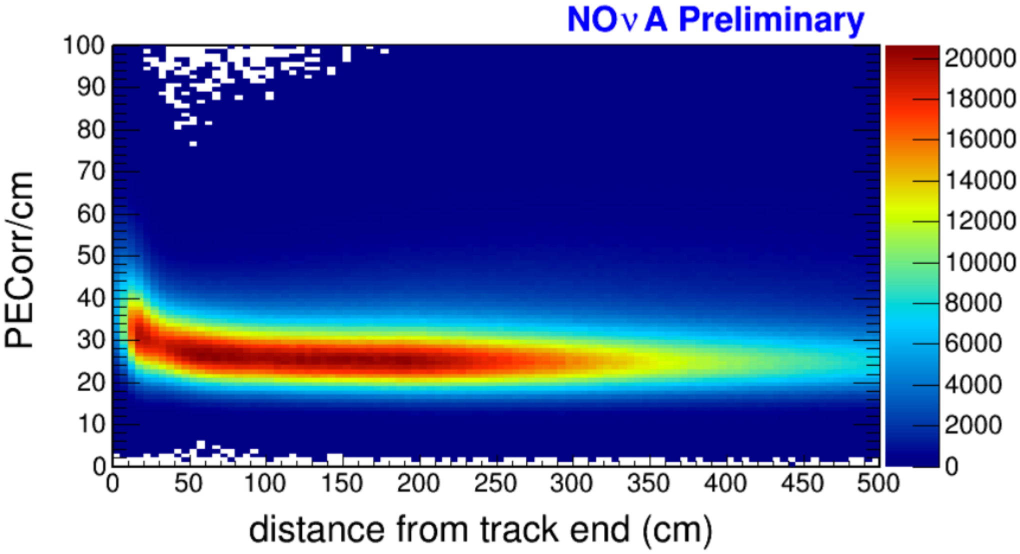

FIG. 5.4: Distribution for PECorr/cm vs. distance from the track end from Far detector cosmic-ray data. It is used to calculate the absolute energy calibration factor.

5.1.3 Timing Calibration

The timing calibration process in NOνA is performed to correct the timing offsets between the DCMs and determine the timing resolution using cosmic-ray data. The first purpose can be achieved by tracking the time of hits from a cosmic ray that passes through multiple DCMs. The timing resolution is determined empirically by through-going cosmic muons for the Far detector and by muons that are produced from neutrino interactions in the surrounding rock for the Near detector [84].

5.2 Reconstruction

The reconstruction process translates calibrated data into physically analyzable data including interaction energy, vertex location, and size. This is achieved by several sequential modules developed for different purposes. First, the the data is "sliced" [85] by small spatial and timing windows to group hits that belong to a single neutrino interaction. A slice will be used as the basic reconstruction unit in the later steps. Next, a two-point Hough Transform algorithm [20] is applied to each slice to identify geometric lines. These lines are later used by a Elastic Arms algorithm [86] to determine the neutrino interaction vertex in a slice. Lastly, the fuzzy K-mean algorithm [87] uses the vertex information as a seed to cluster cell hits into different prongs, each one of which corresponds to a particle produced in the interaction.

5.2.1 Slicer4D

The NOνA slicing algorithm Slicer4D [85] is based on the DBSCAN (Density-Based Spatial Clustering of Application with Noise) algorithm. It groups the hits that result from the same neutrino interaction by computing the four-dimensional distance (including time and space) between each pair of cell hits using the following equation:

$$\epsilon = \left(\frac{\Delta T - \frac{\Delta\vec{r}}{c}}{T_{res}}\right)^2 + \left(\frac{\Delta Z}{D_{pen}}\right)^2 + \left(\frac{\Delta XY}{D_{pen}}\right)^2 + \left(\frac{PE_{pen}}{PE}\right)^5 \tag{5.3}$$

In this equation, the first term calculates the timing difference where T_{res} is the timing resolution between the hits, summed in quadrature. While ΔZ (ΔXY) are the distances of the hits in Z (X/Y) direction, and $\Delta\vec{r}$ is the radial distance defined as $\Delta\vec{r} = \sqrt{\Delta Z^2 + \Delta XY^2}$ for hits in the same view while $\Delta\vec{r} = \Delta Z$ for hits in opposite views. The PE is the sum of the number of photoelectrons in the pair of hits added in quadrature. The parameters denoted with "*pen*" stands for the penalty terms that are designed to rule out the extreme cases.

For each individual hit, the distances from it to all other hits is computed using Equation 5.3. The ones that have distances less than a predefined threshold are tagged as neighbors of the target hit. After the tagging, hits that have more than four neighbor hits are called core hits, and others are called border hits. By clustering the core hits with all their neighbors iteratively, the slice object is constructed with the minimum requirement of three hits in each view to exclude coincident noise. Figure 5.5 shows a typical Far detector event display before and after the slicer4D is applied [85].

To optimize the parameters of the slicing algorithm, two criteria, completeness and purity, are chosen to evaluate the performance of the slicer. Completeness reveals the fraction of hits that truly come from an interaction that are clustered in a slice:

$$Completeness = \frac{E\left(hits\ clustered\ in\ slice\ and\ truly\ belong\ to\ the\ slice\right)}{E\left(hits\ truly\ from\ one\ interaction\right)} \tag{5.4}$$

While purity shows the fraction of hits in a slice that are truly from the desired interaction:

$$Purity = \frac{E\left(hits\ clustered\ in\ slice\ and\ truly\ belong\ to\ the\ slice\right)}{E\left(hits\ clustered\ in\ the\ slice\right)} \tag{5.5}$$

The slicer4D optimization is performed using cosmic-ray data in the FD and rock neutrino data in the ND. Figure 5.6 shows the distribution of completeness vs. purity of the optimized slicer4D in both detectors. On average, the slicer4D achieves 99.3% for both purity and completeness in FD, and 98.5% purity and 94.4% completeness in ND [85].

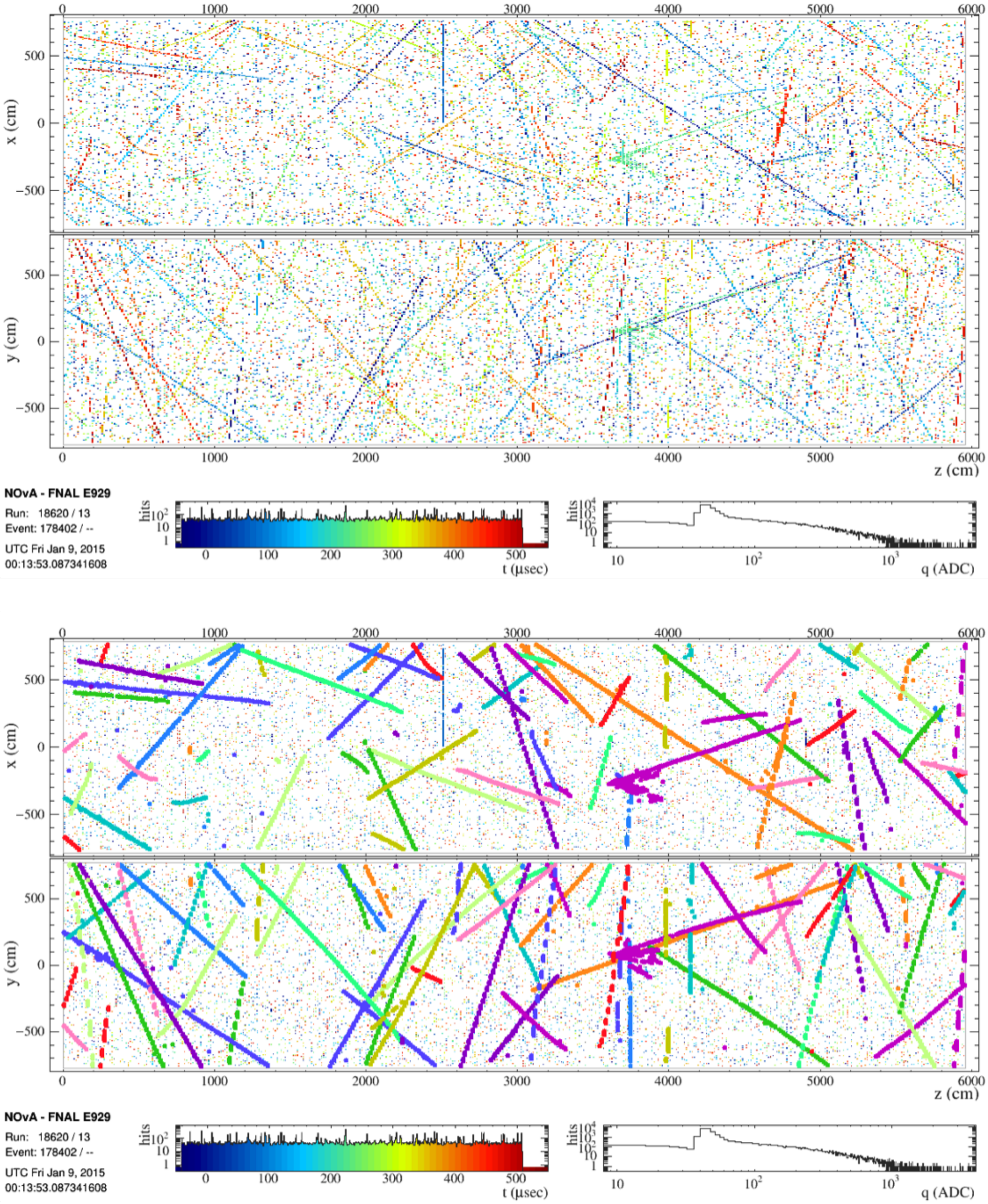

FIG. 5.5: Far detector simulation showing the event display with 550 μs readout window before (top plot) and after (bottom plot) slicer4D reconstruction. In each plot the top and bottom panel respectively represent the XZ and YZ views of the detector. Different colors indicate different timing of the hits. For the bottom plot after slicing, the bold lines shows the clusters of hits that the slicer constructed.

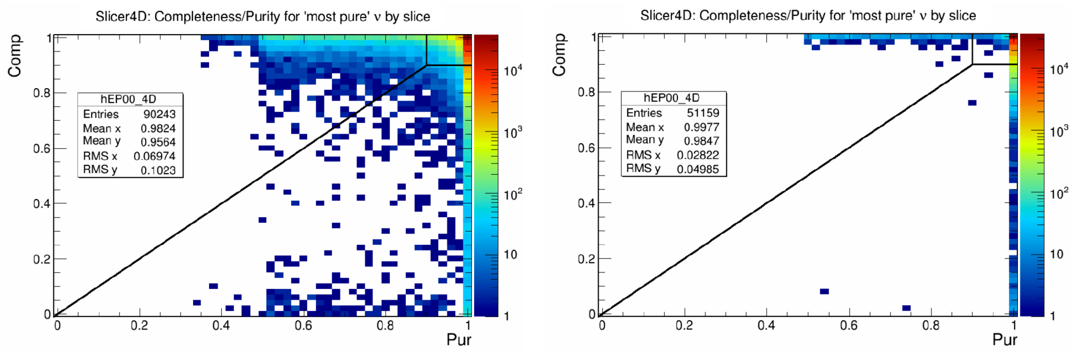

FIG. 5.6: 2D distribution of completeness vs. purity of the Slicer4D algorithm. For Near detector (left), the model is tuned on rock-interation neutrino data. While for Far detector (right), it is tuned on cosmic-ray data.

5.2.2 Hough Transform

After grouping the hits into a slice, the next step is to perform a two point Hough transform [20, 88] that constructs a set of two dimensional lines for each view of the detector to outline the geometric features of the interaction. To get a better handle on the vertical lines, the algorithm is parameterized by polar coordinates (ρ, θ) where ρ is the perpendicular distance from the target hit to the reconstructed line and θ is the angle between the line and the x-axis.

In each detector view (XZ or YZ), the Hough transform is applied to construct a line that passes through each pair of the hits in the slice and calculate its Gaussian smeared vote according to:

$$\begin{aligned} vote &= e^{-\frac{(\rho-\rho_0)^2}{2\sigma_\rho^2}} e^{-\frac{(\theta-\theta_0)^2}{2\sigma_\theta^2}} \\ \sigma_\rho &= \frac{3}{\sqrt{12}} \\ \sigma_\theta &= \frac{3}{d\sqrt{6}} \end{aligned} \tag{5.6}$$

where d is the distance between the two hits in the pair. The constructed lines are stored in a parameter space called a Hough map during this process. After iterating through all the possible hit pairs, peaks are formed in the Hough map and grouped into a line pattern, which represents a possible track of a particle. Some of the lines that fall below the cut-off criteria on length and number of combinations are discarded. A Gaussian smoothing weight is applied in order to improve the accuracy of the lines. Next a refined line finding process is performed over a 7×7 grid of bins around the peak bin for better estimation of the line. Hits that fall within one cell depth (6 cm) in the last round are exempt from the refining iteration. This refining iteration is repeated until no more peaks are formed or a predefined maximum number of lines is reached. Figure 5.7 and 5.8 show one example of the first two iterations of this process [20].

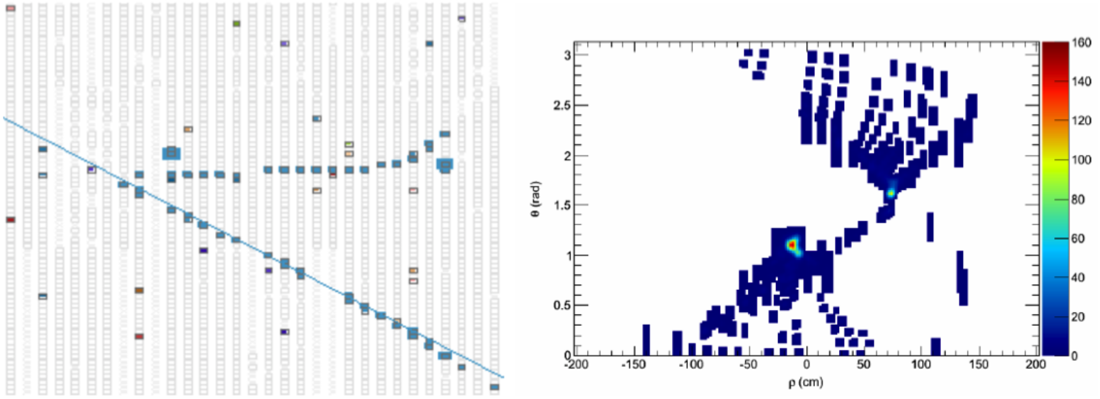

FIG. 5.7: The first iteration of the Hough transform shows in the event display (left) and the corresponding Hough map (right). Two peaks are clearly formed in the map [20].

Two main criteria are used to evaluate the performance of the Hough transform process. The first one is the perpendicular distance from the Hough lines to the true Monte Carlo interaction vertex, which demonstrates the correctness of the ρ direction recon-

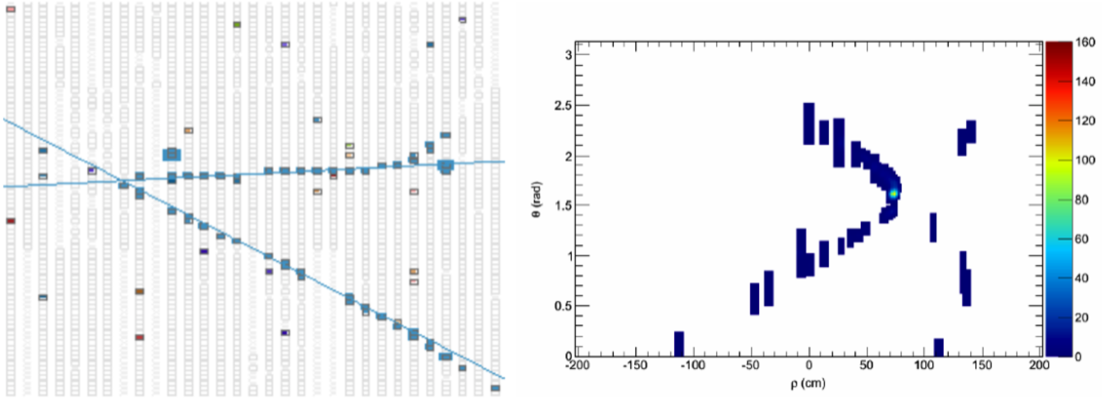

FIG. 5.8: The second iteration of the hough reconstruction after removing the hits associated with the first iteration in which the noise is drastically reduced [20].

struction. The second one is the dot product between the trajectory of the Hough lines and the matching truth interaction, which demonstrates the correctness of the θ direction reconstruction. Figure 5.9 shows the performance evaluation using NOνA Far detector simulation.

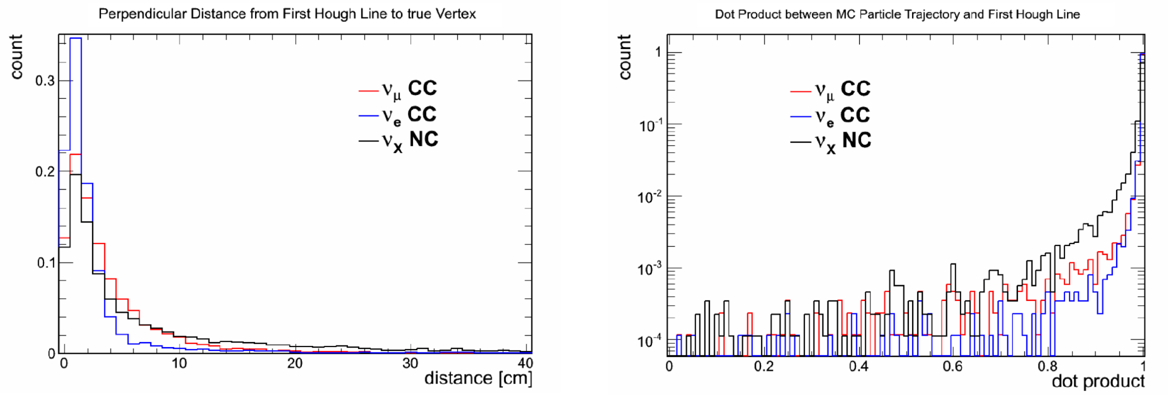

FIG. 5.9: Left: the perpendicular distance from the first Hough line to the true vertex with an average 4 cm for $\nu_\mu CC$, 2.7 cm for $\nu_e CC$ and 6.7 cm for NC. Right: Dot Product with the first Hough line and the best matched MC particle trajectory [20].

5.2.3 Elastic Arm Vertex Finding

Using the geometric lines reconstructed by the Hough transformation, the vertex of the neutrino interaction in a slice can be determined by the Elastic Arm algorithm [86]. In the NOνA detector, it is reasonable to assume based on the event topology that all the activity including prongs or "arms" originate from a single vertex where the interaction happened. Thus the coordinates of an arm can be described as following:

$$\begin{aligned} x(s) &= x_0 + s \cdot \sin\theta_\alpha \cos\phi_\alpha \\ y(s) &= y_0 + s \cdot \sin\theta_\alpha \sin\phi_\alpha \\ z(s) &= z_0 + s \cdot \cos\theta_\alpha \end{aligned} \tag{5.7}$$

where (x_0, y_0, z_0) is the location of the vertex, s is the distance, ϕ_α and θ_α are the azimuth and zenith angle, respectively. To find the optimal vertex for one slice, the algorithm looks for the value of the parameters that minimize the energy cost-function:

$$E = \sum_{i=1}^{N}\sum_{a=1}^{M} V_{ia}M_{ia} + \lambda \sum_{i=1}^{N}\left(\sum_{a=1}^{M} V_{ia} - 1\right)^2 + \frac{2}{\lambda_\nu}\sum_{a=1}^{M} D_a \tag{5.8}$$

in which M_{ia} is the perpendicular distance from target hit i to arm a, V_{ia} is the strength of the association between hit i and a, and D_a is a distance measurement from the vertex to the first hit in arm a [86]. In Equation 5.8, the first term measures the goodness of the fit between N hits and M arms in the slice. The second term is to penalize the hits that are not associated with any arm. The third term is specially designed for NOνA, in which the vertex location is not constrained in advance, as a penalty to arms whose first hit is further away from the vertex than parameter λ_ν. While λ and λ_ν serve as knobs of the cost function to control the strength of the penalty term, and λ_ν is chosen to be the photon radiation length $7/9X_0$.

The hit-track distance M_{ia} is computed in each view by:

$$M_{ia} = \left(\frac{d_{ia}^{prep}}{\sigma_i} \right)^2 \tag{5.9}$$

where d_{ia}^{prep} is the perpendicular hit-track distance in the view, and σ_i is the spatial resolution of the detector that defined as the half cell depth ($\sigma_i = 3/\sqrt{12}\ cm$). In the special cases when the hits are in the backward direction relative to the first hit of the arm, the distance calculation is modified by using the hit-to-vertex distance d_{ia}^{vtx} instead:

$$M_{ia} = \begin{cases} \left(\frac{d_{ia}^{vtx}}{\sigma_i} \right)^2 & if\ \frac{d_{ia}^{vox}}{\sigma_i} \leq 1 \\ \left(\frac{d_{ia}^{vox}}{\sigma_i} \right)^4 & if\ \frac{d_{ia}^{vox}}{\sigma_i} > 1 \end{cases} . \tag{5.10}$$

The other term V_{ia} that measures the hit-track association likelihood is calculated by:

$$V_{ia} = \frac{e^{-\beta M_{ia}}}{e^{-\beta\lambda} + \sum_{b=1}^{M} e^{-\beta M_{ib}}} \tag{5.11}$$

with the normalization to ensure the total likelihood $\sum_{a=1}^{M} V_{ia}$ is bound between 0 and 1. Here the parameter β is inversely proportional to the temperature T thus represents the range of influence of the association. In summary, by minimizing the energy function 5.8, we can find the best fit parameter set $(x_0, y_0, z_0, \vec{\theta}, \vec{\phi})$ which stands for the reconstructed location of the interaction vertex.

5.2.4 Fuzzy K-Means Algorithm

After determining the vertex position, the Fuzzy k-means reconstruction [87] is applied to group hits into separate prongs that belong to different particles coming from the vertex. It allows each hit to belong to more than one cluster, thus the boundaries of the cluster are fuzzy. This possibilistic feature also allows us to isolate noise hits easily since they will have no membership with the reconstructed prongs. The Fuzzy-K algorithm starts with solving a 2D problem by processing the two detector views (XZ and YZ) separately, then merges them into 3D prongs later.

To cluster the hits into 2D prongs, FuzzyK first calculates the angle for each hit with respect to the z axis, and a corresponding angular uncertainty σ which depends on the distance d from the vertex to the hit and is given by [87]:

$$\sigma = \frac{1.745}{d} + 0.0204 + 0.000173 * d. \tag{5.12}$$

Then an angle density matrix w, which is divided into 360 bins, is calculated to find the angle θ with the highest cell density with:

$$w_k = \sum_{j=1}^{n} e^{-\left(\frac{\theta_k - \theta_j}{\sigma_j}\right)^2}$$
$$\theta_k = -\pi + \frac{k * \pi}{180} \tag{5.13}$$

in which k is the bin number that varies from 0 to 359.

To determine the membership of the hits to clusters, an iterative two-step process is used. First the angular distance between the hits j and the center of the cluster i is computed by:

$$d_{ij} = \left(\frac{\theta_j - \theta_i}{\sigma_j}\right)^2, \qquad -\pi \leq (\theta_j - \theta_i) \leq \pi \tag{5.14}$$

and then the degree of membership is calculated by:

$$\mu_{ij} = e^{-\frac{m\sqrt{a}d_{ij}}{\beta}} \tag{5.15}$$

where a is the number of clusters in the slice; m and β are the predefined control parameters with m representing the fuzziness of the cluster which is set to be 2, and β as a normalization factor that measures the degree of spread of the hits and set to be 4. The second step uses the following equation to update the central angle of the clusters:

$$\theta_i' = \theta_i + \frac{\sum_j^n \frac{\mu_{ij}}{\sigma_j^2} (\theta_j - \theta_i)}{\sum_j^n \frac{\mu_{ij}}{\sigma_j^2}}. \tag{5.16}$$

This iteration is executed until $|\theta_i' - \theta_i|$ falls below a predefined tolerance value for all cluster centers.

Lastly, the 2D clusters reconstructed in each view need to be matched into 3D prongs. This is performed by calculating the two cumulative cell hit energy functions, which depend on the distance along each track, for each possible pairs of clusters from different views. For the true matching pairs, the energy profile should be quite similar between the two views. A Kupier metric is used here to determine the best matching pairs iteratively until all possible clusters have been matched as shown in Figure 5.10 [87, 89].

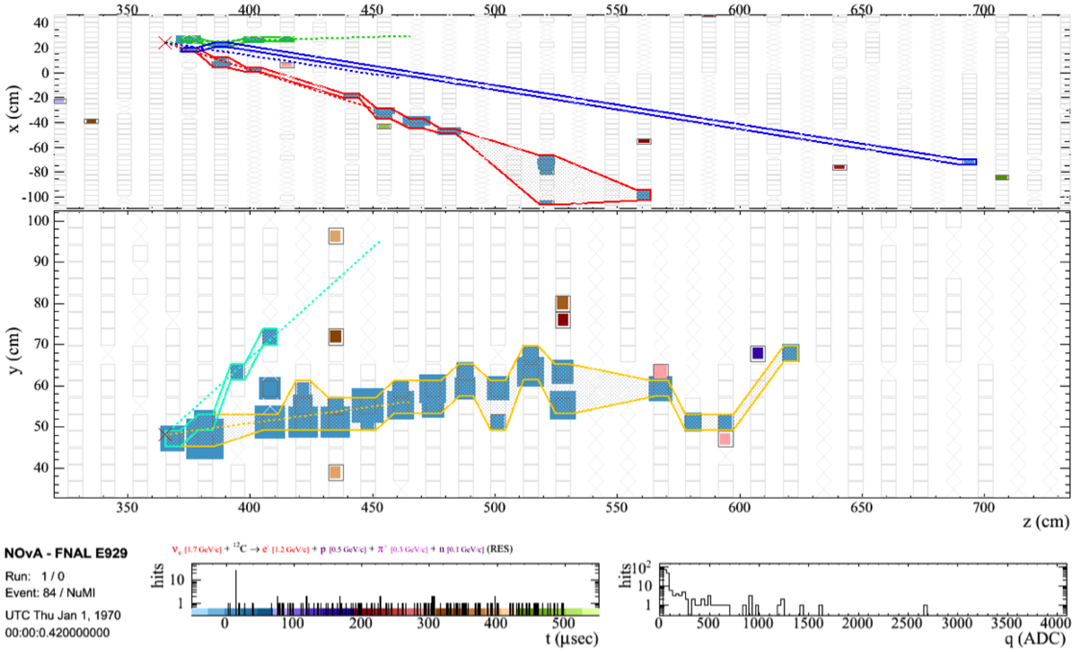

FIG. 5.10: Event display of a typical ν_e CC event with a electron shower. The outlines show the FuzzyK reconstructed prongs.

CHAPTER 6

ν_e Event Selection

In the ν_e appearance analysis, we intend to select the ν_e CC events that oscillated from the $\nu_\mu$beam as signal, and reject NC, ν_μ CC, beam contained ν_e CC and cosmic events as backgrounds. To serve this purpose, there are several levels of cuts that are applied to select a sample of events. The first level is data quality selection, followed by preselection cuts. Finally, one of two cuts based on our particle identifiers is applied to select a final set of electron-like events for the analysis. More details of the selection will be listed in the following sections.

The specific value of every cut at each level was tuned by the optimization of the figure of merit (FoM) defined as:

$$FOM = \frac{s}{\sqrt{b}} \tag{6.1}$$

where s and b are the number of selected signal and background events, including cosmic events in the background. An alternative FOM where the denominator is replaced by $\sqrt{s+b}$ is considered, which improves the signal efficiency but only marginally improves the sensitivity to the mass ordering. In the analysis in this thesis, Equation 6.1 works better for the discovery of ν_e appearance. The cuts will be retuned using the second formula in a future analysis when the goal is a precision measurement.

6.1 NOνA Event Topologies

There are three types of neutrino events that we try to identify in the NOνA detectors: ν_μ charged current (ν_μ CC), ν_e charged current (ν_e CC) and neutral current (NC). Figure 6.1 shows the event topology of these three types of interactions. The ν_e CC events, which are the signal for the ν_e appearance analysis, produce an electromagnetic shower. The ν_μ CC and NC events are the primary backgrounds for this analysis. While ν_μ CC events are easier to identify based on its signature of a long and narrow muon track produced in the interactions. NC events with a single π^0 have quite a similar event topology to the signal and are the major background source for the ν_e appearance analysis.

6.2 Data Quality Selection

The first step of the selection is data quality selection. This selection applies the cuts on a spill-by-spill basis to ensure that the beam conditions are good, the detector is

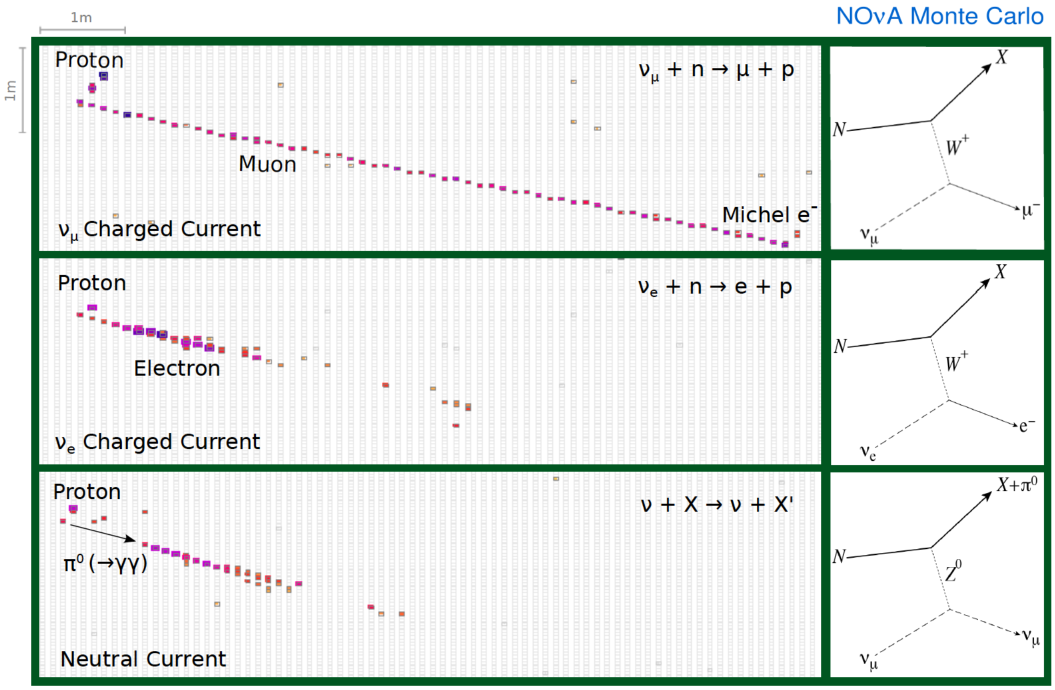
1m
1m
NOvA Monte Carlo
Proton
νμ + n → μ + p
Muon
Michel e⁻
νμ Charged Current
N
X
W⁺
νμ
μ⁻
Proton
νe + n → e + p
Electron
νe Charged Current
N
X
W⁺
νe
e⁻
Proton
ν + X → ν + X'
π⁰ (→γγ)
Neutral Current
N
X+π⁰
Z⁰
νμ
νμ

FIG. 6.1: Event topology for the three basic event types: ν_μ CC (top), ν_e CC (middle) and NC(bottom) from the NOνA simulation.

functioning well, and the reconstruction is performed properly. It can be further divided into two set of selections: Beam quality selection and Subrun data quality selection.

6.2.1 Beam Quality

Beam quality cuts are applied on a spill by spill basis to monitor the conditions of the NuMI beam and to determine if the beam is of sufficient quality for the spill to be used in the NOvA analysis. The main characteristics of the NuMI beam that we use to perform these cuts include: the protons on target (POT) as measured by magnetic induction in toriods, the horn current, the position of the beam on the target, the spread of the beam, and the time difference between the event time recorded in the NOνA event files and the spill time recorded in the Intensity Frontier Database (IFDB). For the first analysis datasets, these beam quality cuts remove less than 1% of the POT. Here are the list of cuts that we applied to both of the detectors' spills:

- The current event time must be less than 0.5 s from the time of the nearest beam spill in the IFDB,
- The POT in the spill must exceed 2×10^{12},
- The horn current must be between -202 kA and -198 kA,
- The beam x and y positions must be between 0.02 mm and 2.00 mm,
- The beam x and y widths must be between 0.57 mm and 1.58 mm.

6.2.2 Subrun Data Quality

In NOνA, data taken from the detectors is recorded as runs and subruns. For the Far detector, each subrun is about 2-3 minutes of data taking, and each run contains 64 subruns. While in the Near detector, each subrun lasts an hour and each run contains 24 subruns. A number of metrics, which are different between the two detectors, are checked to eliminate bad data.

Far Detector

The good subrun selection for the Far detector has following requirements [90]:

- Subrun sanity check: To check the rationality of the file,

  - Subrun start time < subrun end time,
  - Year ≥ 2013,
  - Data file is not empty.

- Median MIP hit rate: To check the rate of physics hits is consistent throughout the detector, which indicates it is running at nominal gain
  - $13\,\mathrm{Hz} <$ Median MIP Hit Rate $< 23\,\mathrm{Hz}$.

- Detector size: To check the detector has a large enough working and active region for the analysis
  - Number of functioning consecutive diblocks ≥ 4 (detector construction occured during data taking).

- Reconstruction quality:
  - Fraction of reconstructed tracks per event that are 2D $< 15\%$,
  - $1.2 <$ Slices/Trigger/10^4 Channels < 3.2.

Near Detector

The subrun good data selection in the Near detector is similar to the Far detector, except in the Near detector we use only NuMI triggers to make the selection.

- Subrun duration check:
  - Number of NuMI triggers > 1000.

- Median MIP hit rate:
  - $13\,\mathrm{Hz} <$ Median MIP Hit Rate $< 23\,\mathrm{Hz}$.
- Detector size:
  - Number of functioning consecutive diblocks ≥ 4 (all Near detector diblocks).
- Empty spills:
  - Fraction of empty (no POT) spills $< 3\%$.
- Timing peak: To check the detector is properly synchronized to the beam
  - $217\,\mu s <$ timing peak start $< 219\,\mu s$,
  - $227\,\mu s <$ timing peak end $< 229\,\mu s$.
- Slice Rate:
  - $3.5 <$ number of slices per spill (2.5×10^{13} POT equivalent) < 5.5.

6.3 ν_e Event Selection

This suite of cuts are applied to each slice of the data files that pass the data quality selection but prior to the particle identification selection for three main purposes: first, to further ensure that the neutrino event is well contained and well reconstructed; second, to eliminate rock muon events and reject the majority of the FD cosmic rays; third, to slim down the size of the data that will be processed through the following particle identification selection to save production time and disk usage.

6.3.1 Reconstruction Quality Cuts

Reconstruction quality cuts [91] are designed, as the name suggests, to remove reconstruction failures and guarantee the slice is well reconstructed by requiring:

- Number of hits per plane: Remove FEB flash issues in data that happen when a high energy deposit in one cell affects neighbor pixels in the APD, some microseconds later. This causes multiple fake hits in the same plane after the initial energy deposition.
    - $\frac{nHit}{nPlane} < 8$.
- Number of hits in slice: Remove neutrino events that do not have enough activity in one or both views.
    - Vertical view: $nHit_X > 5$,
    - Horizontal view: $nHit_Y > 5$.
- Shower hit asymmetry: Remove events with a high discrepancy in hits between the two views.
    - $|nHit_x - nHit_y|/(nHit_x + nHit_y) < 0.4$.
- Angle between the two leading showers: Remove events that have one of the most energetic prongs going backward, likely due to reconstruction failure.

  - $\cos\theta > -0.95$.

- Gap between the leading shower and the interaction vertex:
  - $Gap < 100\ cm$.
- Shower reconstruction fraction: Select only the events that have more than 70% of the hits reconstructed into a shower, to make sure the noise hit rate is low.
  - $nHitFrac > 0.7$.

6.3.2 Containment Cuts

This set of cuts is designed to select events that are well contained within the detectors and makes sure there is sufficient information for reconstruction. It also helps to remove the environmental background, such as the neutrino interactions that happen in the surrounding rock for Near detector (rock events), and cosmic-ray in the FD.

For the Far detector, since part of the first analysis data was taken while the detector was under construction, the detector diblock configurations varied depending on the construction status. Thus the boundaries of the active detector are dynamic and stored during the data taking in each subrun. The containment cuts are defined based on the distance between the start/stop point of the shower and the live edges of the detector. Since the overburden built around FD to reduce the cosmic ray contamination is asymmetric, the cut values are different for the different walls and optimized for FOM:

- East wall: $Dist_{min} > 15\ cm$,

- West wall: $Dist_{min} > 10\ cm$,
- Top wall: $Dist_{min} > 150\ cm$,
- Bottom wall: $Dist_{min} > 10\ cm$,
- Front wall: $Dist_{min} > 35\ cm$,
- Back wall: $Dist_{min} > 200\ cm$.

The containment cuts for the Near detector is more straightforward since the active detector region stays the same for all the subruns. As shown in Figure 6.2, the cuts select only the neutrino event that starts and stops inside the box with the green line, and the interaction vertex must lies within a tighter box region marked with red line. The specific cuts used for Near detector data are:

- 3D shower start and stop position
    - $-180\ cm < x, y < 180\ cm$,
    - $25\ cm < z < 1225\ cm$.
- ElasticArms Vertex (Figure 6.3)
    - $-140\ cm < x, y < 140\ cm$,
    - $100\ cm < z < 700\ cm$.
- Front planes: To reject rock muon events
    - No fewer than 6 planes before the most upstream hit in the slice.

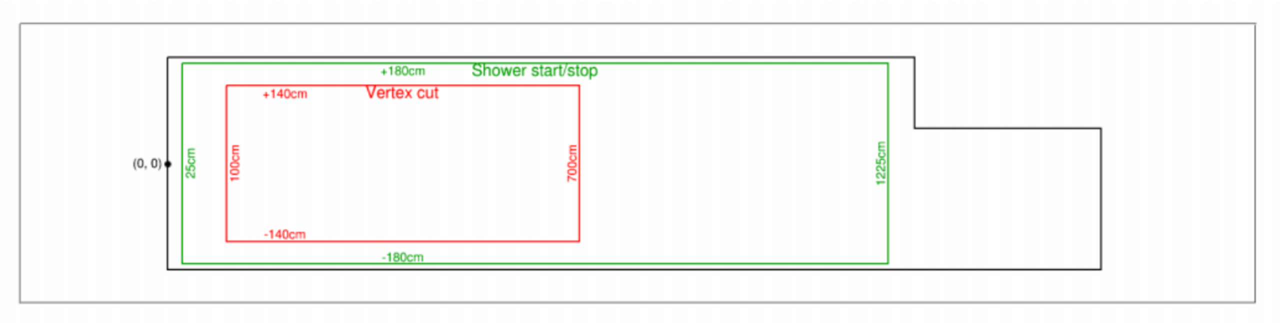
+180cm
Shower start/stop
+140cm
Vertex cut
(0, 0)
25cm
100cm
700cm
1225cm
-140cm
-180cm

FIG. 6.2: The position of the Near detector containment cuts. The selection requires the interaction vertex must be within the red box and the start and stop points of all showers must be within the green box. The origin of the coordinates is in the center of the upstream face of the detector and the beam travels from left to right in the positive z direction. Positive y is upwards, and positive x is into the page (West).

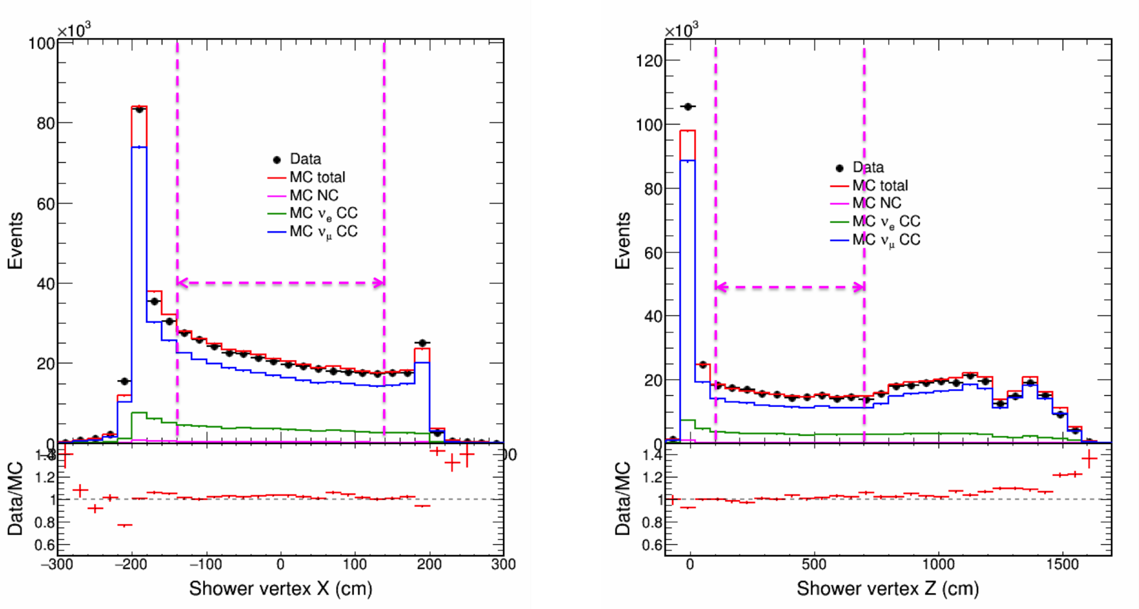

FIG. 6.3: Distributions of the ElasticArms vertex X (left) and Z (right) for ND data and MC (decomposed into different background event type). Magenta Lines are containmnet cut position.

6.3.3 Cosmic Ray Rejection for Far Detector

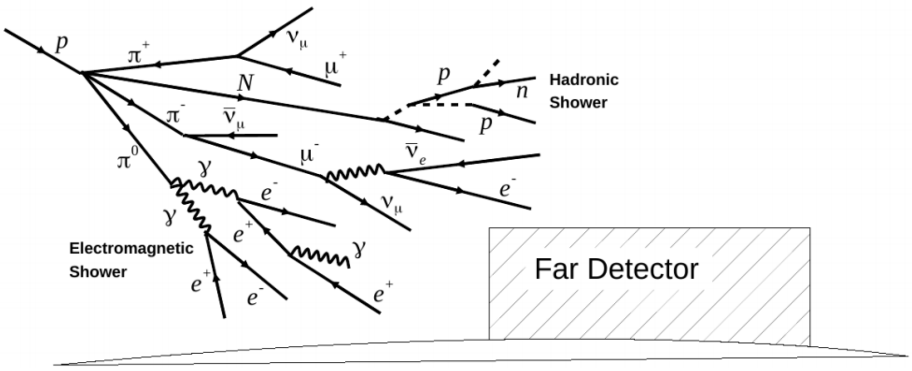

FIG. 6.4: Primary cosmic rays interact with air molecules, producing secondary cosmic rays.

The NOνA Far detector, unlike the Near detector that sits 100 m deep underground, is located on the surface and exposed to abundant cosmic rays that originate from astrophysical processes (Figure 6.4). These cosmic rays are a dominant source of the background for the ν_e analysis. Thus cosmic background rejection is crucial for the ν_e event selection. In addition to the containment cuts, a cut on the fraction of event transverse momentum (p_{trans}/p) with respect to the beam direction is also made to further enhance the signal to cosmic background ratio. This cut is based on the fact that cosmic rays tend to enter the detector from its top and yield a higher fraction of the transverse momentum, while the beam neutrino tend to traverse the detector in horizontal direction with lower p_{trans}/p value (Figure 6.5) [91].

- Fraction of transverse momentum (p_{trans}/p)
  - When the interaction occurs close to the top wall ($DistToTop_min < 25\ cm$), $p_{trans}/p \leq 0.4$,

- Other cases ($DistToTop_min \geq 25\ cm$), $p_{trans}/p \leq 0.65$.

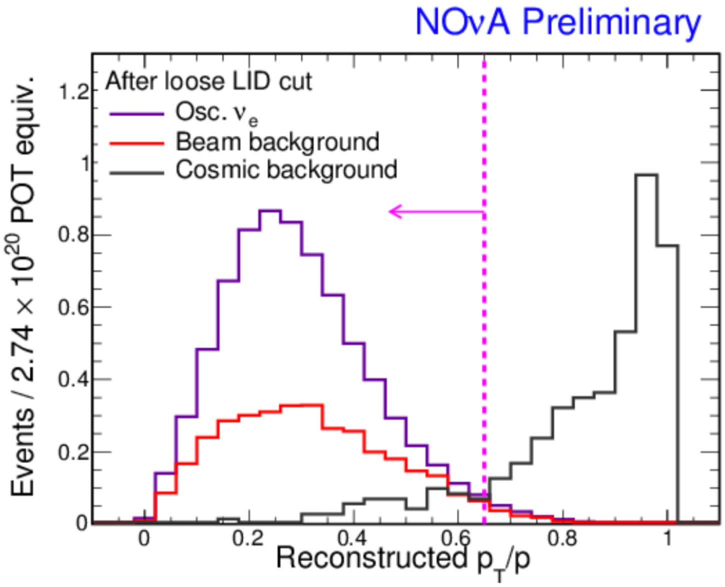

FIG. 6.5: Distribution of the transverse momentum fraction for signal, beam background and cosmic background. Cosmic rays tend to show large p_t/p value, while signal peaks at low values. This plot has all other preselection cuts and a loose LID cut of > 0.7 applied (described in Section 6.4).

6.3.4 Preselection Cuts

The preselection for the ν_e analysis depends on three energy-related variables: the total number of hits in the slice, total calorimetric energy (GeV), and length of the primary FuzzyK prong. They are optimized to remove the energy region that contains mostly background events (ν_μCC and NC interactions), and events passing the preselection are feed to the particle identification algorithms for the final signal selection. The preselection cuts are:

- Slice hits:

  - Far detector: $40 < nHits < 115$,
  - Near detector: $20 < nHits < 200$ (Figure 6.6).

- Calorimetric energy:
  - Far detector: $1.5\,\mathrm{GeV} < calorimetric\ energy < 2.7\,\mathrm{GeV}$,
  - Near detector: Extrapolate full energy spectrum to FD, then apply the same energy cut as FD (Figure 6.7).

- Shower length:
  - $140\ cm < length\ of\ primary\ FuzzyK\ prong < 500\ cm$.

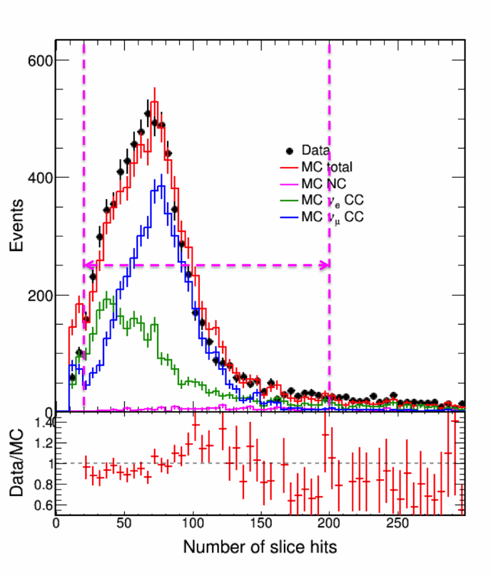

FIG. 6.6: ND number of hits per plane for data (black) and MC (red) after all ν_e preselection cuts except the nHits cut.

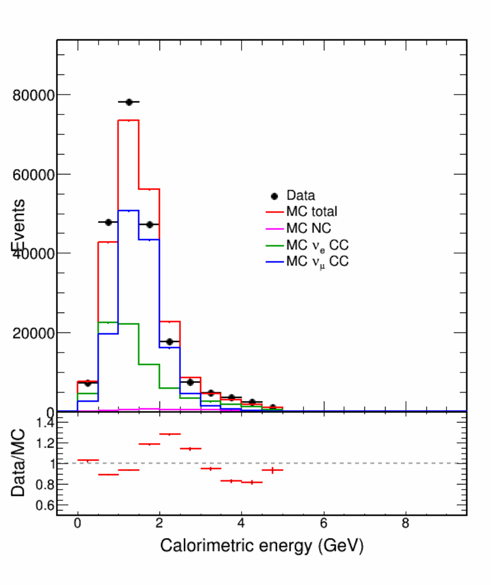

FIG. 6.7: ND calorimetric energy distribution for data (black) and MC (red) after ν_e preselection.

6.4 ν_e Particle Identification

The previous two sections describe the simple cuts that can remove a large component of the background without sacrificing many signal events. To further purify the selected sample and eliminate the residual backgrounds, more sophisticated Particle Identification algorithms are invented and built. In the ν_e analysis, we developed two distinct PID algorithms, named LID and LEM, to serve this purpose.

The LID [92] is a likelihood-based selector and focuses on the energy deposition per unit length (dE/dx) along the particle's trajectory for different type of particles. It utilizes the event vertex and prongs made by the Fuzzy-K reconstruction. LID reclusters these prongs to conform to the shape expected of an electron shower, and performs a cell-energy deconvolution to prevent double-counting of a cell's energy in the event energy. This information is extracted from both longitudinal (along the direction of the leading shower) and transverse (perpendicular) energy deposition of the most energetic shower, and is tested against template histograms for various particles hypothese (e, μ, p, n, $\pi^{\pm}$, and γ). The likelihood differences along with other topological variables, such as the shower energy fraction, the mass of possible π^0s, the vertex energy, the gap between the start point of the shower to the vertex, and $\cos\theta$ (θ is the angle of the leading shower with respect to the beam direction) are fed into a feed-forward artificial neural network (ANN). An ANN is a computational network that consists of one input layer, one output layer and several hidden layers in between. By training it with large numbers of MC events for which the type of the event is known, ANN performs the calculation and constructs the

LID classifier (Figure 6.8).

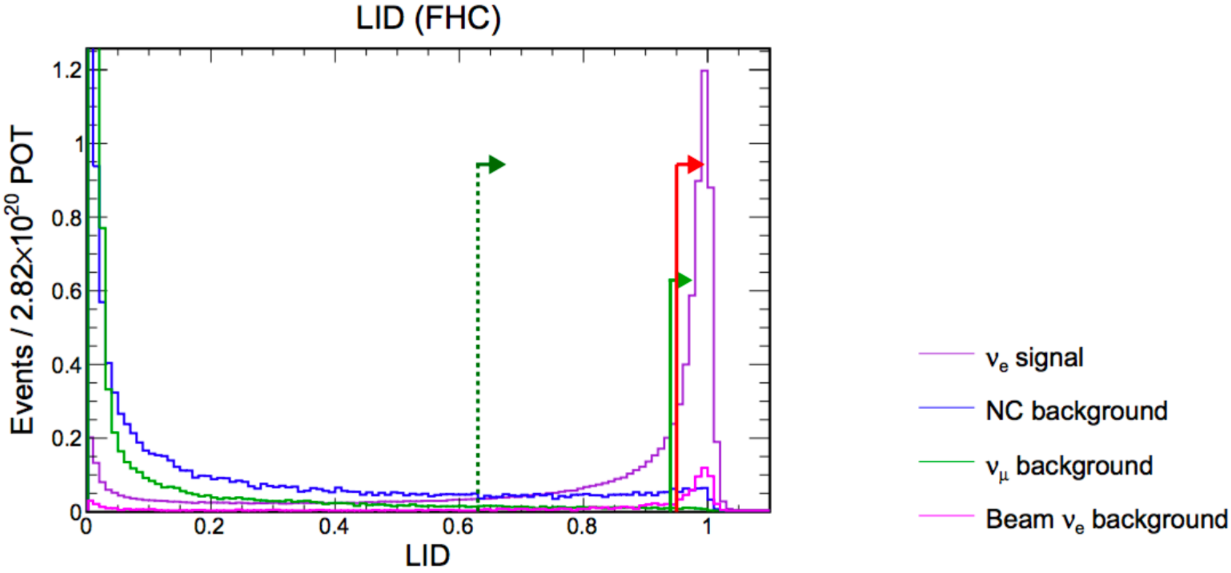

FIG. 6.8: Simulated LID distribution (scaled to effective full detector exposure of 1.8×10^{20} POT) in Far detector after all preselection cuts for ν_e signal and backgrounds. The two green lines shows the selection that optimize $s/\sqrt{b}$ (solid) and $s/\sqrt{s+b}$ (dashed), while the red line is the cut value used in the first analysis.

The other selection method, Library Event Matching (LEM) [93], uses a quite different technique but achieves similar performance as LID, with different systematic uncertainties. LEM compares the input event to a large number of simulated library events that include both signal and background interactions. By performing a cell by cell comparison of its events properties, LEM finds the most likely library events with a matching metric. This philosophy is inherited from the MINOS experiment, but has been specially re-designed to take advantage of the higher spatial resolution of the NOνA detectors. LEM uses an ensemble decision tree to generate the final result type of input event by feeding it 6 input variables including weighted fraction of signal in the best matched library events, the mean hadronic y, mean matched charge fraction with the best matches, energy differences with the best matches, the fraction of π^0s in the best matches, and the total calorimetric energy.

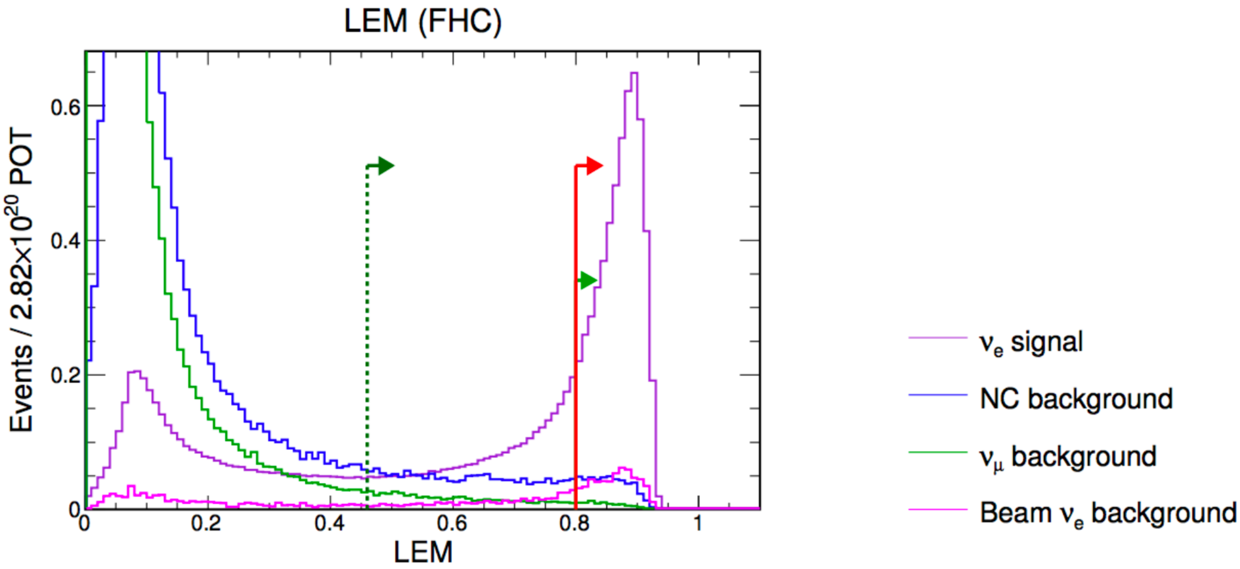

FIG. 6.9: Simulated LEM distribution (scaled to effective full detector exposure of 1.8×10^{20} POT) in Far detector after all preselection cuts for ν_e signal and backgrounds. The two green lines shows the selection that optimize $s/\sqrt{b}$ (solid) and $s/\sqrt{s+b}$ (dashed), while the red line is the cut value used in the first analysis.

The cuts on PID value for both selectors have been optimized for the first ν_e analysis of NOνA by requiring a minimum output value 0.95 for LID (red line in Figure 6.8), and 0.8 for LEM (red line in Figure 6.9). Both ν_e selectors achieve similar signal efficiency and background rejection for simulated events. The resulting LID selector has a signal efficiency of 34% with respect to the events selected by the containment criteria and purity of 84% for beam backgrounds in the Far detector, while the efficiency and purity for LEM selector is 35% and 83%, accordingly. For background rejection, both of them achieve better than 99% for beam background rejection, and better than 1 in 10^8 for cosmic induced background rejection. Before the FD beam data inspection, and after evaluating their sensitivity to ν_e appearance and vulnerability to systematic errors, the LID classifier was designated to be the primary selection algorithm by the ν_e group, while LEM the secondary selector.

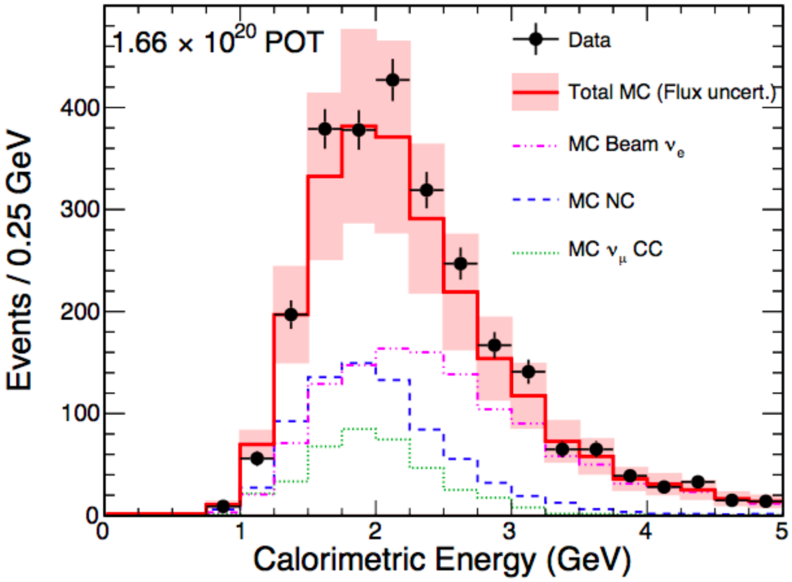

FIG. 6.10: ND calorimetric energy distribution for ND data and MC after ν_e preselection and LID cut (decomposed into different background event types). The error bar represents flux uncertainty, which largely cancels when extrapolated to the FD.

CHAPTER 7

ν_e Appearance Analysis

This chapter presents the first ν_e appearance analysis of NOνA. First, the description of the dataset used by this analysis is presented in Section 7.1, and data vs. MC comparisons are shown in Section 7.2. Section 7.3 discusses the decomposition process, which separates the different neutrino interaction types (ν_eCC, ν_μCC and NC) in the Near detector data for detector background estimation. Finally the background events selected in the Near detector are extrapolated to the Far detector (Section 7.4) to significantly reduce the systematic uncertainties of the final result.

7.1 First Measurement Data

The first measurement data, used in this thesis, were collected between February 6^{th}, 2014 and May 15^{th}, 2015. The collected data is divided into three periods. The first period went from February 2014 until the scheduled NuMI beam shutdown for maintenance and upgrade on September 5^{th}. The second period began after the beam came back on October 24^{th}, 2014 to March 14^{th}, 2015. Lastly, a top-off period lasting until May 15^{th}, 2015 was used for better statistics.

During most of the data taking period (until November, 2014), the Far detector was under construction. The effective fiducial mass varied from 2.3 kt for 4.0 kt of total mass to 10 kt for the full 14 kt. Because of the segmented design of the NOνA detector, once new diblocks were fully constructed and tested, they could be added to the DAQ stream without interrupting data taking. Figure 7.1 shows consecutive active diblocks of the FD in terms of exposure throughout the data-taking period. These different configurations of diblocks are also simulated in MC proportionally to data, as shown in Figure 7.2, to make the MC as close to the real conditions as possible. In total the accumulated exposure of FD for the first measurement is 3.45×10^{20} POT (Protons On Target), which is equivalent to 2.74×10^{20} POT collected in the full 14 kt detector [94].

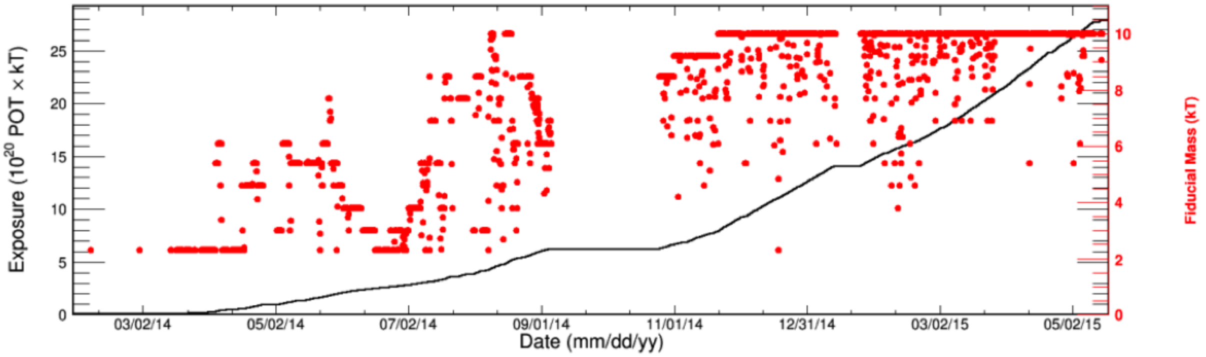

FIG. 7.1: The NOνA Far detector cumulative POT exposure (black line) and fiducial mass (red dots) for the first analysis period from February 6th, 2014 to May 15th, 2015. The blank region corresponds to the NuMI shutdown period.

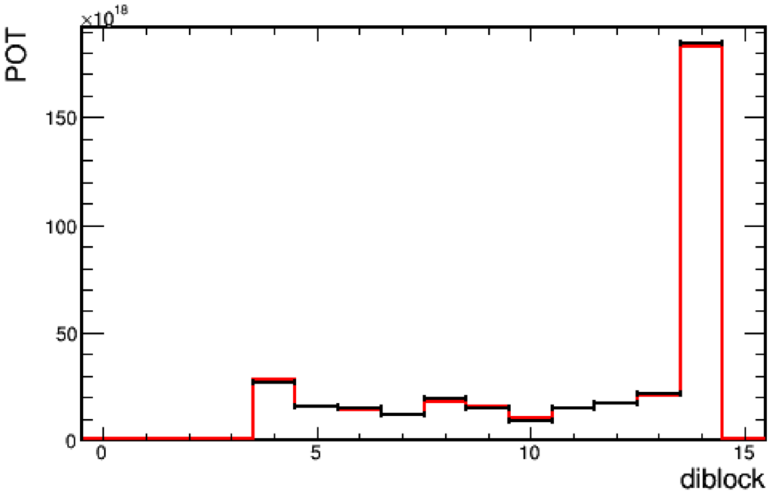

FIG. 7.2: POT exposure for different configurations of active diblocks in data (black) and MC (red). Here MC is area normalized to data.

The Near detector data is used to benchmark the simulation and make predictions of the numbers of beam backgrounds and signal events expected in the Far detector. The first analysis Near detector data, unlike the Far detector, was taken by the full detector because of its much smaller size. The total exposure of Near detector data is 1.66×10^{20} POT.

7.2 Data vs. MC Comparisons

The technical details of the NOνA simulation has already been described in Chapter 4. For each detector, a set of Monte Carlo simulated data was produced with customized run by run bad channel masks matched with real data. The masks are configured to ensure the active region in MC is continuously consistent with the detector state throughout the construction period. We produce many more MC events compared to the data exposure for each detector. We produced 9.92×10^{20} POT in ND, roughly 6 times the data, and 8.6×10^{23} in FD, roughly 2400 times the data.

7.2.1 ND Data vs. MC Comparison

Having the $\nu_e CC$ selection cuts defined in Chapter 6, we can now compare the data and simulation. The accumulated distributions are normalized to the ND data exposure (1.66×10^{20} POT). Table 7.1 displays the event counts and selection efficiencies after each cut level for both MC and data. These comparisons help us better understand our simulation models and analysis tools as well as display any possible issues. Figure 7.2a-7.7b are some key distributions after the data quality cuts that we used to make the ν_eCC selection listed in Table 7.1. Most of them have pretty good agreement between data and MC, especially in the selected region. The distribution of the calorimetric energy in Figure 7.2b does show some discrepancy in high energy region. This is caused by the mis-simulated scintillator saturation in MC and it is cut out by the energy cut after extrapolation to FD. To further investigate the disagreement, we analyze several other energy related variables such as the energy per hit in a slice (Figure 7.5a) and the energy of the leading shower in a slice (Figure 7.5b) after pre nue selection cuts, both of which are peaked a bit lower in data than the MC. We later determined that the discrepancy is caused by the poorly modeled hadronic energy in the simulation. Uncertainty associated with this mismodeling is evaluated in Chapter 8.

	Total MC	Efficiency		ν_μCC	ν_eCC	NC	Data	Efficiency	
No cut	30049057	100.00%		25742957	364671	3941430	29802297	100.00%	
Data quality	29139394	96.97%		25132969	339183	3667242	29015588	97.36%	
Reconstruction	16338569	54.37%		13577267	229803	2531499	15996841	53.68%	
Fiducial	1139793	3.79%		758778	20924	360091	1025407	3.44%	
Containment	478835	1.59%		253650	10236	214949	424518	1.42%	
Front planes	461975	1.54%		243569	9815	208592	413242	1.39%	
Slice hits and E_{cal}	323131	1.08%		177970	5437	139724	301019	1.01%	
Shower length	236834	0.79%		145944	4859	86030	222046	0.75%	
Gap	230475	0.77%	100.00%	142987	4755	82732	217656	0.73%	100.00%
LEM	3225	0.01%	1.40%	1047	985	1193	3395	0.01%	1.56%
LID	2471	0.01%	1.07%	396	1292	783	2579	0.01%	1.18%

TABLE 7.1: ν_e selection performance and efficiencies in the Near detector for both MC and data. MC is normalized to the data POT 1.66×10^{20}.

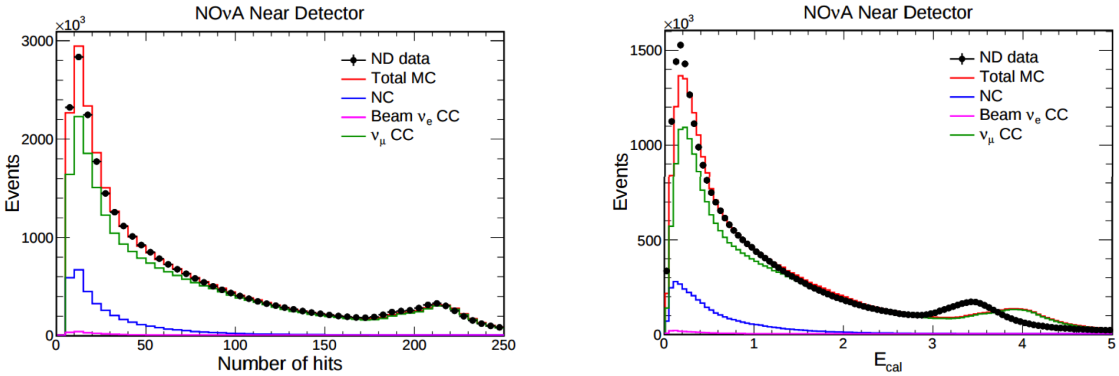

a Number of hits

b Calorimetric Energy

FIG. 7.3: ND number of hits in slice distribution (*Left*) and calorimetric energy distribution (*Right*) for data (black) and MC (red) after all ν_e preselection cuts.

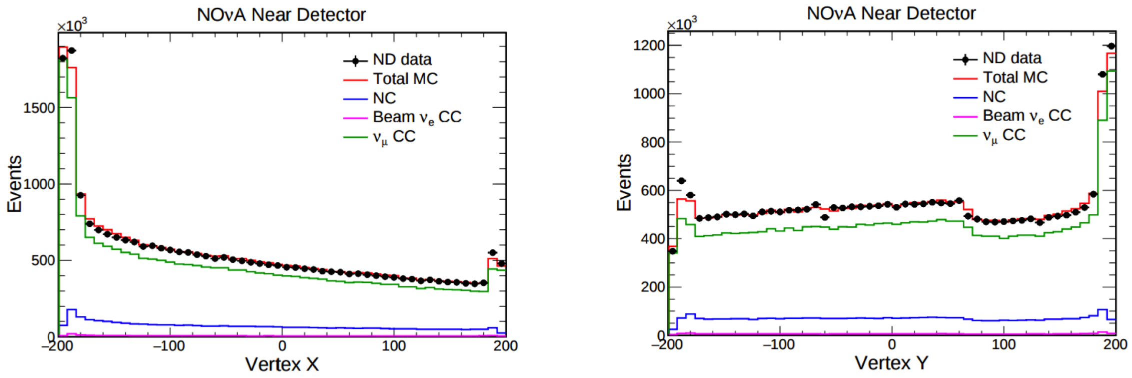

a Interaction vertex X b Interaction vertex Y

FIG. 7.4: ND interaction vertex position X (*Left*) and Y (*Right*) distributions for data (black) and MC (red) after ν_e preselection. The slope shape is due to the off-axis feature of the NOνA detectors.

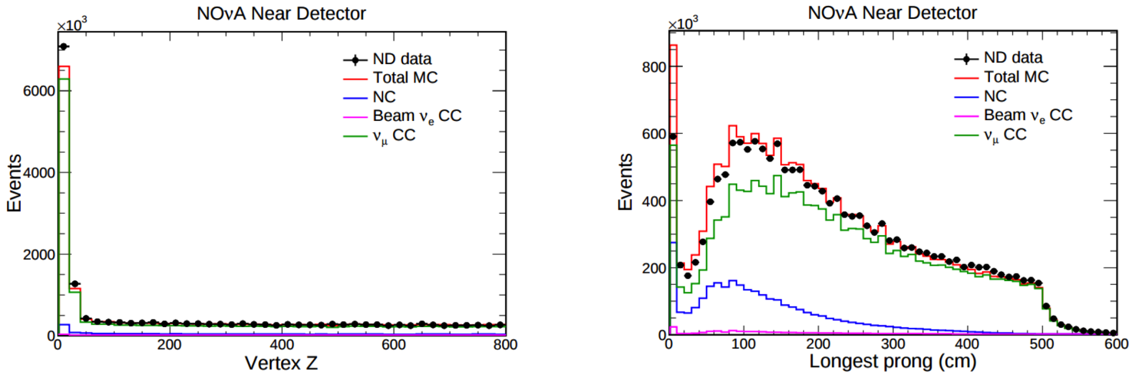

a Interaction vertex Z b Length of the longest prong

FIG. 7.5: ND interaction vertex Z distributions (*Left*) and length of the longest prong in a slice (*Right*) for data (black) and MC (red) after ν_e preselection.

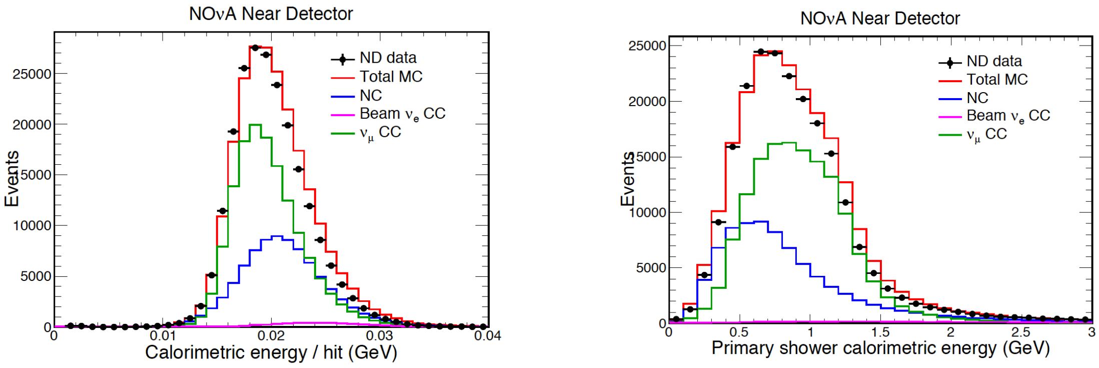

a Energy per hit

b Leading shower energy

FIG. 7.6: ND energy per hit in a slice (*Left*) and leading shower energy in a slice (*Right*) distributions for data (black) and MC (red) after ν_e preselection.

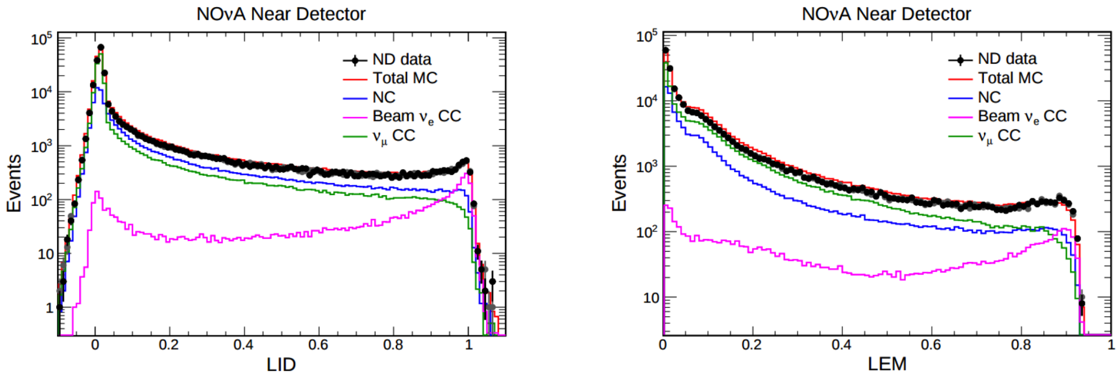

a LID

b LEM

FIG. 7.7: ND LID (*Left*) and LEM (*Right*) distributions for data (black) and MC (red) after ν_e preselection.

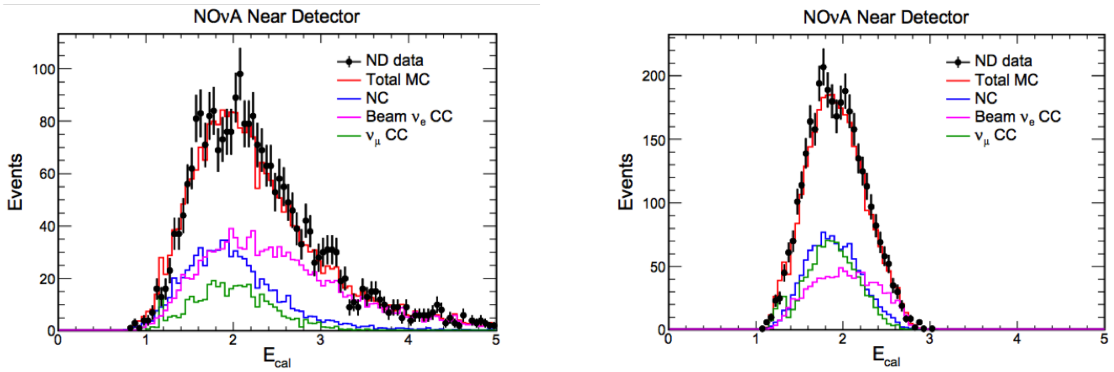

a LID b LEM

FIG. 7.8: ND calorimetric energy distributions for data (black) and MC (red) after LID (*Left*) and LEM (*Right*) selection. This is the spectrum that we extrapolate to the FD.

7.2.2 FD Data vs. MC Comparison

For the Far detector, since we are performing a blind analysis, the FD beam events are concealed until all analysis tools are tuned. We only use FD cosmic ray data to make the data vs. MC comparison. These cosmic events are not expected to look ν_e like, but it tell us about the performance of detector and the simulation model. As a cosmic muon goes through our detector it produces EM showers through Bremsstrahlung and decay in flight. The EM shower induced by the cosmic ray is an important tool to benchmark our simulation and selection of EM showers. In these cosmic events, we removed the hits associated with the muon track, then reconstructed the remnant EM shower. Figure 7.8a-7.10b show these muon removed cosmic data and MC comparisons for some key variables from the shower reconstruction and LID, all of which have good agreement and demonstrates the EM showers, cosmic events and FD geometry are all well modeled in our simulation [95].

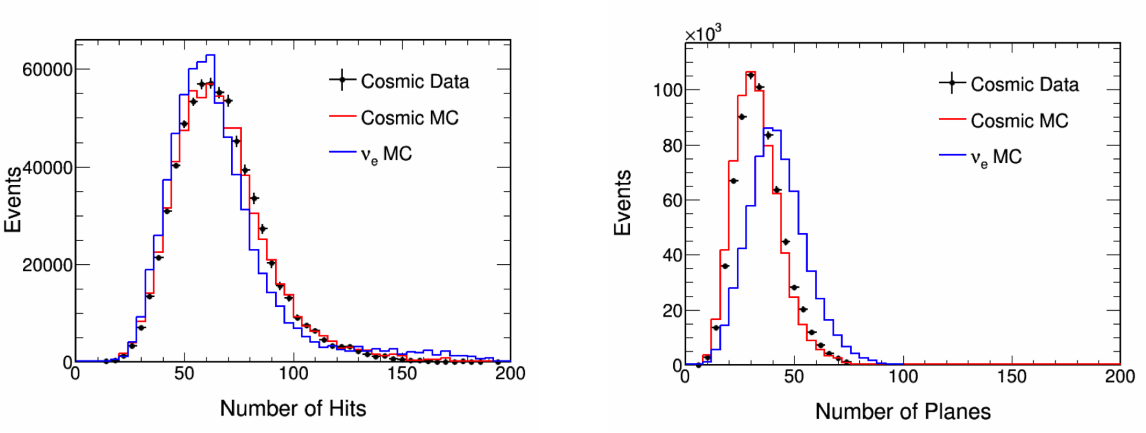

a Number of hits.

b Number of planes.

FIG. 7.9: FD number of hits (*Left*) and planes (*Right*) distributions for cosmic data (black) and cosmic MC (red), while ν_e MC (blue) are shown for reference.

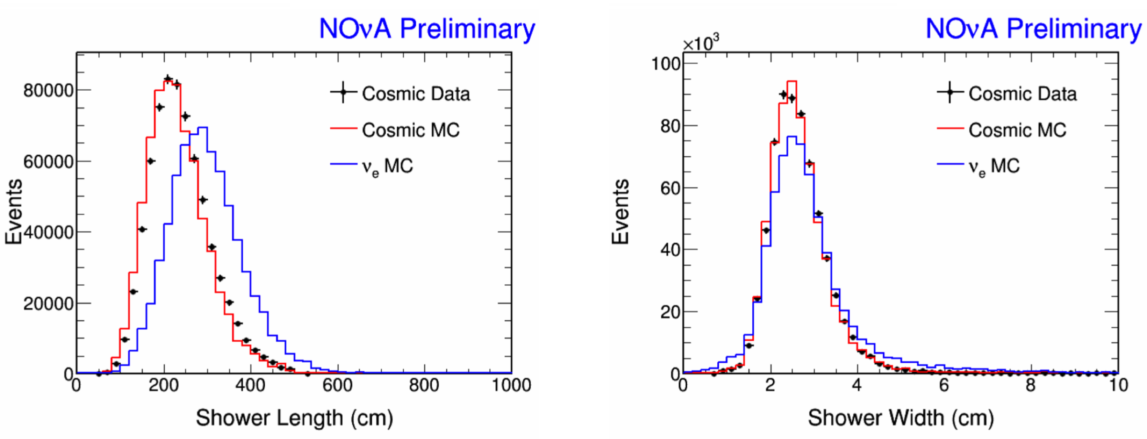

a Reconstructed shower length b Reconstructed shower radius

FIG. 7.10: FD reconstructed shower length (*Left*) and reconstructed shower radius (*Right*) distributions for cosmic data (black) and cosmic MC (red), while ν_e MC (blue) are shown for reference.

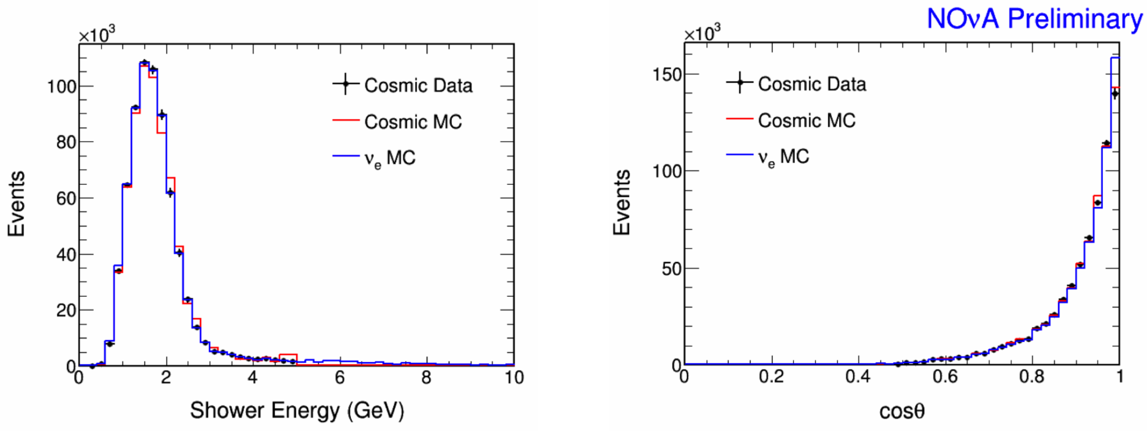

a Reconstructed shower energy

b Reconstructed shower angle

FIG. 7.11: FD reconstructed shower energy (*Left*) and reconstructed shower angle (*Right*) distributions for cosmic data (black) and cosmic MC (red), while ν_e MC (blue) are shown for reference.

7.3 Decomposition

The NOνA Near detector measures the neutrino beam before oscillations occur, and is designed to predict the background in the Far detector to the ν_e appearance signal. To serve this purpose, we first need to classify the neutrino interactions in the ND into three major event types beam, $\nu_e CC$, $\nu_\mu CC$, and NC since their oscillation channels and behavior at different distances are different. Then we analyze the behaviors of different event types and extrapolate each component to the Far detector separately.

The decomposition method we chose for the first analysis is called the proportional decomposition. It takes the ratio of each true neutrino interaction type to the total in the ND MC after the ν_e selection cut, and scales them by the ND data to estimate the event counts for each type. This decomposition is performed separately for each bin of reconstructed neutrino energy as following:

$$N^{Data}_{\alpha,S_e}(B_j) = N^{Data}_{Tot,S_e}(B_j)\frac{N^{MC}_{\alpha,S_e}(B_j)}{N^{MC}_{Tot,S_e}(B_j)} \tag{7.1}$$

where N represents the Near detector component α of data or MC, where α is one of the three neutrino background types beam $\nu_e CC$, $\nu_\mu CC$ or NC. S_e denotes that the ν_e selection is applied, and B_j is the j^{th} reconstructed energy bin. We find the background is 31.7% NC, 16% $\nu_\mu CC$, and 52% beam $\nu_e CC$.

7.4 Extrapolation

As we mentioned previously, NOνA's two functionally-identical detectors allow us to predict the Far detector background with Near detector data to reduce the systematic errors. The technique we used to make the prediction is called "extrapolation" [21].

The extrapolation's feasibility is based on the assumption that the events selected in the Near detector represent the Far detector backgrounds. In that case the kinematic behavior of the neutrino interaction in the two detectors should be very similar. To verify this assumption, we compare the distributions of two invariant kinematic variables between the two detectors. The first one Q^2, as defined in Equation 7.2, represents the four-momentum transfer. The other one, W^2, as defined in Equation 7.3, is the mass of the system recoiling against the scattered lepton.

$$Q^2 = -q^2 = 2\left(EE' - \vec{\kappa}\cdot\vec{\kappa}'\right) - m_l^2 - m_{l'}^2 \tag{7.2}$$

$$W^2 = \left(P+q\right)^2 = M^2 + 2M\left(E - E'\right) - Q^2 \tag{7.3}$$

As illustrated in Figure 7.12, E, $\vec{\kappa}$ and m_l represent the energy, four-momenta and mass of the incident lepton respectively, and E', $\vec{\kappa}'$ and $m_{l'}$ are the same kinematic variables for the outgoing lepton. For the other party in the scattering, the nucleon, P and M stand for its four-momentum and mass. The comparison of these distributions between the detectors are shown after LID selection (Fig 7.13), or LEM selection (Fig 7.14). Here the ND MC are shown in color while FD MC are illustrated by overlaid box. The excess in high energy MC compared to data in these plots came from the neutral current scattering, which is an effect that has been considered when calculating the systematic uncertainty in Chapter 8. Overall, the peak and distribution are consistent, which proves the ND selection contains a good representative sample for FD prediction.

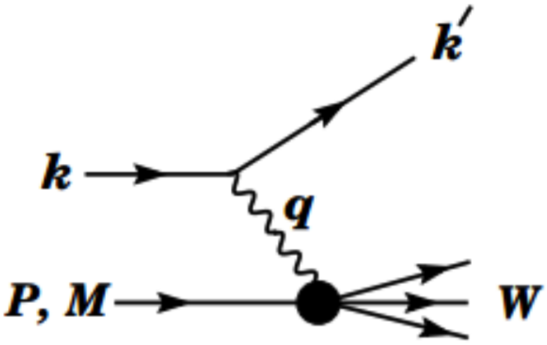

FIG. 7.12: Feynman diagram for lepton-nucleon scattering labeled with its kinematic quantities [21].

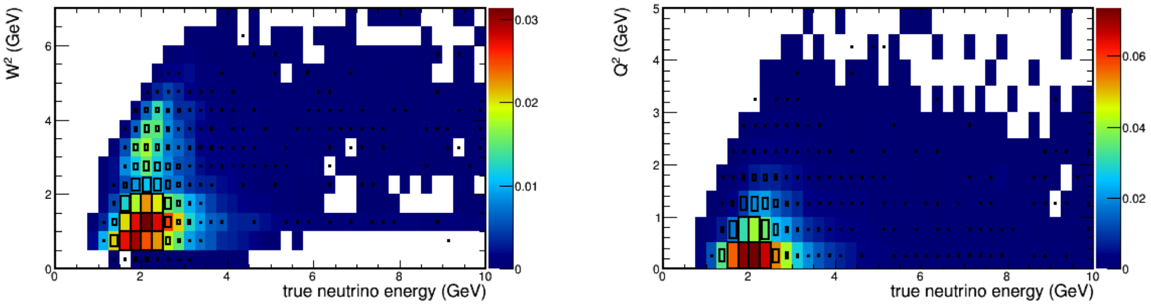

FIG. 7.13: The ND MC distribution of W^2 (left) and Q^2 (right) vs. true neutrino energy after the LID selection cut shown in color. Overlaid boxes are FD MC selected events [21].

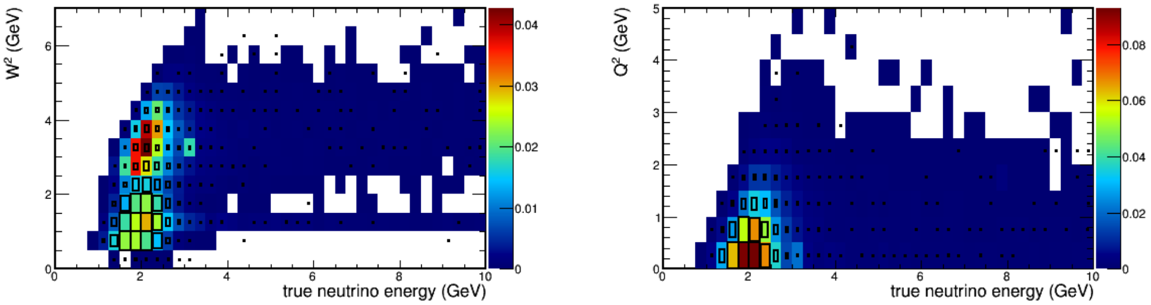

FIG. 7.14: The ND MC distribution of W^2 (left) and Q^2 (right) vs. true neutrino energy after the LEM selection cut shown in color. Overlaid boxes are FD MC selected events [21].

Using the decomposed Near detector data components as calculated in Section 7.3 Equation 7.1, we scale the ND data with the FD/ND MC ratio for each event type to estimate the FD event rate. The FD background extrapolation is performed in each energy bin through each background channel as below:

$$F^{Pred}_{\alpha\to\alpha,S_e}(E_i, B_j) = N^{Data}_{\alpha,S_e}(B_j)\frac{F^{MC}_{\alpha\to\alpha,S_e}(E_i, B_j)}{N^{MC}_{\alpha,S_e}(B_j)} \tag{7.4}$$

where E_i is true neutrino energy bins and convoluted with the reconstructed energy bins by a matrix created using MC, and $\alpha \to \alpha$ is the background oscillation channels ($\nu_e \to \nu_e$, $\nu_\mu \to \nu_\mu$, $\nu_x \to \nu_x\ NC$). Other denotations are the same as described for Equation 7.1. Then we can calculate the FD background prediction by applying the oscillation probability $P_{\alpha\to\alpha}(E_i)$ using:

$$F^{Pred}_{\alpha\to\alpha,S_e}(B_j) = \sum_i F^{Pred}_{\alpha\to\alpha,S_e}(E_i, B_j)P_{\alpha\to\alpha}(E_i). \tag{7.5}$$

In this Chapter, the oscillation probability $P_{\alpha\to\alpha}(E_i)$ we are using assumes no matter effect or CP violation with $\Delta m^2_{32} = 2.35 \times 10^{-3}$, $\sin^2 2\theta_{23} = 1$, and $\sin^2 2\theta_{13} = 0.1$. Besides the three major oscillation channels, there are also eight minor background channels: $\nu_e \to \nu_\mu$, $\nu_e \to \nu_\tau$, $\nu_\mu \to \nu_\tau$, $\bar{\nu_e} \to \bar{\nu_e}$, $\bar{\nu_e} \to \bar{\nu_\mu}$, $\bar{\nu_e} \to \bar{\nu_\tau}$, $\bar{\nu_\mu} \to \bar{\nu_\mu}$, $\bar{\nu_\mu} \to \bar{\nu_\tau}$. The FD prediction for these eight background channel are taken directly from FD MC since their event rates are very small.

For the FD signal channels $\nu_\mu \to \nu_e$ and $\bar{\nu_\mu} \to \bar{\nu_e}$, the extrapolation is performed using

ν_μ selection in the ND instead of ν_e selection for background. Also, the ND event rate is converted into true energy because the ν_μ selection has a different reconstructed energy resolution. Then the ND true spectrum is extrapolated using:

$$N^{Pred}_{\nu_\mu,S_\mu}(E_j) = \sum_i \frac{N^{Data}_{\nu_\mu,S_\mu}(B_k)}{N^{MC}_{\nu_\mu,S_\mu}(B_k)} N^{MC}_{\nu_\mu,S_\mu}(E_i, B_k). \tag{7.6}$$

Then, similar to the background extrapolation, the FD signal is predicted by:

$$F^{Pred}_{\nu_\mu\to\nu_e,S_\mu}(E_i, B_j) = N^{Data}_{\nu_\mu,S_\mu}(E_i)\frac{F^{MC}_{\nu_e,S_e}(E_i, B_j)}{N^{MC}_{\nu_\mu,S_\mu}(E_i)} \tag{7.7}$$

$$F^{Pred}_{\nu_\mu\to\nu_e,S_e}(B_j) = \sum_i F^{Pred}_{\nu_\mu\to\nu_e,S_\mu}(E_i, B_j) P_{\nu_\mu\to\nu_e}(E_i). \tag{7.8}$$

7.5 Far Detector Background and Signal Prediction

Figure 7.15 (for LID selector) and 7.16 (for LEM selector) show the energy distribution that was used in the key steps of the extrapolation for each background channel. For the ND we show the comparison between data and MC, while for the FD the comparison is made between prediction and MC.

The final background and signal prediction event counts are listed in Table 7.2. The cosmic background prediction comes from an out-of-time NuMI trigger sample (more details in Section 6.3.3). These numbers are normalized to the FD first analysis POT 3.45×10^{20} to represent our predicted event counts for each type of component from the

	Signal	Total Bkg.	Beam ν_e	NC	ν_μ CC	ν_τ CC	Cosmic
LID FD prediction	4.33	0.94	0.05	0.46	0.36	0.02	0.06
LEM FD prediction	4.53	1.00	0.06	0.46	0.40	0.02	0.06
LID FD MC	4.28	0.90	0.05	0.44	0.33	0.02	0.06
LEM FD MC	4.45	0.97	0.07	0.44	0.38	0.02	0.06

TABLE 7.2: The FD extrapolation predicted result for signal and background components using different particle selectors (LID and LEM). The FD MC event counts are also listed for comparison. The numbers are normalized to 3.45×10^{20} POT to agree with the FD first analysis exposure.

data. Thus we expect to see 4.33 oscillated $\nu_e CC$ signal events on a background of 0.94 events after LID selection, and 4.53 signal events on a background of 1.00 events after LEM selection.

By comparing the FD prediction (top two rows) and FD MC (bottom two rows) in Table 7.2, we expect slightly higher event counts for both signal and background in prediction than MC. This can be traced back to the ND data excess with respect to MC as mentioned in Section 7.2.2 and is taken account in the systematic uncertainties that will be discussed in detail in the next chapter.

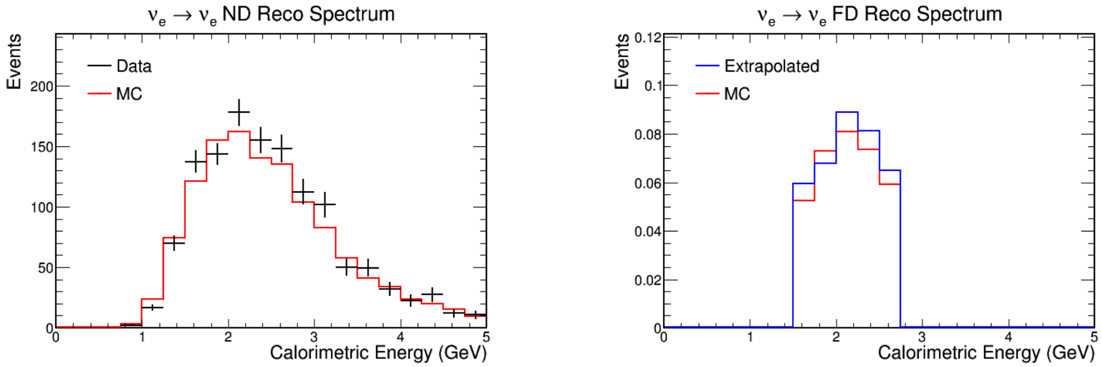

a Near Detector, $\nu_e \rightarrow \nu_e$ b Far Detector, $\nu_e \rightarrow \nu_e$

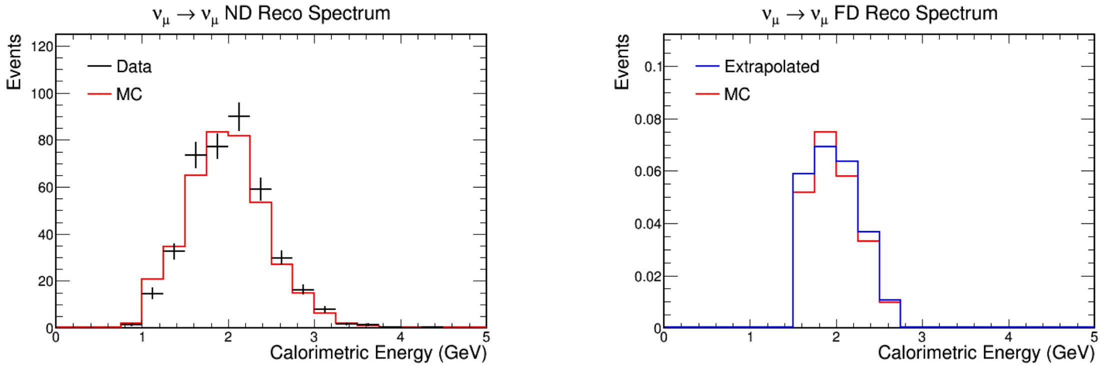

c Near Detector, $\nu_\mu \rightarrow \nu_\mu$ d Far Detector, $\nu_\mu \rightarrow \nu_\mu$

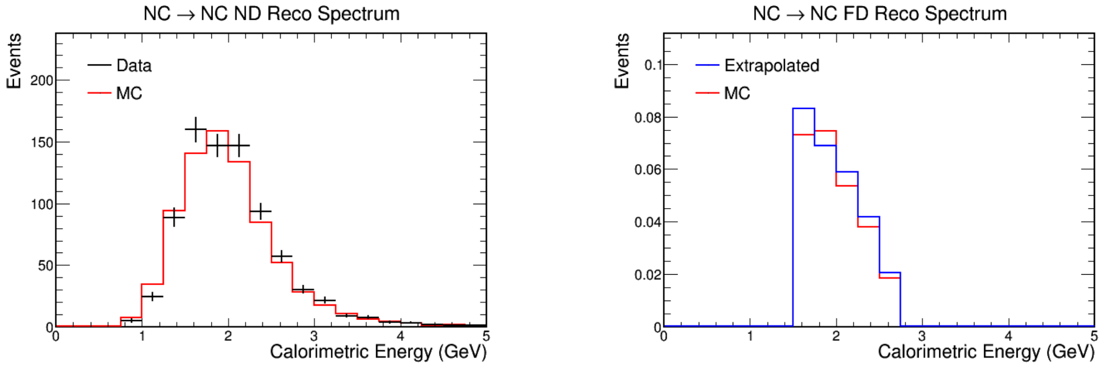

e Near Detector, Neutral-Current f Far Detector, Neutral-Current

FIG. 7.15: Reconstructed energy spectrums in ND for data and MC (left), and in FD for prediction and MC (right) after LID selection for the major background channels: $\nu_e \rightarrow \nu_e$ (a, b), $\nu_\mu \rightarrow \nu_\mu$ (c, d), and neutral current (e, f).

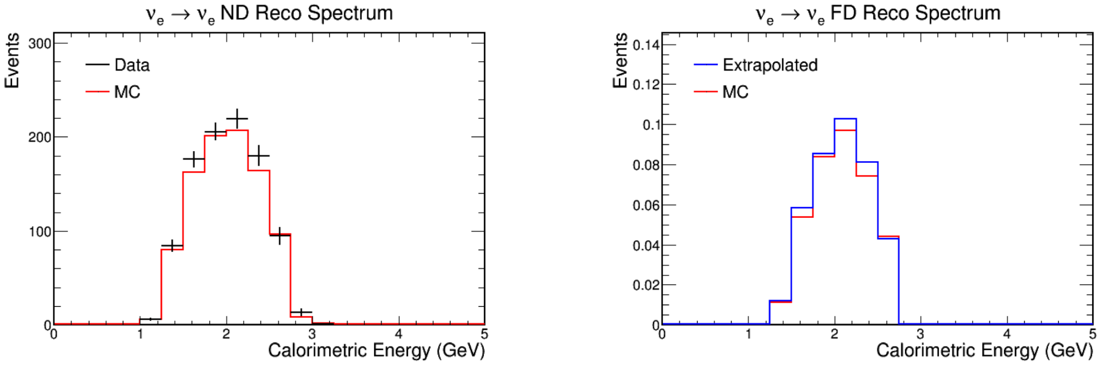

a Near Detector, $\nu_e \rightarrow \nu_e$

b Far Detector, $\nu_e \rightarrow \nu_e$

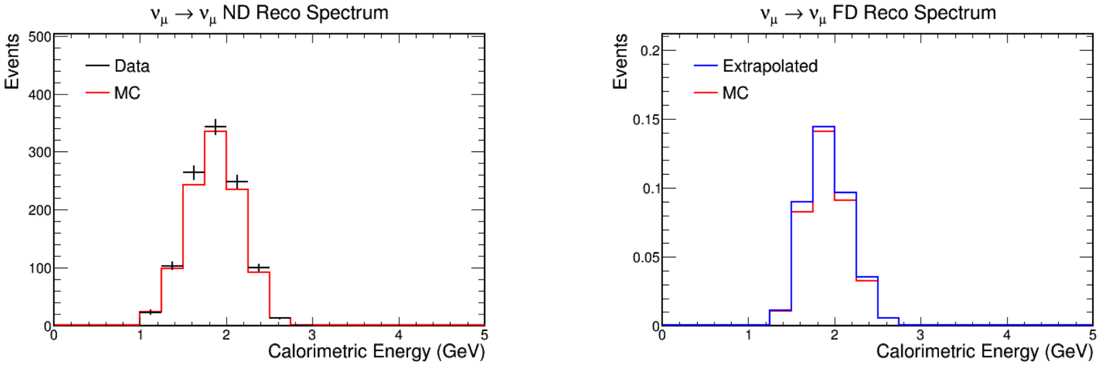

c Near Detector, $\nu_\mu \rightarrow \nu_\mu$

d Far Detector, $\nu_\mu \rightarrow \nu_\mu$

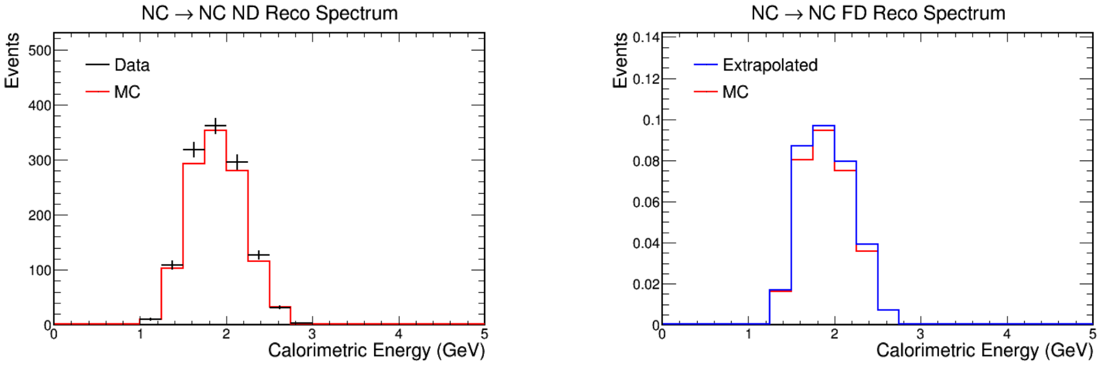

e Near Detector, Neutral-Current

f Far Detector, Neutral-Current

FIG. 7.16: Reconstructed energy spectrums in ND for data and MC (left), and in FD for prediction and MC (right) after LEM selection for the major background channels: $\nu_e \rightarrow \nu_e$ (a, b), $\nu_\mu \rightarrow \nu_\mu$ (c, d), and neutral current (e, f).

CHAPTER 8

Systematics

The two NOνA detectors are designed to be functionally identical in order to cancel most of the systematic uncertainties using the extrapolation techniques described in Chapter 7. However, due to the different sizes of the two detectors and the limited statistics for the first analysis, some systematic errors remain. In this chapter, the main contributing systematic sources are described and their effects on the first analysis results are quantified [22].

These systematic errors are analyzed in different ways. Some effects, such as scintillator saturation and calibration have effects on the event topologies or the composition of the types of interaction, thus require generating systematically modified MC samples for both detectors. By comparing the modified FD prediction, obtained by performing the extrapolation using the systematically modified MC, with the nominal FD prediction, we calculate percentage change as the systematic error for each event type. Beam flux and neutrino interaction uncertainties, on the other hand, do not change event topology, just the abundance of each event type. Thus their systematic errors are analyzed using an event weight. Other evaluation methods will be discussed separately for each effect in their section.

8.1 Beam Systematic Uncertainties

The uncertainties of the NuMI neutrino beam flux observed at the two NOνA detectors are classified into two categories: *Beam transport*, which refers to the variance of the actual beam configuration such as horn current, beam size, beam position etc, and *Hadron production*, which refers to the uncertainty in the beam simulation arising from the modeling of the hadron production at the target [96] [97]. To quantify the systematic uncertainties, modified MC samples were produced with the beam transport and hadron production variables shifted 1σ up and down for both detectors and used in the extrapolation to make the FD prediction. The shifted prediction from each systematic variable is compared to the nominal extrapolation to produce the uncertainties.

Figure 8.1 shows ND Data/MC comparisons distribution with beam systematic errors for calorimetric energy and LID. The effect is similar in the FD thus the large error is cancelled in the extrapolation. Table 8.1 shows the the main beam systematic uncertainties for the first analysis. These results average the shift up/down (if available) and are presented as percent differences between the shifted and nominal extrapolation. By summing each uncertainty in quadrature, we find the overall beam uncertainty to be 1.06% on the ν_e

Diff %	LID		LEM	
	Signal	Background	Signal	Background
Horn Current	0.04	0.17	0.04	0.12
Beam Spot Size	0.05	0.08	0.05	0.13
BeamPosX	0.14	0.36	0.11	0.32
BeamPosY	0.11	0.03	0.09	0.02
H1Pos	0.23	0.33	0.21	0.40
H2Pos	0.03	0.23	0.01	0.28
TargetPos	0.02	0.14	0.02	0.04
ExpMagnField	0.01	0.38	0.02	0.35
Hadron Production Simulation	1.01	3.10	1.01	2.77
Total	1.06	3.18	1.04	2.85

TABLE 8.1: Percentage difference between nominal and each systematically modified FD prediction for signal and background after LID or LEM selection for each beam related systematic uncertainty. The last row corresponds to the quadrature sum of all errors in the table.

appearance signal and 3.18% on the background for LID selector, while for LEM selector the values are similar with 1.04% on the signal and 2.85% on the background.

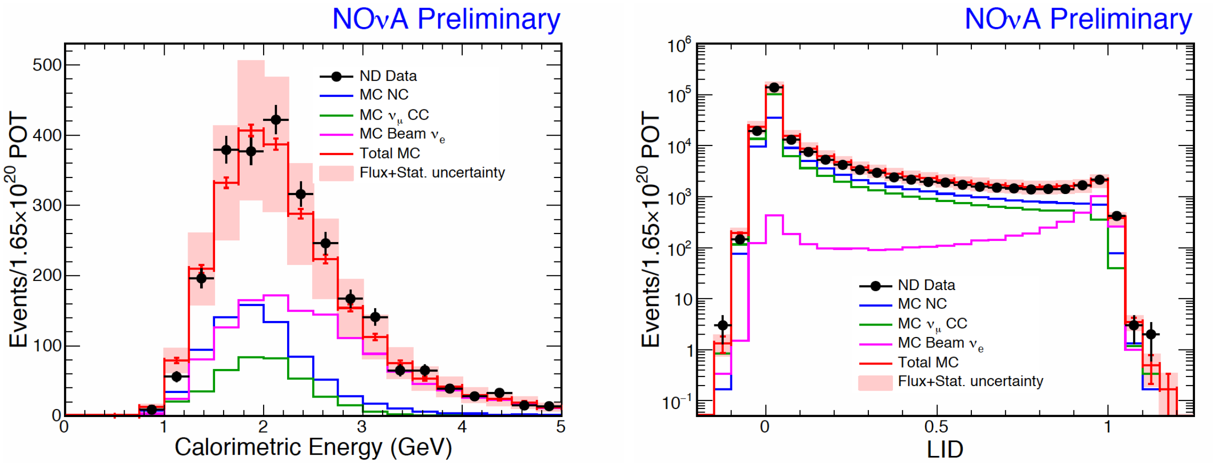

FIG. 8.1: ND Data/MC comparisons distribution with beam systematic errors: Left plot shows the reconstructed energy after LID selection (left), and Right plot shows the LID distribution after preselection.

8.2 Scintillator Saturartion Systematic Uncertainties

The NOνA detectors are filled with scintillator to observe the trajectory and energy of the daughter particles created in neutrino interactions. This measurement assumes the light yield is proportional to the energy deposition. However, at high energy deposition rates, the scintillator saturates and the light yield begins to quench. An empirical Birks-Chou law [98] with high loss rates correction is used to describe the effect :

$$\frac{dL}{dX} = \frac{A\frac{dE}{dx}}{1 + k_B\frac{dE}{dx} + k_C\frac{dE}{dx}^2}$$

where L is the light yield, k_B and k_C are two scintillator material dependent parameters. Using NOνA Near detector data, we measured $k_B = 0.04\ \frac{g}{MeV \cdot cm^2}$ and $k_C = -0.00005\ \frac{g^2}{MeV^2 \cdot cm^4}$. While providing the best description of our data, these are a factor of four times higher than the typical measurements from other experiments [99]. Therefore to be conservative, two modified MC samples are generated for both detectors with two sets of typical k parameters, one named BirksB with $k_B = 0.01\ \frac{g}{MeV \cdot cm^2}$ and $k_C = 0$, while the other named BirksC with $k_B = 0.02\ \frac{g}{MeV \cdot cm^2}$ and $k_C = 0$. Using the shifted MC we made the FD prediction and compared with nominal. The percentage differences using the different selectors are shown in Table 8.2. Results of the larger shifted MC set BirksC are chosen as the final scintillator saturation systematic uncertainties with 7.2% on the signal and 5.1% on the background for LID.

Diff (%)	Signal	Background
LID BirkB	-5.12	-8.80
LID BirkC	-7.22	-5.14
LEM BirkB	-6.28	-3.22
LEM BirkC	-7.94	-4.62

TABLE 8.2: Percentage difference between the nominal and the Birks-Chou systematically modified FD predictions for signal and background after LID or LEM selection.

8.3 Calibration Systematic Uncertainties

The two NOνA detectors are calibrated separately with different cosmic muon samples due to the differences in each detector's size and location. Thus the calibration systematic, which comes from imperfections of the detector calibration, is expected to be one of the major sources of systematic error. In this analysis, we generated deliberately mis-calibrated Monte Carlo samples in both detectors and processed it through the extrapolation procedure to compute the changes in event counts.

There are three artificial mis-calibrations that we studied for this analysis: an absolute calibration shift, a gradient calibration shift as a function of position along cell length, and a random cell by cell calibration offset. Details of each type of mis-calibration are listed below:

- Absolute mis-calibration:

  The absolute mis-calibration MC sample is achieved by offsetting the energy calibration scale by ±5%. This 5% error is determined from a study of Michel electrons' reconstructed energy. A Michel electron is produced in decays of muons at rest and present a well understood energy spectrum that can be used as a tool to check the muon energy calibration. As shown in Figure 8.2, the data/MC comparison of the Michel electron energy spectrum in ND (left) and FD (right) shows a discrepancy that indicates the mis-calibration level in the detectors. The data/MC ratio of the mean energy scale is 0.958 in ND while 1.005 in FD, from which we conservatively estimated a 5% absolute mis-calibration in both detectors.

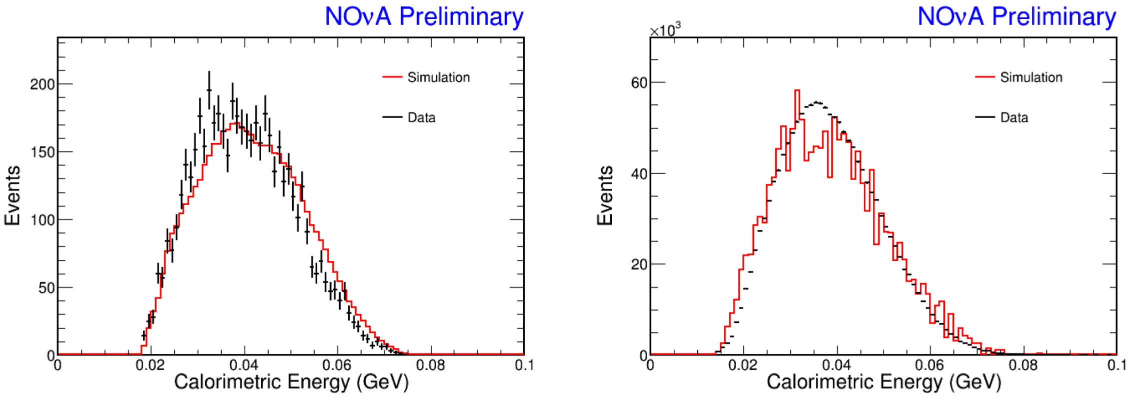

FIG. 8.2: ND (left) and FD (right) data/MC comparisons distribution of the Michel Electron energy spectrum [22].

Using the mis-calibrated MC from both detectors, the extrapolation process is performed to get a FD prediction. The left plots in Figure 8.3 shows the ND data vs. mis-calibrated MC comparison for each oscillation channel, while the right plots shows the FD prediction with shifted extrapolation vs. nominal MC, which served as fake data. By comparing the predicted events count using nominal and mis-calibrated extrapolation, a 0.76% change in total background and a 5.98% change in signal is found when using the primary selector LID, while for LEM the numbers are 5.80% in total background and 1.20% in signal.

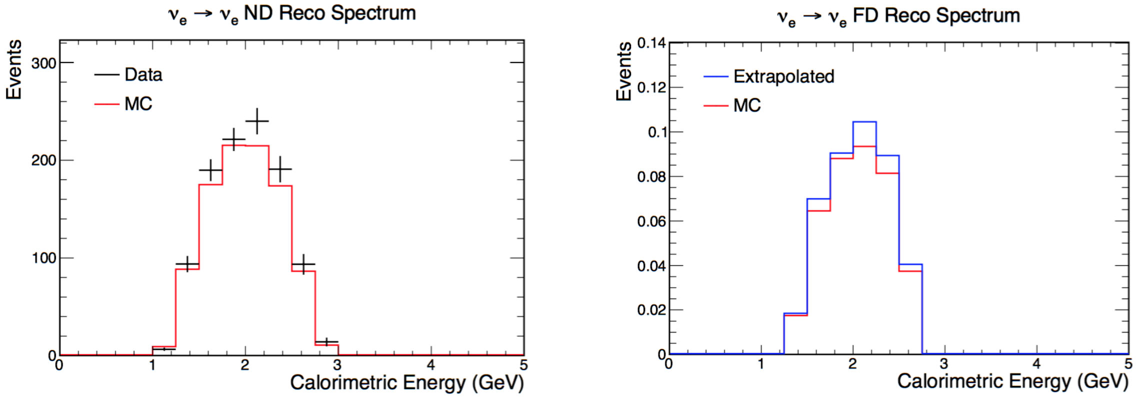

a Near Detector, $\nu_e \rightarrow \nu_e$.

b Far Detector, $\nu_e \rightarrow \nu_e$.

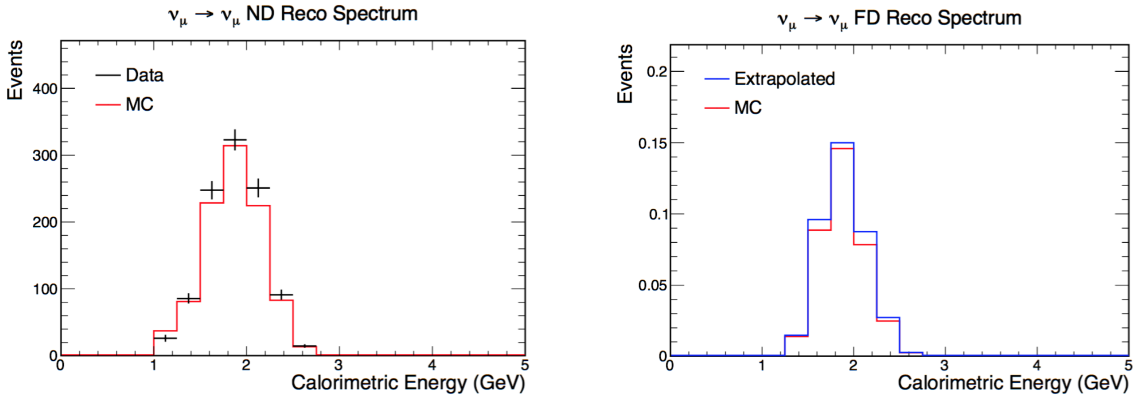

c Near Detector, $\nu_\mu \rightarrow \nu_\mu$.

d Far Detector, $\nu_\mu \rightarrow \nu_\mu$.

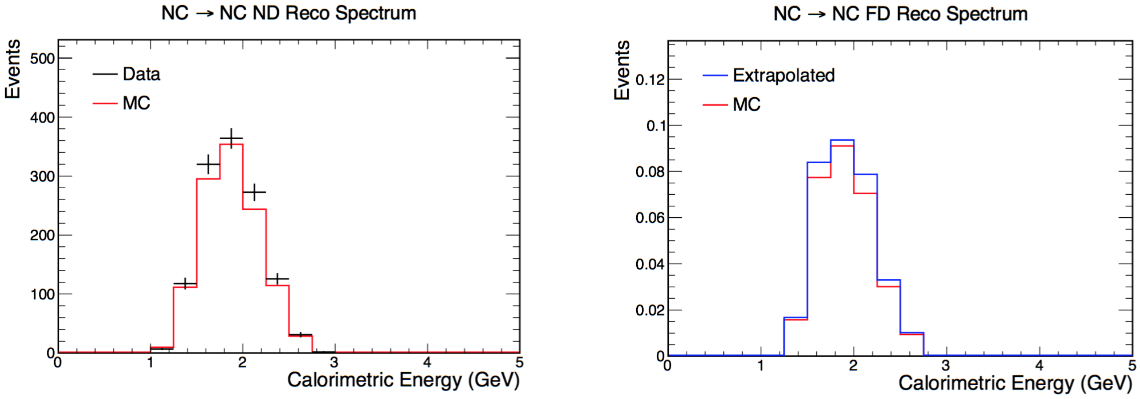

e Near Detector, Neutral-Current.

f Far Detector, Neutral-Current.

FIG. 8.3: Reconstructed energy spectra for the absolute calibration systematics study. Left plots show data (black dots) and mis-calibrated MC(red lines) in ND, while right plots show the predicted spectrum using mis-calibration ND/FD ratio (Blue) and nominal MC (Red) in FD. Top, middle and bottom plots display the different background channels respectively: $\nu_e \rightarrow \nu_e$ (a, b), $\nu_\mu \rightarrow \nu_\mu$ (c, d), and neutral current (e, f).

- Gradient (relative) mis-calibration:

  The gradient (relative) mis-calibration, which is an artificial calibration shift that depends on the length of a cell, represents a systematic error in the attenuation constant between data and MC during calibration. Because of the larger size of FD, this effect is bigger at the far end of an FD cell than in ND cells. For the first analysis, the mis-calibration effect is described using a polynomial that is fit to the data/mc ratio of detector response as a function of cell length. A ±8% attenuation difference between the near end and the far end is applied to generate the mis-calibrated MC samples as shown in Figure 8.4. These mis-calibrated MC are then used to calculate the systematic error in the same process used for the absolute mis-calibration. Overall, the uncertainties are -1.51% for signal and -3.21% for the total background after LID selection.

- Random cell-by-cell mis-calibration:

  In NOνA, the attenuation calibration is performed in each cell, thus the quality might fluctuate from cell to cell, which could bring in systematic error. In the first analysis, the artificial mis-calibration for this effect is simulated by smearing the cell attenuation constant by a gaussian with 8% width. Figure 8.5 shows the calorimetric energy distribution for the mis-calibrated MC compared with nominal MC. The systematic uncertainty is calculated in the same process as others, and presents very small figures with -0.93% for signal and -0.39% for the total background after LID selection.

Final systematic uncertainties of the three mis-calibration effects are listed in Ta-

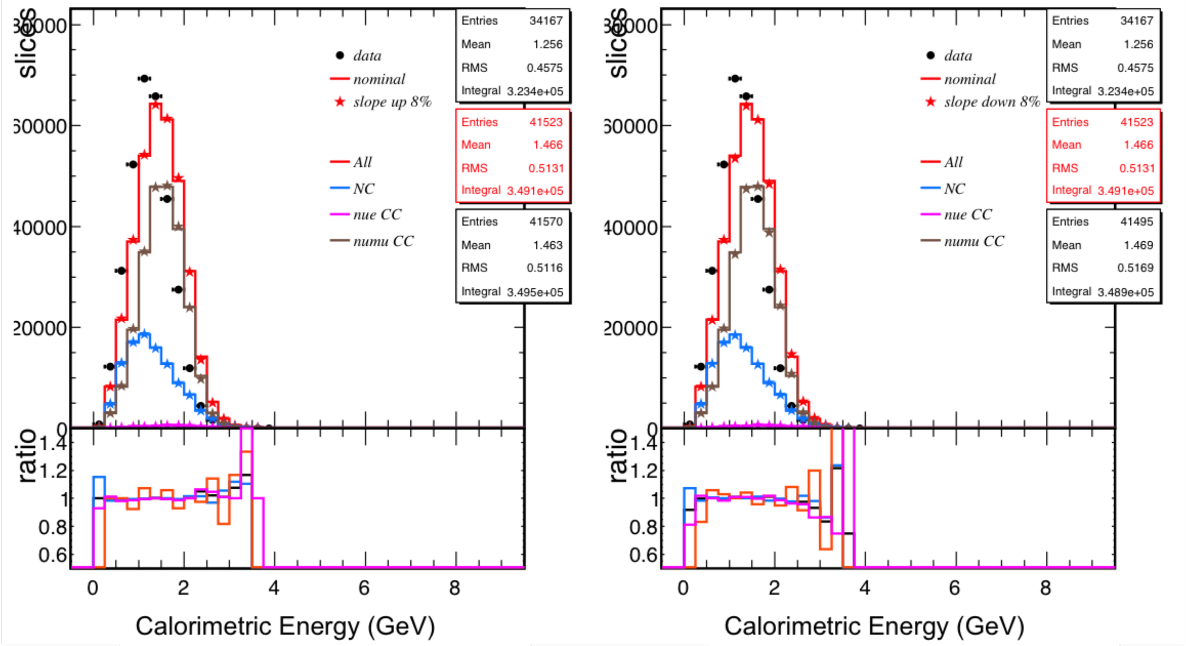

FIG. 8.4: ND calorimetric energy spectrum for 8% gradient mis-calibration shift up (left) and down (right) compared to the nominal after the LID selection.

ble 8.3. The numbers are broken down into signal and background components for each PID selection after extrapolating the calibration shifts compared to nominal. For each effect, the final figure comes from averaging the up and down shifts. The total calibration systematic error is the quadrature sum, which is 7.58% in signal and 4.44% in total background for LID selection, and 3.68% in signal and 7.90% in total background for LEM selection.

8.4 Light Level Systematic Uncertainties

The light-level determines the amount of photons that are produced by an energy deposition. During the analysis, we found some evidence indicating that the light-level in

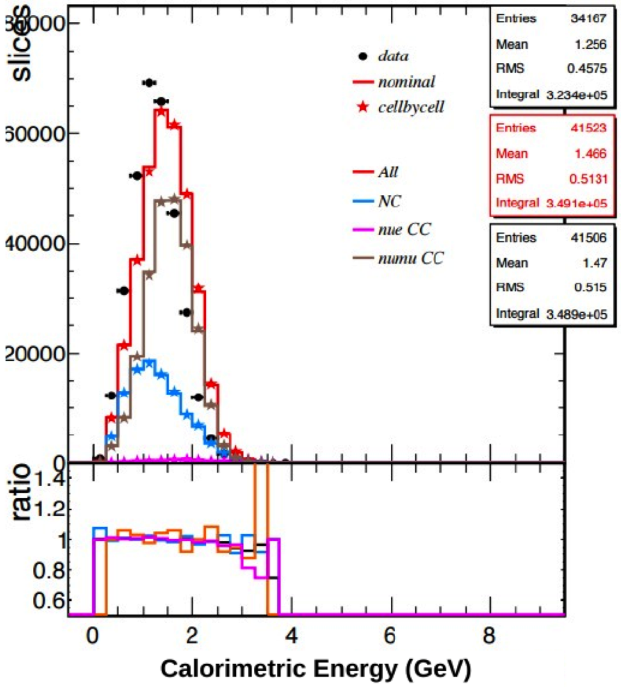

FIG. 8.5: ND calorimetric energy spectrum for Random cell-by-cell mis-calibration MC compare to the nominal after the LID selection.

the Far detector is underestimated (see Figure 8.6) and should be adjusted [23]. The first order impact of this light-level issue is removed by the calibration procedure. However, there is a residual effect of non-noise hits falling below threshold and failing to trigger readout. We further study this effect by evaluating the MC selection efficiency with a shifted threshold, in which the numbers of selected events vs. vertex position shows a 5% discrepancy at the far cell end [100]. This effect is projected to a 1% systematic error on the signal for the ν_e analysis, and is negligible on the background.

	LID				
% diff	signal	total bkg.	ν_μ CC	NC	beam ν_e CC
Absolute	5.98	0.76	8.45	10.81	10.89
Relative	4.36	3.72	12.07	15.65	6.39
Random	-0.93	-0.39	1.47	1.47	1.87
Slope	1.33	2.27	2.94	10.51	3.92
Total	7.58	4.44	15.10	21.78	13.35

	LEM				
% diff	signal	total bkg.	ν_μ CC	NC	beam ν_e CC
Absolute	1.20	5.80	12.25	0.81	10.36
Relative	2.84	4.22	10.46	1.87	8.33
Random	-1.33	-0.80	1.09	-0.42	1.43
Slope	-1.51	-3.21	-4.35	1.06	6.45
Total	3.68	7.90	16.72	2.34	14.84

TABLE 8.3: Calibration systematic error relative change from nominal for the signal and background components of LEM and LID selections.

8.5 Neutrino Interaction Systematic Uncertainties

In Chapter 4, we described how the neutrino interactions are simulated in NOνA. To evaluate the simulation uncertainties, a MC reweighting tool embedded in GENIE provided a way to vary 33 neutrino interaction parameters within the interaction model. The available "knobs" fall generally into three categories: cross-section uncertainties, hadronization model uncertainties, and uncertainties due to final state interactions. The size of the systematic modification of each parameter comes from the GENIE authors based on a careful survey of the interaction model using data collected from various experiments [18]. Below is a full list of the 33 parameters that we considered in the systematics study. The percentage adjustment is the change of the weight for a 1 sigma tweak of the knob up/down, which is the weight that we used in the analysis (except the axial mass in quasi-elastic

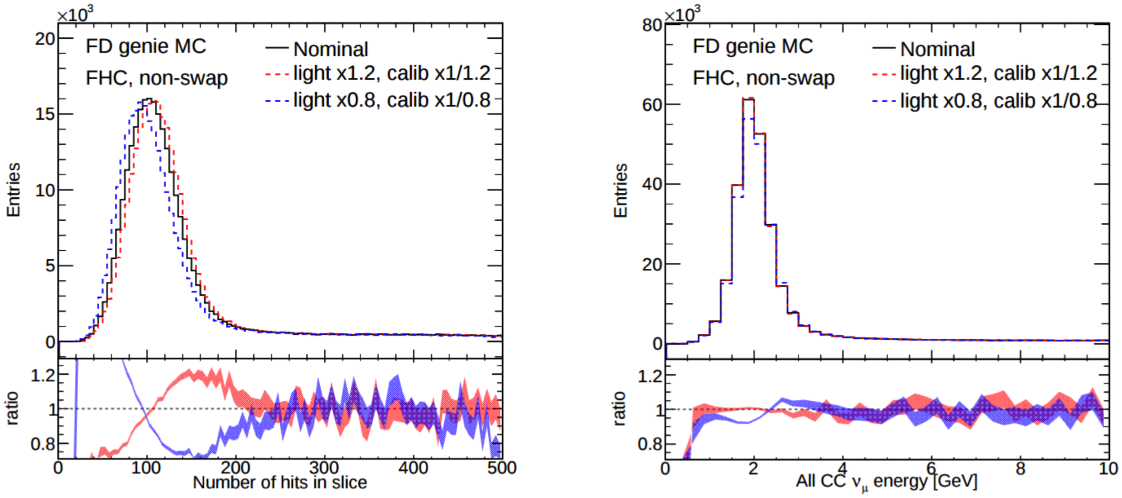

FIG. 8.6: Comparison between nominal FD MC (black) and light-level shifted up/down (red/blue) by 20% for number of hits in slice (*Left*) and reconstructed energy of ν_μ CC events (*Right*) distribution [23].

cross section, which is shifted by 2 sigma). Below are plots showing the 2 sigma event weights distribution in logarithmic scale to better show the size of the effects.

- Cross-section uncertainties
  - Adjust the axial mass in the CC and NC quasi-elastic cross section by +20%/ − 15%. Figure 8.7 shows the event weights of a 2 sigma shift up/down in ND MC. This particular systematic error was calculated with 2 sigma shift to cover the unsimulated scattering off substructure in the nucleus.
  - Adjust the axial mass in the elastic scattering cross section by ±25%. Figure 8.8 shows the event weights of a 2 sigma shift up/down in ND MC.
  - Adjust the η production in the elastic scattering cross section by ±30%. Figure 8.9 shows the event weights of a 2 sigma shift up/down in ND MC.

- Adjust the axial mass parameter in the Rein-Sehgal resonance cross section model by ±20%. Figure 8.11 (NC) and 8.12 (CC) show the event weights of a 2 sigma shift up/down in ND MC.
- Adjust the vector mass parameter in the Rein-Sehgal resonance cross section model by ±10%. Figure 8.13 (NC) and 8.14 (CC) show the event weights of a 2 sigma shift up/down in ND MC.
- Adjust the rate of single pion production in CC and NC for non-resonant inelastic events by ±50%, tweaking 8 correlated production channels including both CC and NC. Figure 8.15 and 8.16 show the event weights of a 2 sigma shift up/down for two of the eight knobs in ND MC.
- Adjust the rate of two-pion production in CC and NC for non-resonant inelastic events by ±50%, tweaking 8 correlated production channels including both CC and NC. Figure 8.17 and 8.18 show the event weights of a 2 sigma shift up/down for two of the eight knobs in ND MC.
- Adjust the A_{HT} parameter in the Bodek-Yang model by ±50%. Figure 8.19 shows the event weights of a 2 sigma shift up/down in ND MC.
- Adjust the B_{HT} parameter in the Bodek-Yang model by ±25%. Figure 8.20 shows the event weights of a 2 sigma shift up/down in ND MC.
- Adjust the C_{V1u} parameter in the Bodek-Yang model by ±30%. Figure 8.21 shows the event weights of a 2 sigma shift up/down in ND MC.
- Adjust the C_{V2u} parameter in the Bodek-Yang model by ±40%. Figure 8.22 shows

the event weights of a 2 sigma shift up/down in ND MC.

- Modify the Pauli blocking momentum cutoff at low Q^2 by ±30%. Figure 8.10 shows the event weights of a 2 sigma shift up/down in ND MC.

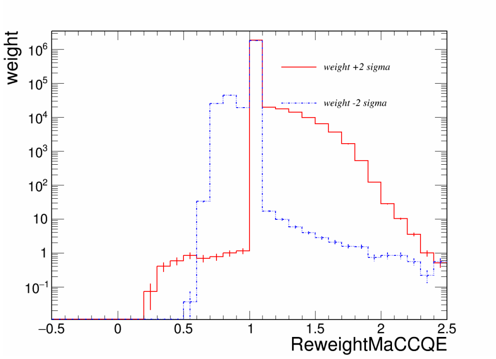

FIG. 8.7: Event weights of a 2 sigma shift up/down of the axial mass in the CC and NC quasi-elastic cross section in ND MC

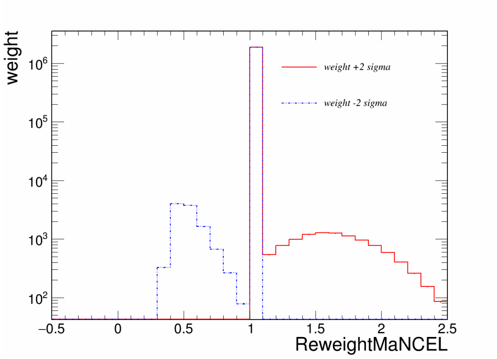

FIG. 8.8: Event weights of a 2 sigma shift up/down of the axial mass in the elastic scattering cross section in ND MC

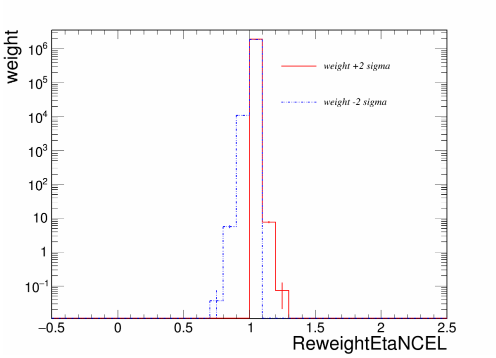

FIG. 8.9: Event weights of a 2 sigma shift up/down of the η production in the elastic scattering cross section in ND MC

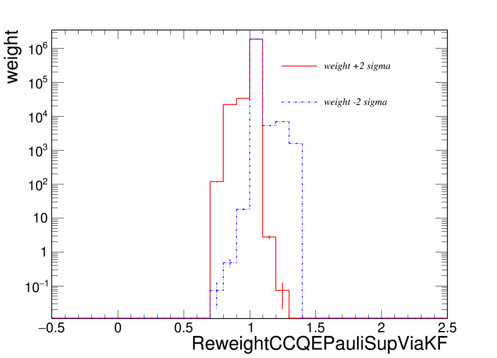

FIG. 8.10: Event weights of a 2 sigma shift up/down of the Pauli blocking momentum cutoff at low Q^2 in ND MC

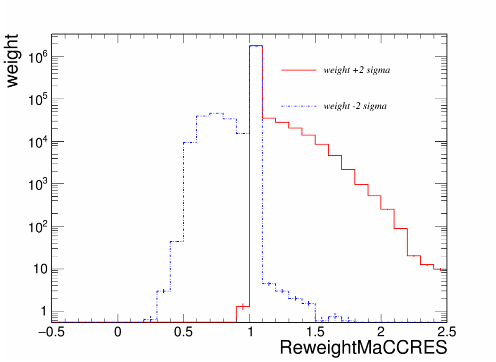

FIG. 8.11: Event weights of a 2 sigma shift up/down of the axial mass parameter in the Rein-Sehgal resonance cross section model for CC event in ND MC

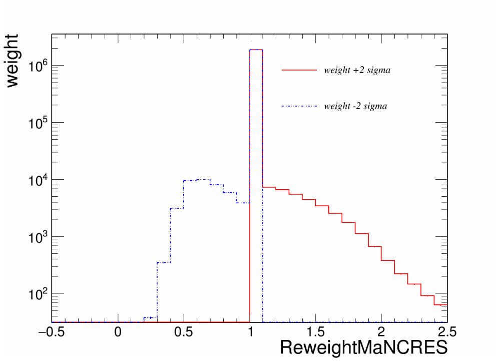

FIG. 8.12: Event weights of a 2 sigma shift up/down of the axial mass parameter in the Rein-Sehgal resonance cross section model for NC event in ND MC

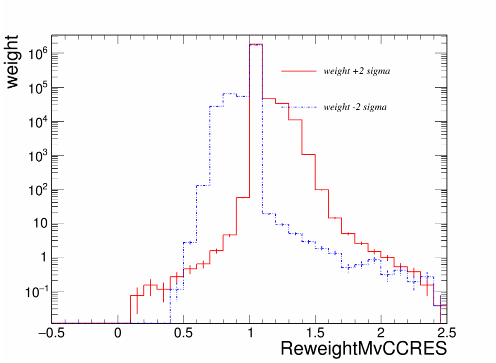

FIG. 8.13: Event weights of a 2 sigma shift up/down of the vector mass parameter in the Rein-Sehgal resonance cross section model for CC event in ND MC

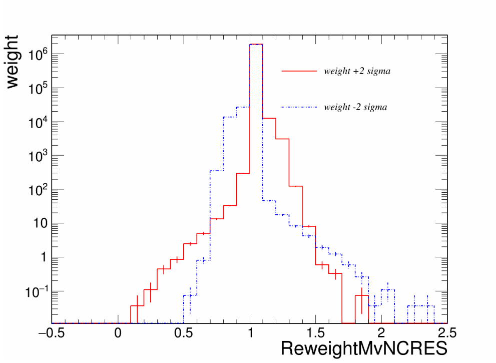

FIG. 8.14: Event weights of a 2 sigma shift up/down of the vector mass parameter in the Rein-Sehgal resonance cross section model for CC event in ND MC

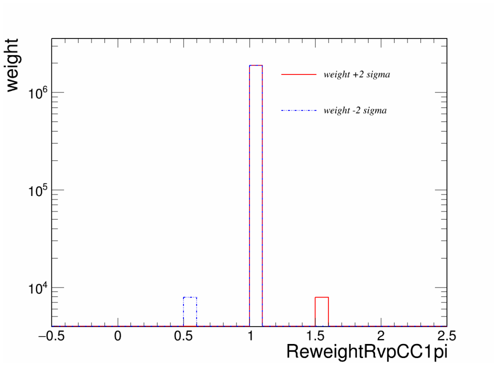

FIG. 8.15: Event weights of a 2 sigma shift up/down of the rate of single pion production in CC and NC for non-resonant inelastic scattering off proton in ND MC

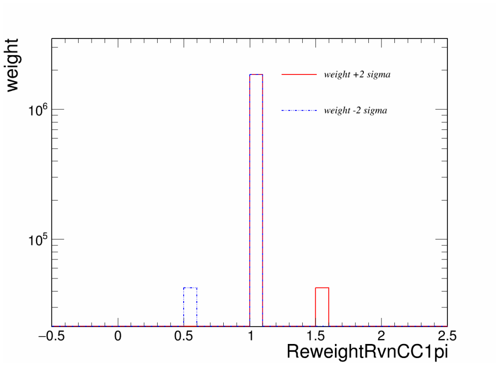

FIG. 8.16: Event weights of a 2 sigma shift up/down of the rate of single pion production in CC and NC for non-resonant inelastic scattering off nucleon in ND MC

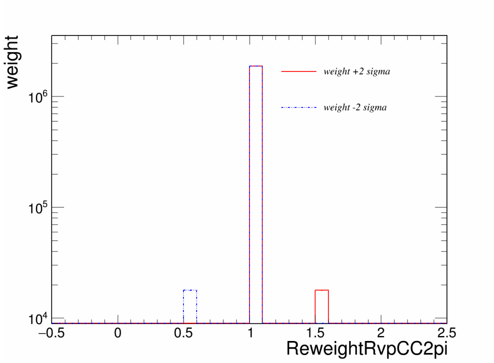

FIG. 8.17: Event weights of a 2 sigma shift up/down of the rate of two pion production in CC and NC for non-resonant inelastic scattering off proton in ND MC

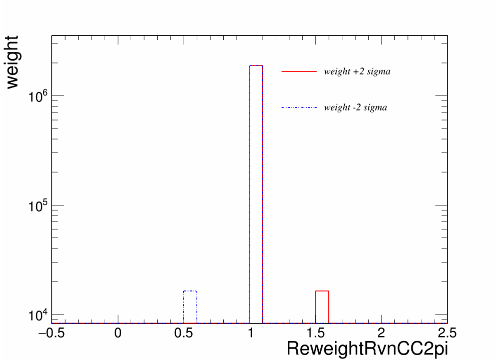

FIG. 8.18: Event weights of a 2 sigma shift up/down of the rate of two pion production in CC and NC for non-resonant inelastic scattering off nucleon in ND MC

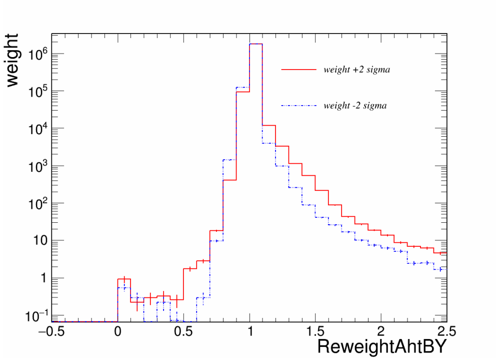

FIG. 8.19: Event weights of a 2 sigma shift up/down of the A_{HT} parameter in the Bodek-Yang mode in ND MC

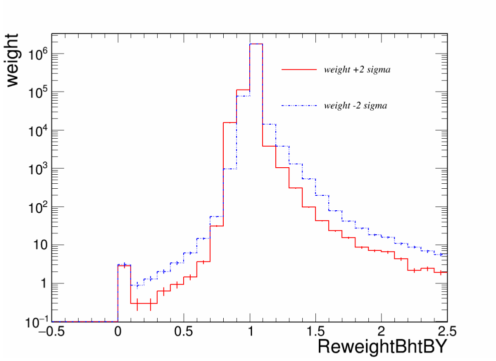

FIG. 8.20: Event weights of a 2 sigma shift up/down of the B_{HT} parameter in the Bodek-Yang mode in ND MC

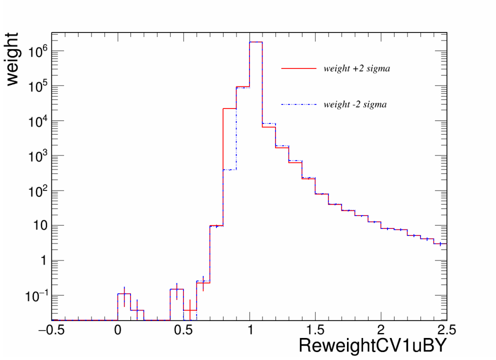

FIG. 8.21: Event weights of a 2 sigma shift up/down of the C_{V1u} parameter in the Bodek-Yang mode in ND MC

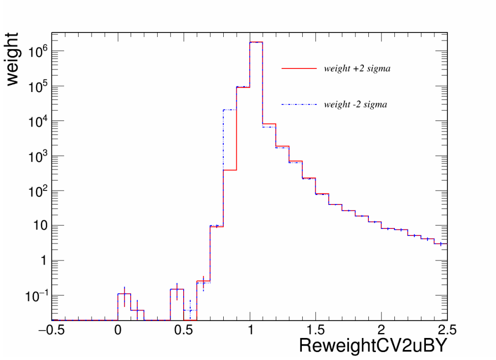

FIG. 8.22: Event weights of a 2 sigma shift up/down of the C_{V2u} parameter in the Bodek-Yang mode in ND MC

- Hadronization model uncertainties

  The Hadronization model determines the final state particles and 4-momenta produced in a nuetrino-nucleon interaction given its interaction type and event kinematics. In GENIE, the default hadronization model is called AGKY model, which uses Koba-Nielsen-Olesen (KNO) model in low invariant mass region and gradually transitions to PYTHIA/JETSET model in higher masses [18]. The systematic effects considered are:

  - Adjust the x_F distribution for low multiplicity DIS events produced by the AGKY model by ±20%. Figure 8.23 shows the event weights of a 2 sigma shift up/down.
  - Adjust the p_T distribution for low multiplicity DIS events produced by the AGKY model by ±3%. Figure 8.24 shows the event weights of a 2 sigma shift up/down.
  - Adjust the resonance decay branching ratio to photons by ±50%. Figure 8.25 shows the event weights of a 2 sigma shift up/down.
  - Adjust the resonance decay branching ratio to eta mesons by ±50%. Figure 8.26 shows the event weights of a 2 sigma shift up/down.
  - Adjust the delta decay angle distribution. Figure 8.27 shows the event weights of a 2 sigma shift up/down.

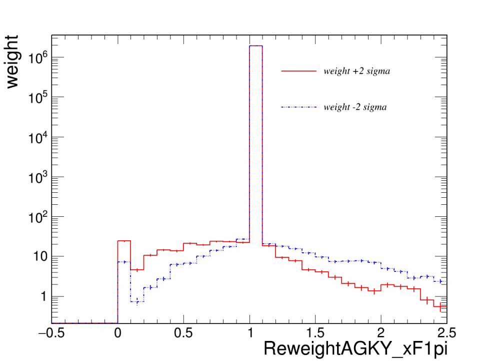

FIG. 8.23: Event weights of a 2 sigma shift up/down of the x_F distribution for low multiplicity DIS events produced by the AGKY model in ND MC.

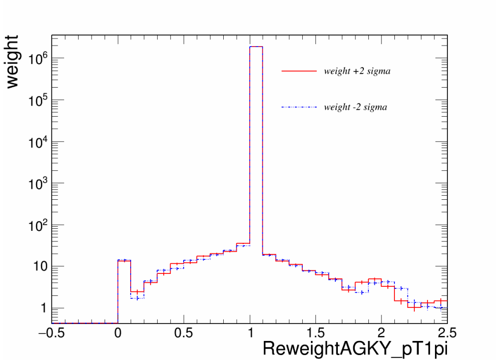

FIG. 8.24: Event weights of a 2 sigma shift up/down of the p_T distribution for low multiplicity DIS events produced by the AGKY model in ND MC.

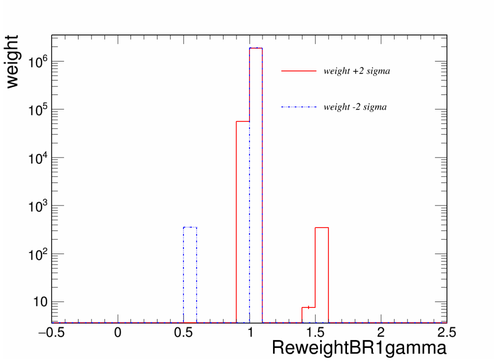

FIG. 8.25: Event weights of a 2 sigma shift up/down of the resonance decay branching ratio to photons in ND MC.

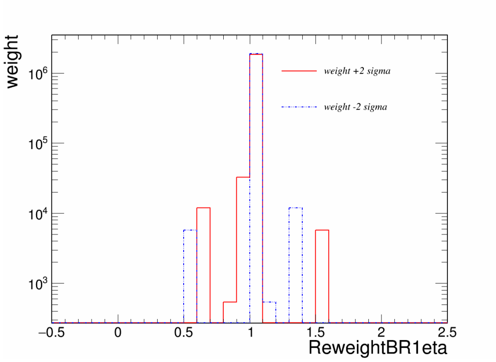

FIG. 8.26: Event weights of a 2 sigma shift up/down of the resonance decay branching ratio to etas in ND MC.

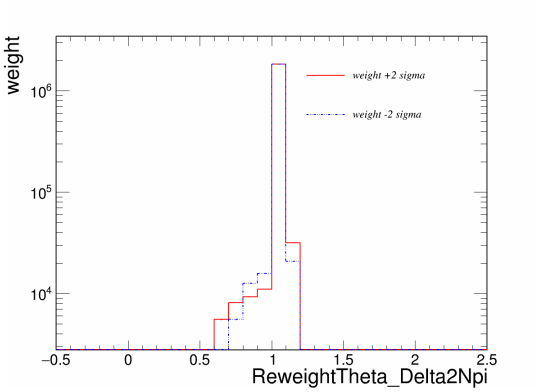

FIG. 8.27: Event weights of a 2 sigma shift up/down of the delta decay angle distribution in ND MC.

- Final State Interactions

  Final State Interactions (FSI) accounts for the effects of the produced hadrons traveling through the nucleon medium before they are detected. Thirteen knobs are provided by GENIE to tweak the production probability of a specific final state as listed below:

  - Adjust the pion mean free path by ±20%. Figure 8.28 shows the event weights of 2 sigma shift up/down.
  - Adjust the nucleon mean free path by ±20%. Figure 8.29 shows the event weights of 2 sigma shift up/down.
  - Adjust the absorption probability for pions by ±30%. Figure 8.30 shows the event weights of 2 sigma shift up/down.
  - Adjust the absorption probability for nucleons by ±20%. Figure 8.31 shows the event weights of 2 sigma shift up/down.
  - Adjust the charge-exchange probability for pions by ±50%. Figure 8.32 shows the event weights of 2 sigma shift up/down.
  - Adjust the charge-exchange probability for nucleons by ±50%. Figure 8.33 shows the event weights of 2 sigma shift up/down.
  - Adjust the elastic-scattering probability for pions by ±10%. Figure 8.34 shows the event weights of 2 sigma shift up/down.
  - Adjust the elastic-scattering probability for nucleons by ±30%. Figure 8.35 shows the event weights of 2 sigma shift up/down.

- Adjust the inelastic-scattering probability for pions by ±40%. Figure 8.36 shows the event weights of 2 sigma shift up/down.
- Adjust the inelastic-scattering probability for nucleons by ±40%. Figure 8.37 shows the event weights of 2 sigma shift up/down.
- Adjust the pion production probability for pions by ±20%. Figure 8.38 shows the event weights of 2 sigma shift up/down.
- Adjust the pion production probability for nucleons by ±20%. Figure 8.39 shows the event weights of 2 sigma shift up/down.

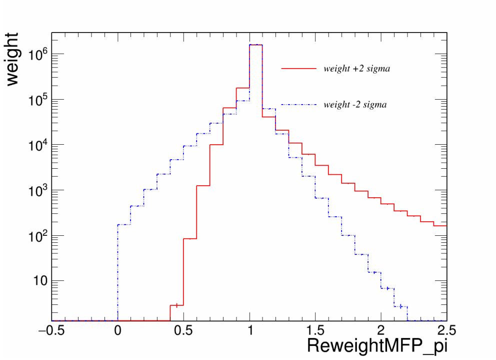

FIG. 8.28: Event weights of a 2 sigma shift up/down of the pion mean free path in ND MC.

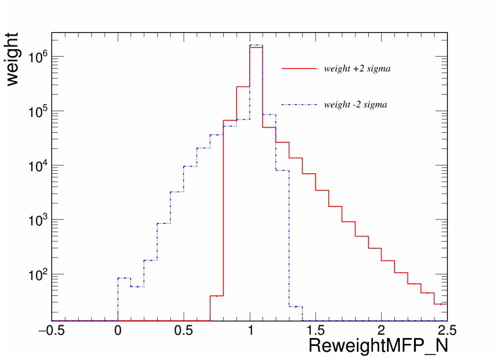

FIG. 8.29: Event weights of a 2 sigma shift up/down of the nucleon mean free path in ND MC.

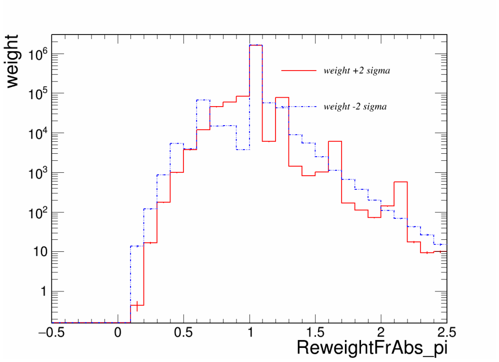

FIG. 8.30: Event weights of a 2 sigma shift up/down of the absorption probability for pions in ND MC.

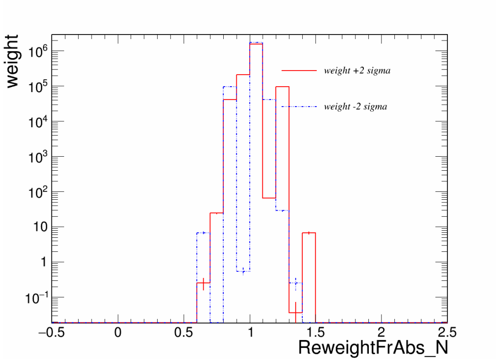

FIG. 8.31: Event weights of a 2 sigma shift up/down of the absorption probability for nucleons in ND MC.

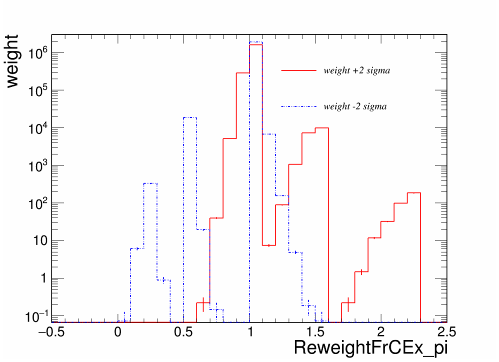

FIG. 8.32: Event weights of a 2 sigma shift up/down of the charge exchange probability for pions in ND MC.

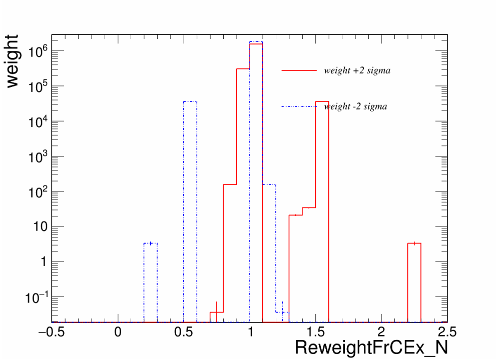

FIG. 8.33: Event weights of a 2 sigma shift up/down of the charge exchange probability for nucleons in ND MC.

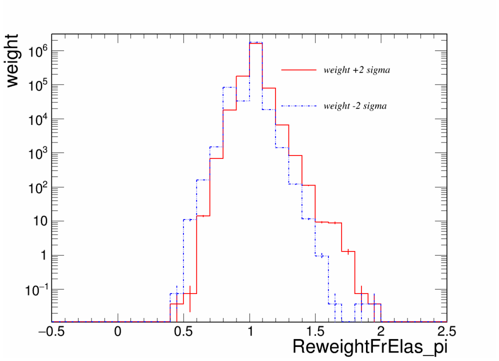

FIG. 8.34: Event weights of a 2 sigma shift up/down of the elastic scattering probability for pions in ND MC.

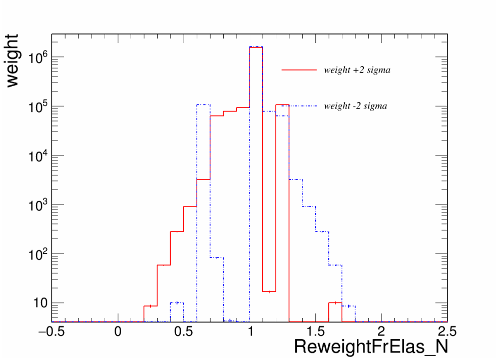

FIG. 8.35: Event weights of a 2 sigma shift up/down of the elastic scattering probability for nucleons in ND MC.

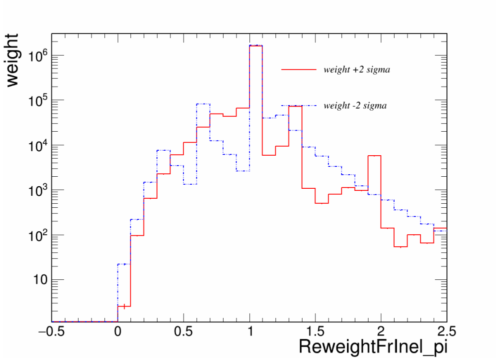

FIG. 8.36: Event weights of a 2 sigma shift up/down of the inelastic scattering probability for pions in ND MC.

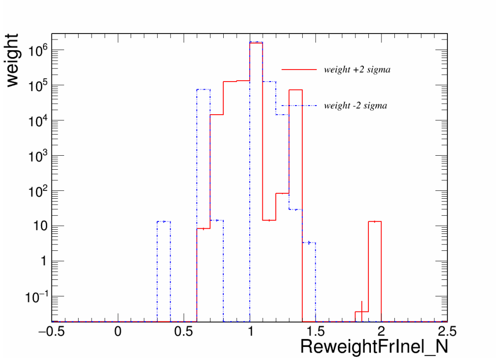

FIG. 8.37: Event weights of a 2 sigma shift up/down of the inelastic scattering probability for nucleons in ND MC.

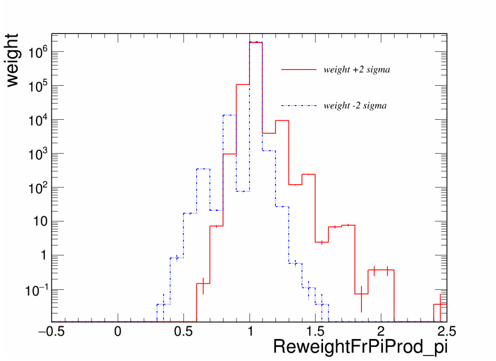

FIG. 8.38: Event weights of a 2 sigma shift up/down of the pion production probability for pions in ND MC.

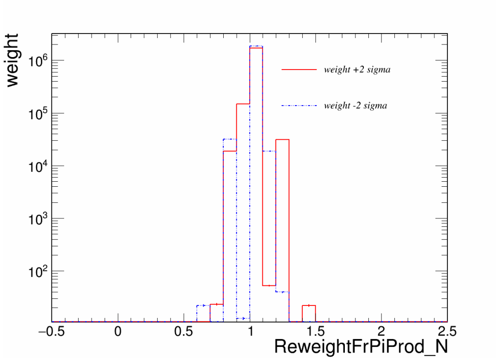

FIG. 8.39: Event weights of a 2 sigma shift up/down of the pion production probability for nucleons in ND MC.

Similar to the calibration systematics study, the systematically reweighted MC sample are then used in the extrapolation to calculate the percentage effect in the predicted FD event counts. The complete systematic errors on the GENIE reweighted variables, for LEM and LID, are tabulated in Table 8.4. Based on the table, the largest source of error in the signal comes from changes to the axial mass in quasi-elastic (QE) events and no single effect dominates the background systematic. The uncertainty of neutrino interaction is calculated by summing up these errors in quadrature, which is 13.98% for signal and 3.72% for total background in LID. In LEM, we have 12.01% for signal and 5.74% for total background.

GENIE reweight	LID		LEM	
	Signal	Background	Signal	Background
Nominal	0.00%	0.00%	0.00%	0.00%
01_MaccQE	13.19%	3.46%	11.19%	3.47%
CohPiZero	0.00%	0.00%	0.00%	0.65%
04_AhtBY	0.07%	0.33%	0.07%	0.38%
05_BhtBY	0.09%	0.36%	0.09%	0.42%
06_CV1uBYshape	0.00%	0.00%	0.00%	0.00%
07_CV2uBYshape	0.00%	0.00%	0.00%	0.00%
08_AGKY_xF1pi	0.02%	0.02%	0.02%	0.03%
09_AGKY_pT1pi	0.01%	0.04%	0.00%	0.02%
10_MFP_pi	0.75%	0.04%	0.65%	0.16%
11_MFP_N	0.07%	0.44%	0.15%	0.14%
12_FrCEx_pi	0.04%	0.24%	0.07%	0.38%
13_FrElas_pi	0.04%	0.25%	0.02%	0.01%
14_FrInel_pi	0.13%	0.46%	0.03%	0.70%
15_FrAbs_pi	0.20%	0.32%	0.07%	0.09%
16_FrPiProd_pi	0.00%	0.00%	0.01%	0.04%
17_FrCEx_N	0.02%	0.24%	0.06%	0.19%
18_FrElas_N	0.03%	0.31%	0.13%	0.15%
19_FrInel_N	0.03%	0.11%	0.08%	0.15%
20_FrAbs_N	0.08%	0.08%	0.01%	0.01%
21_FrPiProd_N	0.01%	0.05%	0.02%	0.05%
22_CCQEPauliSupViaKF	0.17%	0.00%	0.29%	0.40%
23_CCQEMomDistroFGtoSF	0.00%	0.00%	0.00%	0.00%
24_BR1gamma	0.00%	0.00%	0.00%	0.01%
25_BR1eta	0.20%	0.04%	0.24%	0.11%
26_Theta_Delta2Npi	0.17%	0.03%	0.18%	0.02%
27_MaRES	1.09%	0.77%	0.83%	1.07%
28_MvRES	0.33%	0.45%	0.26%	0.25%
29_MaNCEL	0.02%	0.06%	0.03%	0.01%
30_EtaNCEL	0.00%	0.00%	0.00%	0.00%
35_allpi	4.41%	0.07%	4.20%	3.87%
Total	13.98%	3.72%	12.01%	5.47%

TABLE 8.4: Percentage uncertainties for neutrino interaction systematics for each GENIE reweight knob and the quadrature total.

Diff %	total bkg.	ν_μ CC	beam ν_e CC	NC	ν_τ CC
LID $100 < v_Z < 400$ cm	-2.59	-1.54	-2.01	-3.66	0
LID $400 < v_Z < 700$ cm	1.63	3.08	2.01	0.98	0
LID $0 < v_X < 140$ cm	-2.69	-3.08	-2.75	-2.93	0
LID $-140 < v_X < 0$ cm	2.11	4.62	3.11	0.49	0
LID $0 < v_Y < 140$ cm	-1.92	0	-0.92	-3.66	0
LID $-140 < v_Y < 0$ cm	0.58	1.54	0.55	0.49	0
LID $\lvert v_X, v_Y\rvert < 99cm$ cm	-1.92	-1.54	-1.83	-2.20	0
LID $99 < \lvert v_X, v_Y\rvert < 140cm$	1.25	3.08	2.01	0	0
LEM $100 < v_Z < 400$ cm	-2.58	-1.09	-2.15	-3.65	0
LEM $400 < v_Z < 700$ cm	0.86	2.17	2.15	-1.01	0
LEM $0 < v_X < 140$ cm	-2.32	-1.09	-1.08	-4.26	0
LEM $-140 < v_X < 0$ cm	0.77	1.09	1.25	0.20	0
LEM $0 < v_Y < 140$ cm	-1.46	-1.09	0	-3.45	0
LEM $-140 < v_Y < 0$ cm	0.43	1.09	0	-1.42	0
LEM $\lvert v_X, v_Y\rvert < 99cm$ cm	-1.89	0	-1.61	-2.84	0
LEM $99 < \lvert v_X, v_y\rvert < 140cm$	0.43	1.09	1.97	-1.42	0
LID Absolute Average Error	1.84%	2.31%	1.90%	1.80%	0%
LEM Absolute Average Error	1.34%	1.09%	1.28%	2.28%	0%

TABLE 8.5: Percentage difference of Far Detector predicted events rate for LID and LEM selection to study the effect of containment. Eight sets of extrapolation is performed separately different geographic regions of the Near Detector.

8.6 Containment

Because the size of the Near detector is not comparable to the Far detector, selection across the Near detector could be less uniform than in the Far detector. To study this effect, we divided the ND sample into eight sets by cutting each of the three detector axes in half. Then eight sets of extrapolations are performed separately using each region to predict the FD event rate. Table 8.5 shows the predicted background results with each particle selector. The absolute uncertainties for the ND containment is calculated by taking the absolute average for all regions, which is 1.84% for LID and 1.34% for LEM.

8.7 Rock Contamination

The NOνA Near detector is located underground and surrounded by rock. Thus neutrino interaction occuring in the rock is one of the background sources for the ND. The rock events are simulated separately, stored in a library and overlaid with the ND in-detector MC later. To increase the statistics despite heavy computing demands in the generation, each simulated rock event is re-used ~ 350 times. This could potentially bring in systematic uncertainty because one rock event that happens to pass the ν_e selection would be re-selected many times. To study this effect, we used an MC sample that has the rock events removed by truth. Figure 8.40 shows the vertex Z position distribution compared between ND data, MC without rock events, and true rock events after reconstruction quality cuts (left) and LID selection (right). After only the reconstruction cut, the discrepancy between data and MC is big, especially in the front of the detector. The rock event rate is higher in MC than data. However, after the full ν_e selection cuts, the differences are mostly flattened out [101]. We then further quantified the systematic error using this no-rock-event MC sample in extrapolation to make the FD prediction. Percentage differences compared to the nominal are shown in Table 8.6. Overall this rock event contamination effects is only a 0.10% systematic error for background using LID selector, and 0.09% with LEM selector.

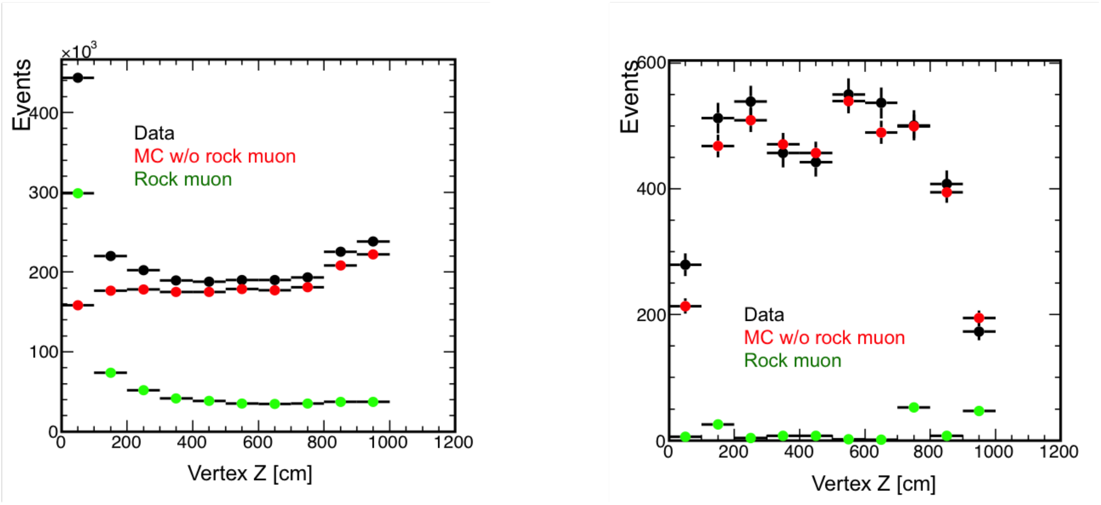

a Reco Quality

b LID

FIG. 8.40: Vertex Z distribution for ND data (black), MC without rock muon (red) and truth rock muon events (green) after reconstruction quality cuts (left) and LID selection (right).

Diff %	total bkg.	ν_μ CC	beam ν_e CC	NC	ν_τ CC
LID Extrapolated prediction without rock	0.10	1.54	0.55	-0.49	0
LEM Extrapolated prediction without rock	0.09	1.09	0.72	-1.01	0

TABLE 8.6: Percentage difference of the extrapolated prediction of FD events using ND MC without rock neutrino interactions compared to nominal for both LID and LEM selection.

8.8 Decomposition

In Section 7.3, we described in detail the process to proportionally decompose ND data into different neutrino interaction types based on MC. That procedure assumes the simulation correctly predicts the relative percentage of each component. To estimate how wrong that assumption is, we took the difference between data and MC and assigned them entirely to each component ($\nu_e CC$, $\nu_\mu CC$, or NC) alternatively to make a shifted FD extrapolation. The predicted FD event rates are compared to nominal as shown in

Diff %	total bkg.	ν_μ CC	beam ν_e CC	NC	ν_τ CC
LID ν_e decomposition	0.77	-4.62	6.41	-5.61	0
LID NC decomposition	0.86	-4.62	-6.23	11.46	0
LID ν_μ decomposition	-3.94	26.15	-6.23	-5.61	0
LEM ν_e decomposition	2.41	-4.35	10.22	-5.27	0
LEM NC decomposition	1.03	-4.35	-4.66	8.52	0
LEM ν_μ decomposition	-3.53	10.87	-4.66	-5.27	0

TABLE 8.7: Percentage difference compared to nominal of FD extrapolated prediction events in each component for LID and LEM selection. Where the difference between data and MC are assigned entirely to each component (ν_eCC, $\nu_\mu CC$, or NC) alternatively to make a shifted FD extrapolation.

Table 8.7. The biggest error occurs when we assign all data/mc deficit to the $\nu_\mu CC$ component, which is 3.94% for LID selection and 3.53% for LEM selection. This is used as the final uncertainty for the decomposition process.

8.9 Alignment

The NOνA Monte Carlo assumes all the planes in both detectors are perfectly aligned with respect to the baseline. However, this is not necessarily true in the real world due to construction imperfections and extrusion distortion. This minor mis-alignment could bring in a systematic error by changing the event topology thus affecting the reconstruction and particle identification. Table 8.8 lists the systematic error as percentage difference between the nominal MC and mis-aligned MC extrapolation. For both PID selection methods, the effect is at the sub-percent level, which can be neglected.

Diff %	signal	total bkg.	ν_μ CC	beam ν_e CC	NC	ν_τ CC
LID extrapolation	-0.73	-1.73	-1.54	-1.83	-1.95	0
LEM extrapolation	-0.73	-1.55	-1.09	-1.43	-1.83	0

TABLE 8.8: Percentage difference of the Far detector extrapolated event prediction for LID and LEM selection using the mis-aligned geometry MC sample.

LEM				
Channel	FD MC	ND Data	ND MC	Total (%)
beam ν_e	3.88	1.97	0.82	4.43
ν_μ	4.91	1.88	0.79	5.31
NC	1.89	1.76	0.74	2.69
Total	2.07	1.79	0.75	2.85
LID				
Channel	FD MC	ND Data	ND MC	Total (%)
beam ν_e	3.98	2.46	1.04	4.81
ν_μ	6.19	2.50	1.05	6.76
NC	2.07	2.48	1.05	3.40
Total	2.27	2.40	1.01	3.47

TABLE 8.9: Statistical error on extrapolation of background components.

8.10 Data and Monte Carlo Statistics

The sample size of Monte Carlo that we used in extrapolation is about 6 times to the data in ND and 2400 times in the FD. The resulting statistical uncertainty is taken as a systematic error and calculated using shifted MC. Table 8.9 shows the systematic error as percentage difference between nominal and shifted samples in each event type, which adds up to 3.47% for total backgrounds for LID and 2.85% for LEM.

8.11 Normalization

Normalization in NOνA is performed based on POT counting and effective detector mass. For POT counting, a 0.5% uncertainty is caused by possible drift of the beam monitoring device [102]. A 0.7% uncertainty for the effective detector mass comes from the measurement error of detector components [103]. Lastly, the Near detector data/MC discrepancy that we showed in Section 7.2 contributes 0.8% systematics uncertainty in reconstruction efficiency. By adding up these three effects in quadrature, the total normalization systematic uncertainty on both signal and background is 1.2%.

8.12 Summary

To summarize, the major categories of systematic uncertainties that we discussed in this chapter are listed in Table 8.10. The dominant source of systematic arise from calibration, neutrino interaction model and scintillation saturation uncertainties. By adding all the effects in quadrature, the total systematics error is 10.11% for the background and 17.58% for the signal using LID selection, while the number is 12.06% for the background and 14.99% for the signal with LEM selection.

	LID		LEM	
	Bkg. (%)	Signal (%)	Bkg. (%)	Signal (%)
Beam	3.18	1.06	2.85	1.04
Scintillation Saturation	5.14	7.22	4.62	7.94
Calibration	4.44	7.58	7.90	3.68
Light Level	-	1.00	-	1.00
Neutrino Interaction	3.72	13.98	5.47	12.01
Containment	1.84	-	1.34	-
Rock Contamination	0.10	-	0.09	-
Decomposition	3.90	-	3.50	-
Data & MC Stat.	3.47	0.6	2.85	0.6
Normalization	1.20	1.20	1.20	1.20
Total	10.11	17.58	12.06	14.99

TABLE 8.10: List of systematic uncertainties on the background and signal prediction for events selected by LID or LEM selector. The last row corresponds to the quadrature sum of all errors in the table.

CHAPTER 9

Results

This chapter reports the results of the first ν_e appearance analysis by the NOνA experiment. The whole analysis was developed blindly with the signal region of the FD data sealed completely to prevent any selection bias. The first section describes the sideband study that was performed to test the analysis chain before the signal region of the FD data was inspected. Then in the second section, the prediction results are tested against the signal region to present the major result of this study. In the end, the conclusion of this thesis is presented.

9.1 Sideband Study

As described in Chapter 7, the signal events are selected by the preselection cuts and one of the two PID cuts with $LID > 0.95$ or $LEM > 0.8$. With the signal region covered

	Signal	Beam Bkg.	Cosmic Bkg.	Total Prediction	Data
$0.7 < LID < 0.95$	2.33	1.5	0.38	4.21	5
$0.6 < LEM < 0.8$	1.79	1.02	0.08	2.89	2

TABLE 9.1: Comparison for the number of events between FD prediction and measurement for events passing the sideband low PID cut [4].

for the blind analysis, the way to test the analysis chain is using the sideband events, or those events that fall into the low PID regions that defined as $0.7 < LID < 0.95$ or $0.6 < LEM < 0.8$. By passing the sideband selected events through the extrapolation process, the FD prediction as shown in Table 9.1 was compared to the data. For LID (LEM), the total prediction is 4.21 (2.89) events, while in FD data 5 (2) events were observed in that region. This consistency demonstrated the reliability of the analysis chain.

9.2 NOνA ν_e Appearance Result

After confirming the FD prediction has good consistency with measurement in the sideband region, the signal region of the data is revealed for analysis. With the primary selector LID, 6 ν_e appearance candidates were selected, compared to the background prediction of $0.99 \pm 0.11(syst.)$. While for the secondary selector LEM, 11 events are selected and the background prediction is $1.07 \pm 0.14(syst.)$. All 6 of the LID candidates are also selected by LEM.

9.2.1 ν_e Appearance Candidates

The event displays of the 6 LID selected candidates are shown in Figures 9.4, 9.5 and 9.6. Each one of them (including the 5 additional ones from LEM selection) show convincing evidence of a ν_e CC event with a well-defined electromagnetic shower. A Kolmogorov-Smirnov statistic test is performed on the accumulation of the LID candidates as a function of exposure (as shown in Figure 9.1) and gives a 31% probability. This proves that the 6 event count of the observation is plausible given the exposure.

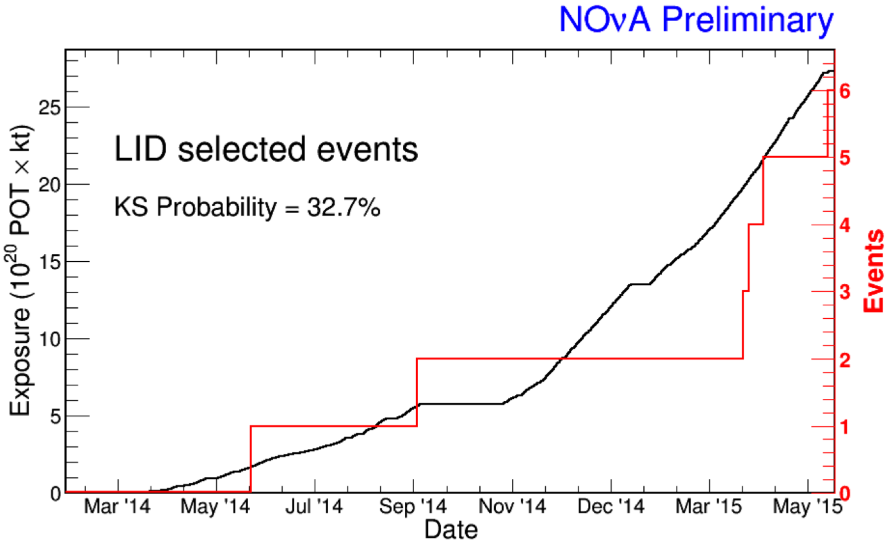

FIG. 9.1: FD NuMI beam POT exposure (black) and the ν_e appearance candidates accumulation (red) [24].

To further examine the results, several properties of the candidates are inspected. Figure 9.3 shows the LID distribution of all 11 candidates, where the 5 additional LEM selected events fall in the low PID sideband of LID, proving the consistency of the two PIDs. Figure 9.2 shows the timing distribution of the 6 LID ν_e appearance candidates inside the in-spill window marked by the blue lines, with two out of time events that set the scale of the cosmic ray background, which will be cut out by the timing cut. The second time window, $64\,\mu s$ delayed compare to the first one, is opened because of a known but rare failure of the TDU that caused a $64\,\mu s$ clocks offset after TDU reboots. This issue only existed in the early stage of the NOνA data, and no LID candidates are found in this second window. Further energy related properties of the 6 LID candidates are shown in Figure 9.7 including: calorimetric energy (a), cosine of the angle between the leading shower and beam direction (b), the number of slice hits (c), the number of planes (d), and the fraction of transverse momentum (e). Figure 9.8 shows the vertex distribution of the LID candidates in the XY (a), XZ (b) and YZ (c) views. All events are well contained and evenly spread inside the detector. Figure 9.9 and 9.10 shows the data/MC comparison for the likelihood of the leading shower of different event type hypotheses. Lastly, Figure 9.11 shows the data/MC comparison for the longitudinal and transverse energy deposition rate, dE/dx, of one of the events (run 15330). Overall, these distribution show no abnormal behavior compared to the prediction and confirm the candidates have typical electron shower topologies.

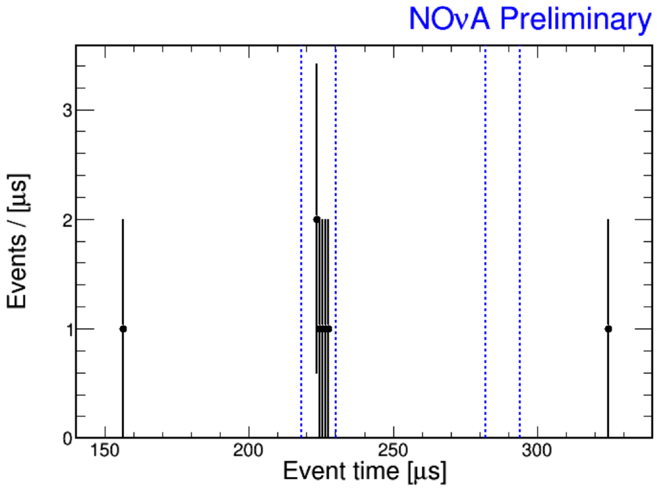

FIG. 9.2: Timing distribution of the ν_e appearance candidates inside the in-spill window (dash blue line). The two out-of-window events are cosmic background.

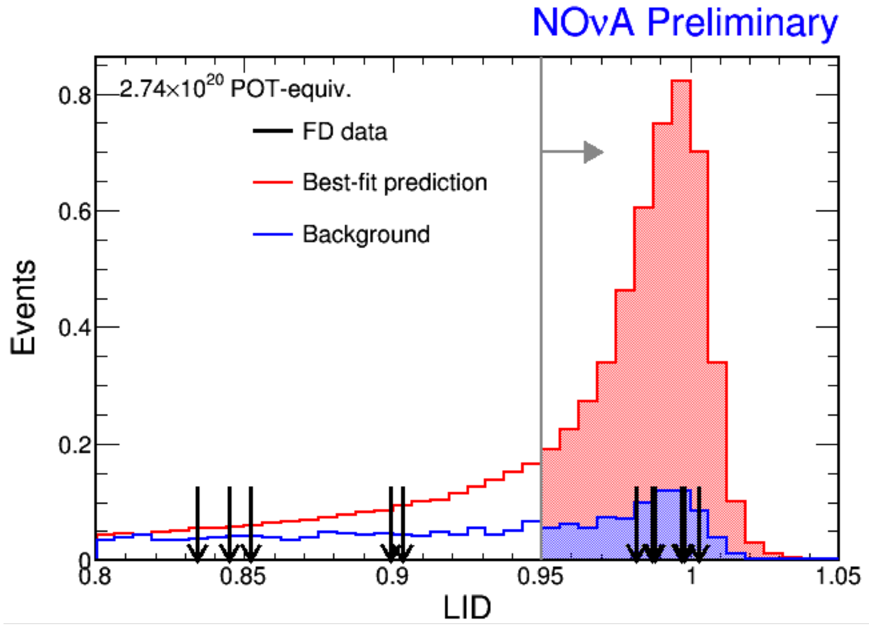

FIG. 9.3: LID distribution of the ν_e appearance candidates (black arrows) in the signal (shaded) and background (line) region.

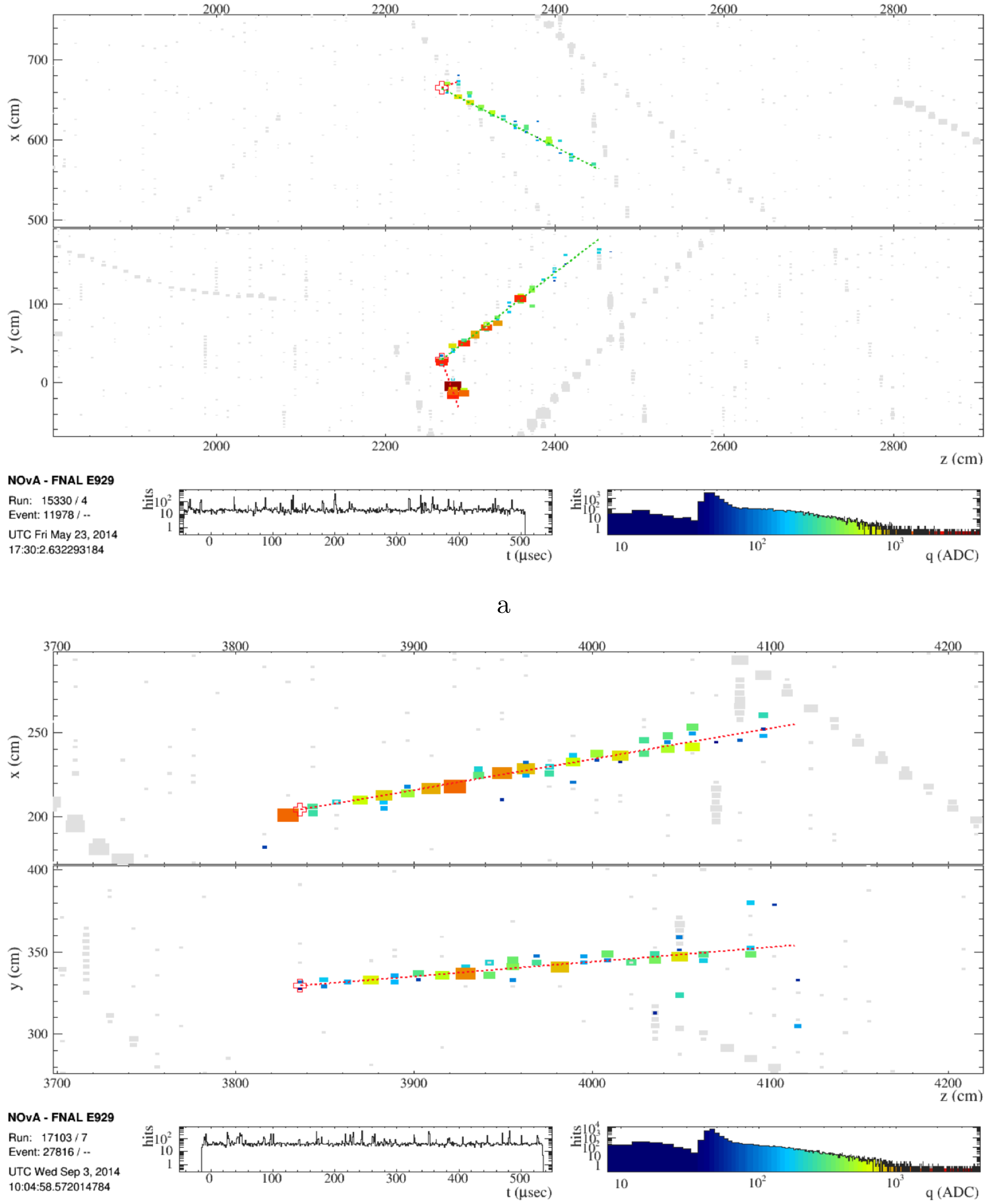

a

b

FIG. 9.4: FD NuMI beam data event display for the LID selected ν_e appearance candidates. The color of the boxes are scaled by the energy deposition in the cell, and gray hits represent out-of-time hits.

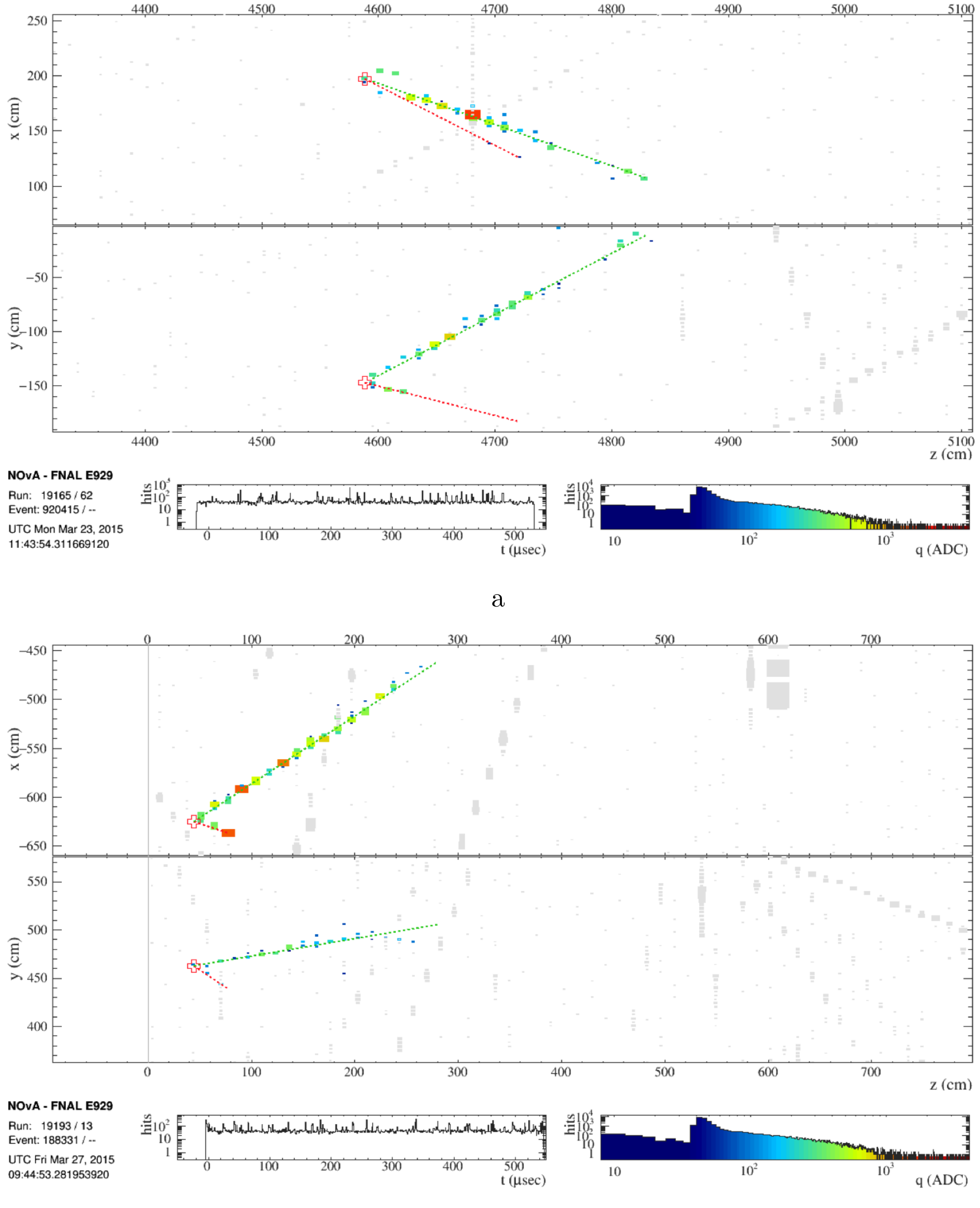

a

b

FIG. 9.5: FD NuMI beam data event display for the LID selected ν_e appearance candidates. The color of the boxes are scaled by the energy deposition in the cell, and gray hits represent out-of-time cosmics.

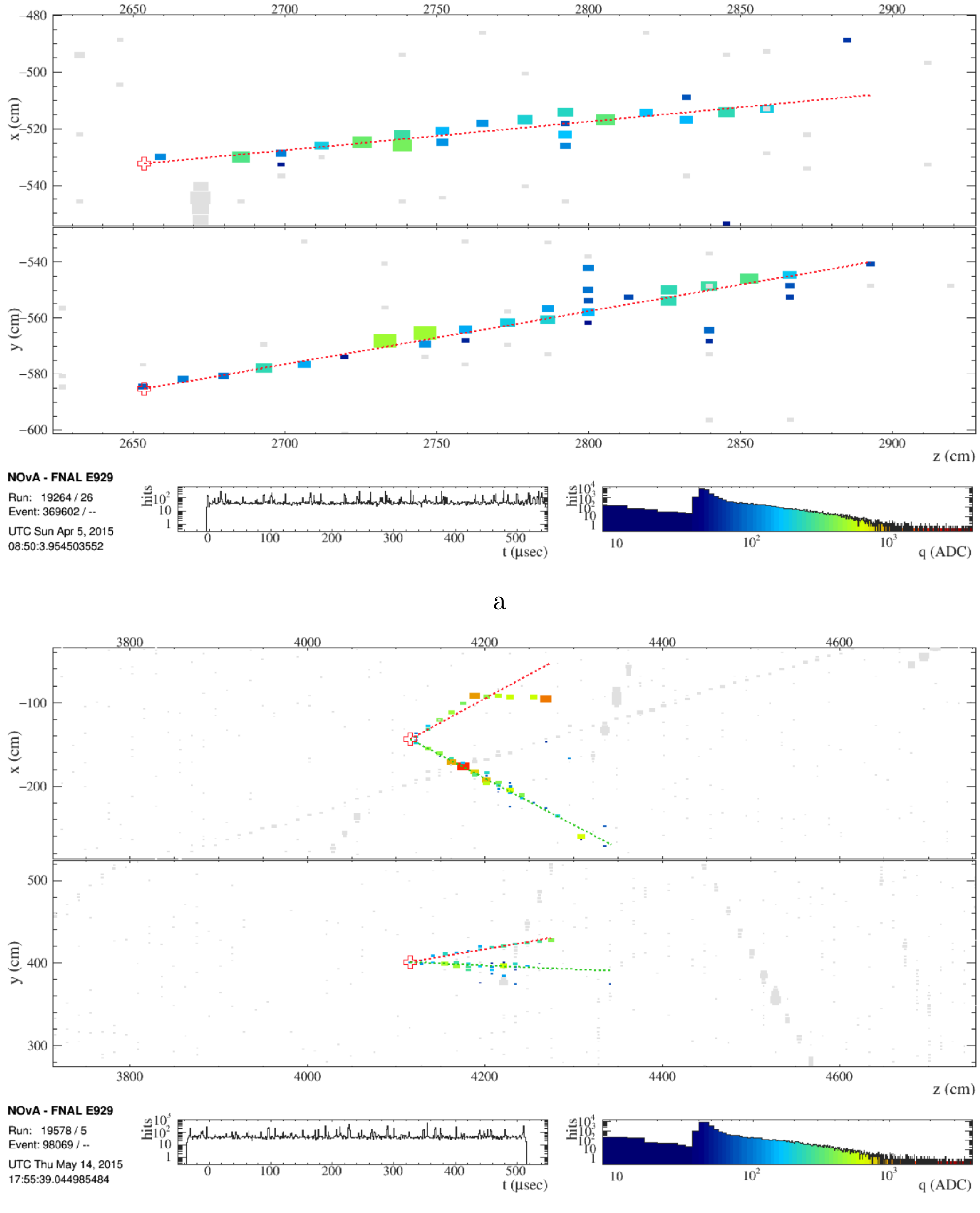

a

b

FIG. 9.6: FD NuMI beam data event display for the LID selected ν_e appearance candidates. The color of the boxes are scaled by the energy deposition in the cell, and gray hits represent out-of-time cosmics.

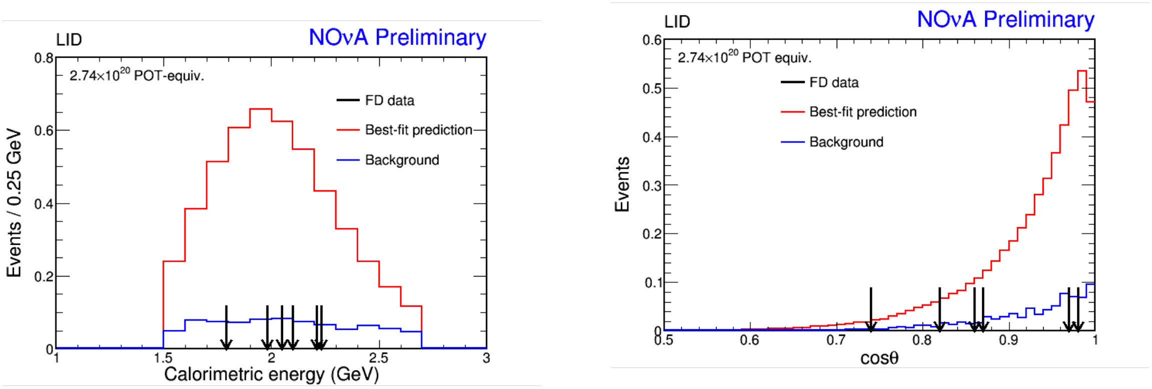

a Distribution of calorimetric energy.

b Distribution of cosine of the angle between the leading shower and beam direction.

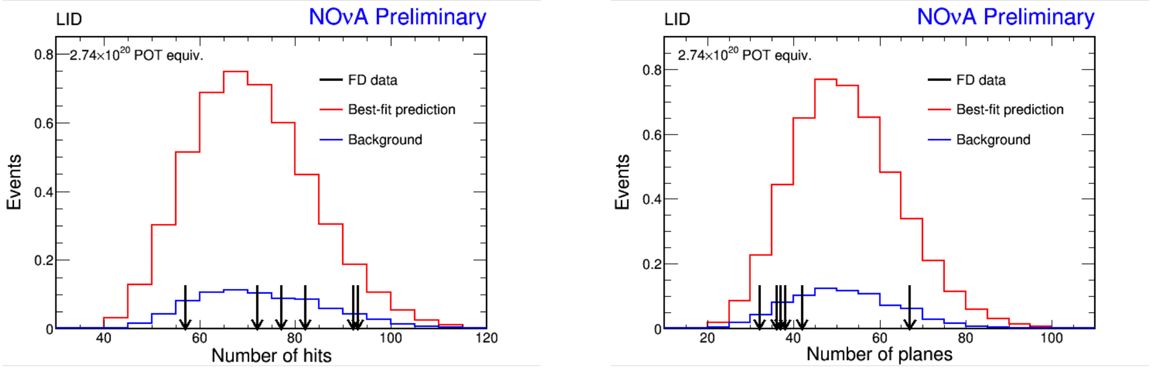

c Distribuition of the number of slice hits

d Distribuition of the number of planes

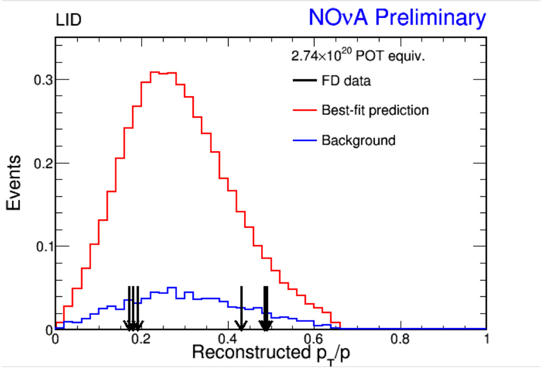

e Distribuition of the fraction of transverse momentum.

FIG. 9.7: Distributions of the LID ν_e appearance candidates (black arrows) in the FD data compared to the FD predictions for background (blue) and total signal(red).

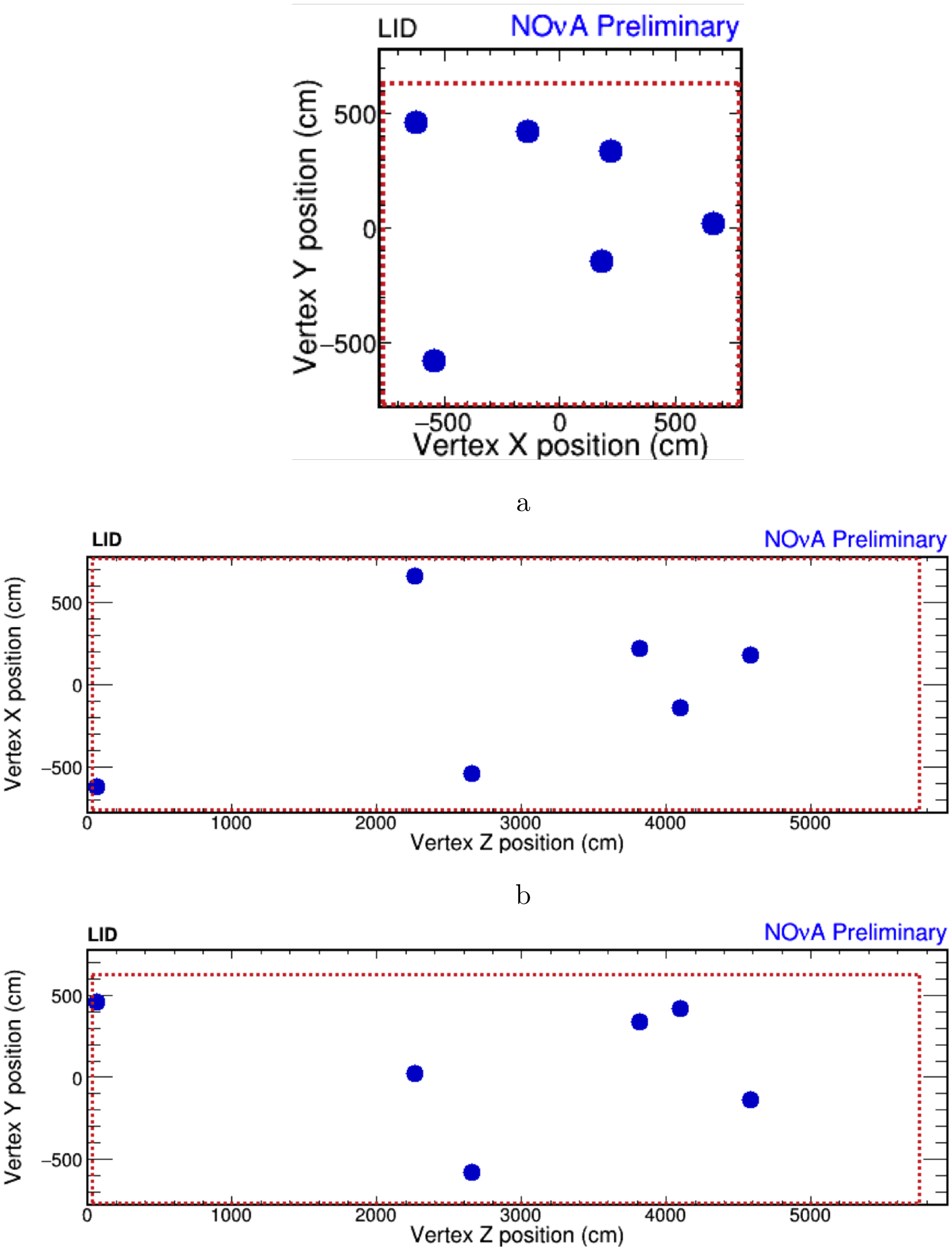

a

b

c

FIG. 9.8: Vertex distribution of the ν_e appearance candidates in XY (a), XZ (b) and YZ (c) planes. The dotted red lines defines the containment area in the detector.

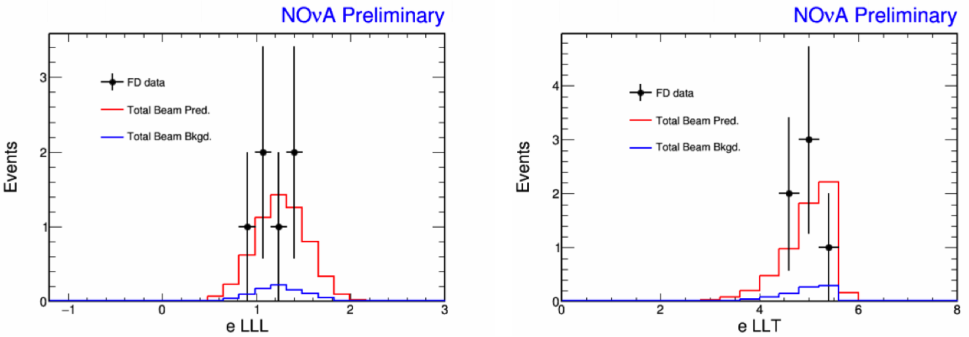

a Likelihood of the leading shower being an electron.

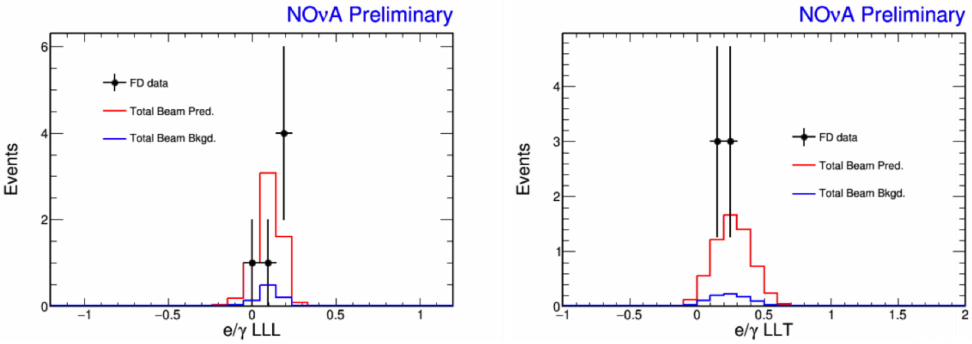

b Likelihood of the leading shower being an electron minus likelihood of being a photon.

FIG. 9.9: Likelihood of the leading shower for being a specific event hypotheses with comparison between data (black), MC prediction (red) and MC background (blue).

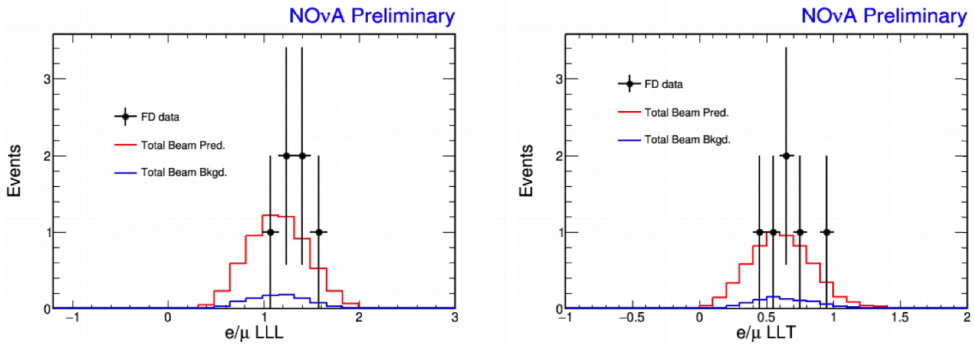

a Likelihood of the leading shower being an electron minus likelihood of being a muon.

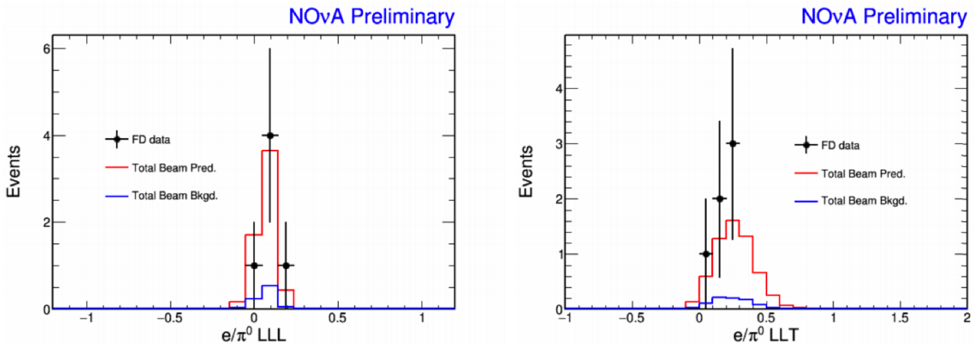

b Likelihood of the leading shower being an electron minus likelihood of being a pion.

FIG. 9.10: Likelihood of the leading shower for being a specific event hypotheses with comparison between data (black), MC prediction (red) and MC background (blue).

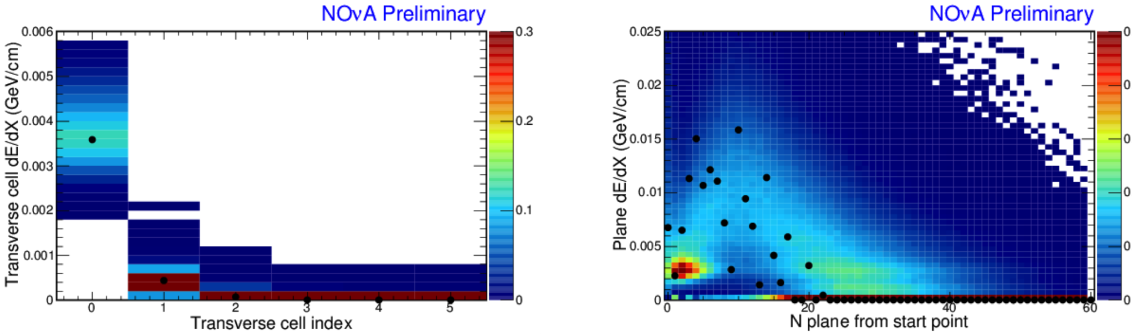

a Longitudinal

b Transverse

FIG. 9.11: Energy deposition rate dE/dx in longitudinal (left) and transverse (right) direction vs. cell number from shower core for the ν_e appearance candidate in run 15330. Black dots represent data and the colored box represent MC.

9.2.2 Confidence Interval

Because of the limited statistics, the first ν_e appearance analysis of NOνA is a "counting" analysis. This means only the number of candidates selected by the PID is used to infer the oscillation parameters, without any energy-related measurement taken into account.

To simply reject the the no-ν_e-oscillation ($\theta_{13} = 0$) hypothesis, the Poisson probability that a background of $0.99 \pm 0.11(syst.)$ could fluctuate to 6 events is computed using:

$$P = \sum_{x=6}^{\infty} \int_{-\infty}^{+\infty} \frac{b^x}{x! \sigma_b^2 b_0^2 \sqrt{2\pi}} exp(-b - \frac{(b-b_0)^2}{\sigma_b^2 b_0^2}) db \tag{9.1}$$

where b_0 is the expected background, and σ_b is the systematic error of the background. As a result, for the primary selector LID, the 6 events observation corresponds to a 3.3σ rejection of the no-ν_e-oscillations hypothesis. While for LEM, the rejection for its 11 events observation is 5.3σ.

To determine the preference of oscillation parameters (θ_{13}, δ_{cp} and mass hierarchy), a oscillation fit is performed in the two-dimensional space of $\sin^2 2\theta_{13}$ vs. δ_{cp}. Table 9.2 lists the value of the oscillation parameters we used in this analysis. The value of $\sin^2 2\theta_{13}$ comes from the best fit result of the reactor neutrino oscillation experiment Daya Bay [63] and will be used to compare with our fit result, the rest of the parameters are adopted from the current global best-fit value [2] used for oscillation calculation.

With the limited statistics of the first measurement, the confidence interval can not

Parameter	Value
Baseline	810 km
Matter density	$2.84\,gcm^{-3}$
$\sin^2\theta_{23}$	0.5
Δm^2_{32}	$+2.37\times10^{-3}\,eV^2$
$\sin^2 2\theta_{12}$	0.846
Δm^2_{21}	$7.53\times10^{-5}\,eV^2$
$\sin^2 2\theta_{13}$	0.086
δ_{cp}	0

TABLE 9.2: Summary of oscillation parameters used (for normal hierarchy assumption) in the first ν_e appearance analysis of NOνA.

be correctly calculated by the traditional standard χ^2 distribution. Instead, the Feldman-Cousins (F-C) procedure [104] is utilized to determine the confidence intervals by inspecting the range of likelihood ratios observed in pseudo-experiments. To be more specific, F-C introduces an alternative way of calculating the likelihood ratio: $R = \frac{P(x|\mu_{true})}{P(x|\mu_{best})}$, where x is the measured value, μ_{true} and μ_{best} are the true and best-fit value of the parameter μ respectively. We take $\chi^2 \sim -2lnR$. The procedure of F-C for finding the χ^2 value under a specific significance level, is to add values of measured x for a fixed μ to the interval with all other parameters varied within the known uncertainties following Gaussian fluctuations.

For this analysis, our measurables are $\sin^2 2\theta_{13}$ and δ_{cp}. In each bin of the $\sin^2 2\theta_{13}$ vs. δ_{cp} space, an suite of pseudo-experiments are generated that includes uncertainties in signal and background prediction, in the solar oscillation parameters, and in the atmospheric mass splitting ($\sin^2\theta_{23}$ is fixed at 0.5). Figure 9.12 shows the critical value χ^2 distribution in the oscillation phase space using LID selection and under normal mass hierarchy assumption for 68% confidential level (a) and 90% confidential level (b).

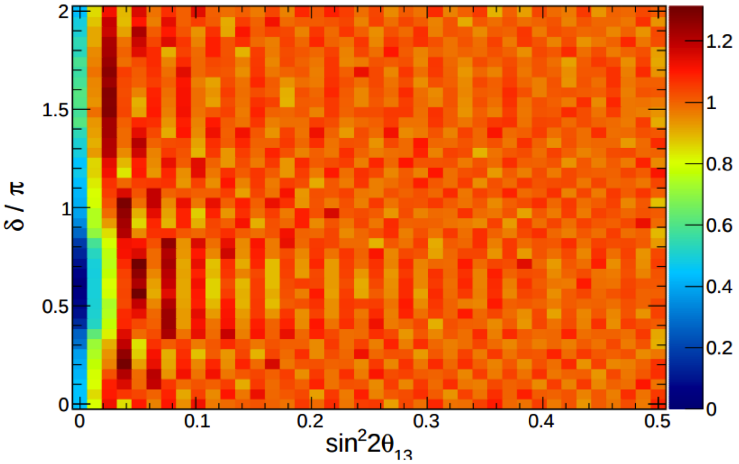

a 68% C.L.

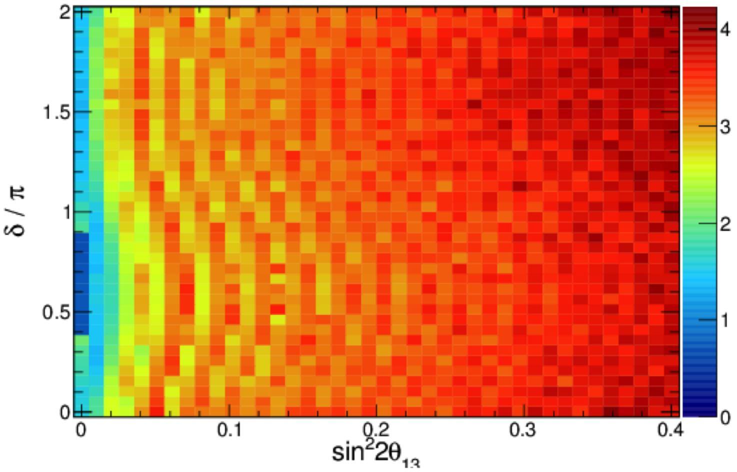

b 90% C.L.

FIG. 9.12: Critical value of χ^2 for 68% (a) and 90% (b) confidential level in $\sin^2 2\theta_{13}$ vs. δ space that calculated by Feldman-Cousins procedure under normal mass hierarchy assumption.

Figure 9.13 and 9.14 are the contours derived from the critical value distribution for LID and LEM, respectively, and compared to the reactor experiment results. For each PID selector, the contours are calculated for 68% and 90% confidence level under normal hierarchy (NH) and inverted hierarchy (IH). In Figure 9.13, the suggested value of $\sin^2 2\theta_{13}$ from Daya Bay reactor experiment shows good compatibility overall with the data from the primary selector LID. And Figure 9.14 shows the same plot for the secondary selector LEM, which is compatible with Daya Bay result in NH for certain δ_{cp} values at 90% C.L.

To take it a step further, we added the additional reactor constraint of $\sin^2 2\theta_{13} = 0.086 \pm 0.005$ and the uncertainty of $\sin^2 \theta_{23}$ to the F-C procedure during the generation of the pseudo-experiments. For every possible value of δ_{cp} in NH or IH, the likelihood ratio to the best-fit parameters is computed. Then the significance is presented from the F-C procedure as the fraction of pseudo-experiments that have a larger or equal likelihood ratio, as shown in Figure 9.15. The discontinuities are coming from the fact that the event counts are discrete. With the primary selector LID, NOνA's first measurement is compatible with the current oscillation models, and disfavor the range of $0.1\pi < \delta_{cp} < 0.5\pi$ in the IH at 90% C.L. For the secondary selector LEM, the whole δ_{cp} range in the IH, as well as $0.25\pi < \delta_{cp} < 0.95\pi$ in the NH are disfavored at 90% C.L.

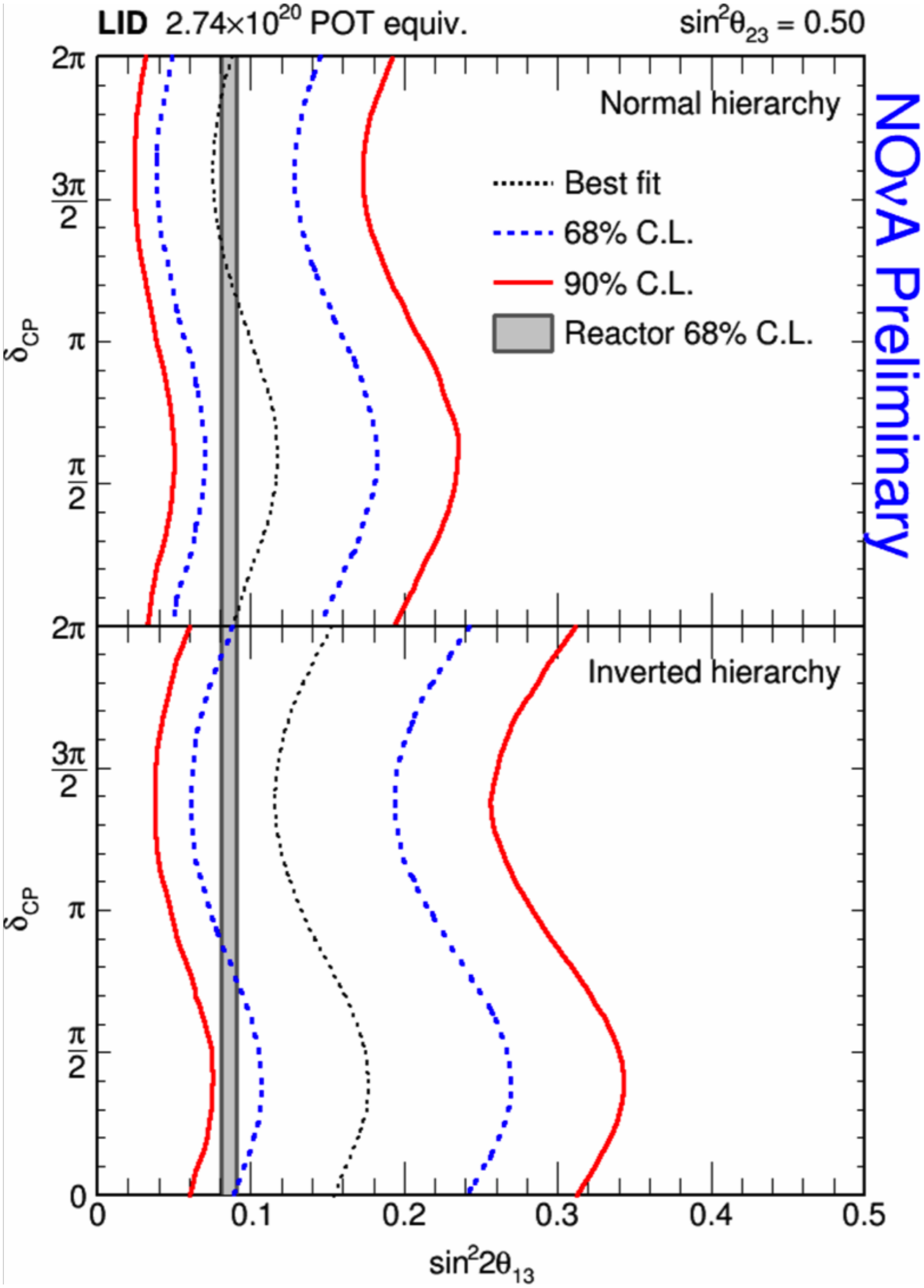

FIG. 9.13: LID candidates allowed values of δ_{cp} vs. $\sin^2 2\theta_{13}$ (black) and its confidence intervals at 68% (blue) and 90% (red). Grey area is the $\sin^2 2\theta_{13}$ result from Daya Bay at 68% confidence level. Top plot is for the normal mass hierarchy while the bottom one is for inverted mass hierarchy.

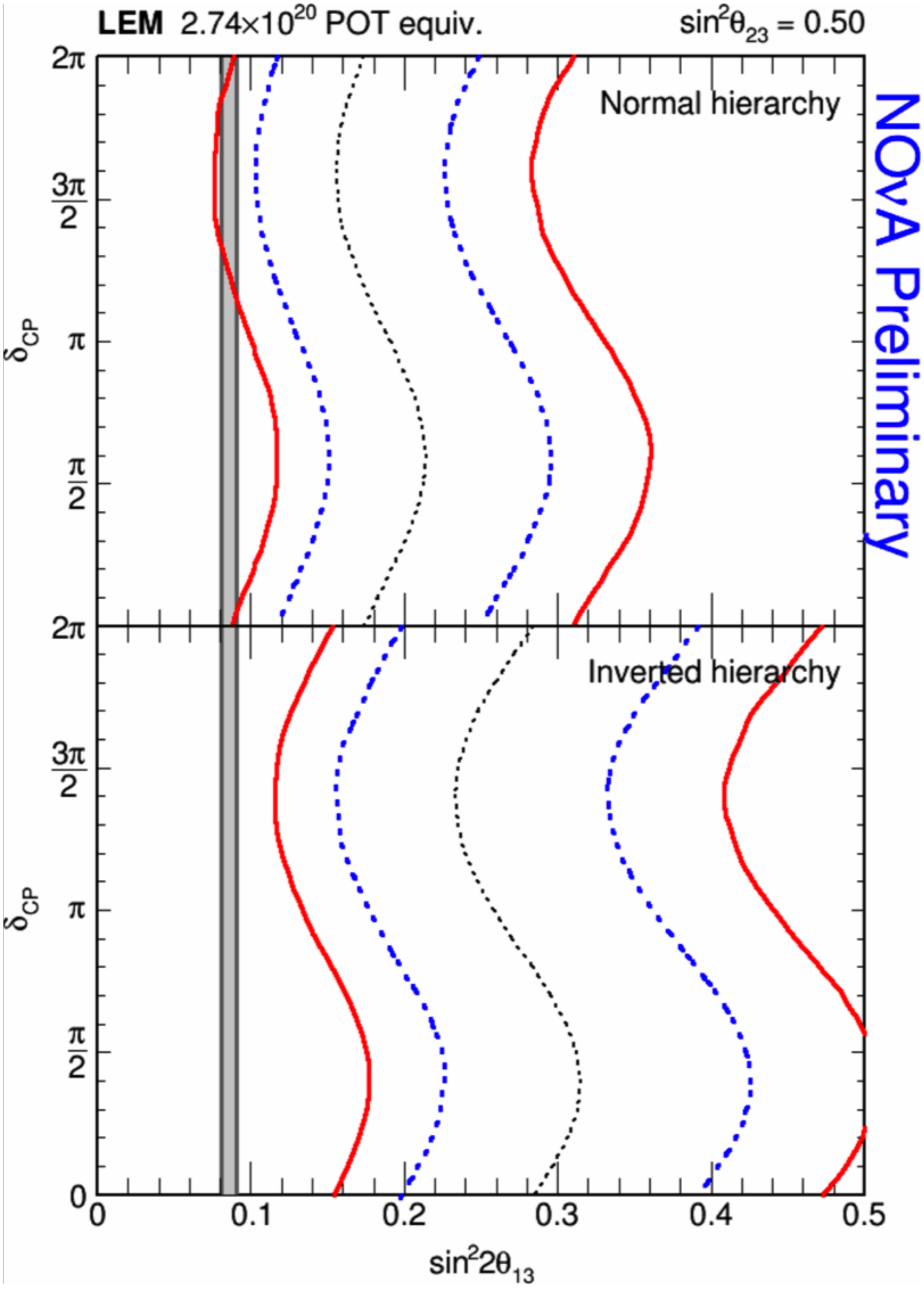

FIG. 9.14: LEM candidates allowed values of δ_{cp} vs. $\sin^2 2\theta_{13}$ (black) and its confidence intervals at 68% (blue) and 90% (red). Grey area is the $\sin^2 2\theta_{13}$ result from Daya Bay at 68% confidence level. Top plot is for the normal mass hierarchy while the bottom one is for inverted mass hierarchy.

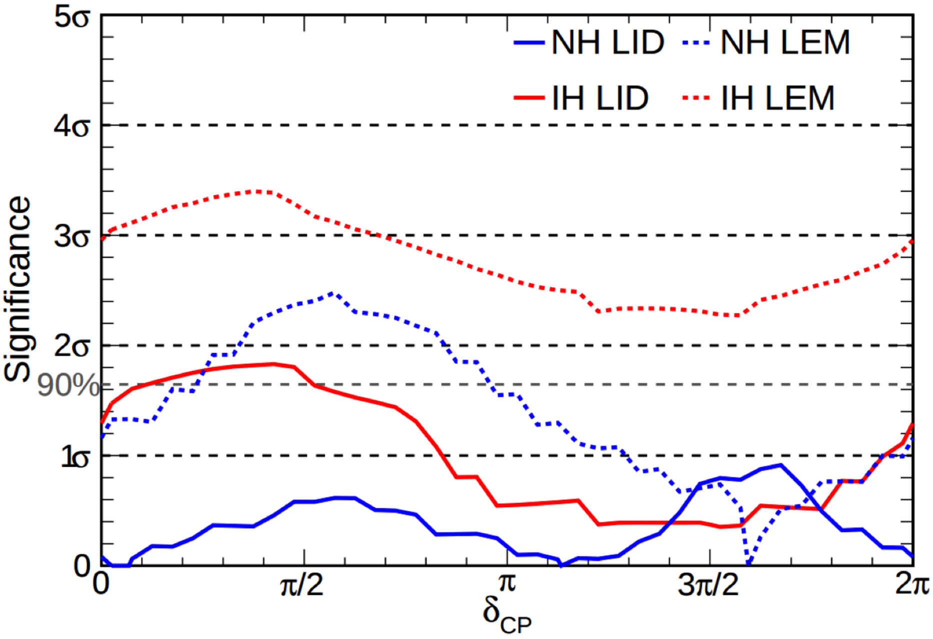

FIG. 9.15: Significance of the difference between the selected and the predicted event counts as a function of δ_{cp} for normal hierarchy (blue) and inverted hierarchy (red) in LID (solid) and LEM (dash).

9.3 Conclusion

This thesis presented the first ν_e appearance measurement in NOνA with an exposure of 2.74×10^{20} full detector equivalent POT collected from February, 2014 to May, 2015. The primary ν_e CC particle selection LID observes 6 ν_e-like events in the Far detector with a background prediction of 0.99 ± 0.11 (syst.), which corresponds to a 3.3σ excess over the no-oscillation hypothesis. The data show good compatibility with the current world-average θ_{13} result. By introducing the reactor constraint on θ_{13} to the analysis, this analysis disfavors $0.1\pi < \delta_{cp} < 0.5\pi$ in the inverted mass hierarchy at 90% C.L.

During the data collection of this analysis, both the Far detector construction and NUMI beam upgrades were ongoing. The exposure used in this analysis represents only about 8% of the total planned exposure for the NOνA experiment. With more exposure accumulated in future analyze, we can utilize the energy-related spectra to obtain more information from the data. Nevertheless, the first analysis contributes significantly to the future analysis by demonstrating the basic capability of NOνA in identifying the ν_e oscillation events and rejecting cosmic ray backgrounds.

BIBLIOGRAPHY

[1] C. Amsler et al. (Particle Data Group), Phys. Lett. **B667**, 1 (2008).

[2] K. A. Olive et al. (Particle Data Group), Chin. Phys. **C38**, 090001 (2014).

[3] S. Mufson et al, *Liquid scintillator production for the NOvA experiment*, NOνA internal docdb-13014.

[4] Evan Niner, *Position paper: nue high energy sideband*, NOνA internal docdb-13557.

[5] W. A. Mann, Int. J. Mod. Phys. **A15S1**, 229 (2000), `hep-ex/9912007`.

[6] URL `http://www.physik.uzh.ch/groups/serra/images/SM1.png`.

[7] G. P. Zeller et al. (NuTeV), Phys. Rev. Lett. **88**, 091802 (2002), [Erratum: Phys. Rev. Lett.90,239902(2003)], `hep-ex/0110059`.

[8] S. Materne et al., Nuclear Instruments and Methods in Physics Research Section A **611**, 176 (2009), particle Physics with Slow Neutrons.

[9] *Fundamental Physics at the Intensity Frontier* (2012), `1205.2671`, URL `https://inspirehep.net/record/1114323/files/arXiv:1205.2671.pdf`.

[10] URL `https://inspirehep.net/record/1368922/files/figures_mh.png`.

[11] URL `http://inspirehep.net/record/833934/files/numi.png`.

[12] Bob Zwaska, *Ph.D. Thesis.*

[13] The NOνA Technical Design Report (2007), `http://www-nova.fnal.gov/nova_cd2_review/tdr_oct_23/tdr.htm`.

[14] P. Adamson et al. (MINOS), Phys.Rev. **D77**, 072002 (2008), `0711.0769`.

[15] URL `https://inspirehep.net/record/1256324/files/map.png`.

[16] Chris Backhouse and Ryan Patterson, *Library event matching event classification algorithm for electron neutrino interactions in the nova detectors*, NOνA internal docdb-11869.

[17] Donald Friend and Ernest Villegas, *Near Detector Underground Assembly Layout*, NOνA internal docdb-8282.

[18] C. Andreopoulos, C. Barry, S. Dytman, H. Gallagher, T. Golan, R. Hatcher, G. Perdue, and J. Yarba (2015), `1510.05494`.

[19] Christopher Backhouse and Alexender Radovic, *Tech note: The Attenuation and Threshold*, NOνA internal docdb-13579.

[20] Michael Baird, *Tech note: Multi-Hough Transform*, NOνA internal docdb-8241.

[21] Evan Niner, *Position paper: nue extrapolation*, NOνA internal docdb-13585.

[22] Gavin S. Davies, *Position paper: Uncertainties for the ν_e Appearance First Analysis*, NOνA internal docdb-13597.

[23] Jeff Hartnell, *NOνA Light/ADC Levels and Thresholds*, NOνA internal docdb-13589.

[24] Evan Niner, *blessing: nue ks plots*, NOνA internal docdb-13807.

[25] W. Pauli, Camb. Monogr. Part. Phys. Nucl. Phys. Cosmol. **14**, 1 (2000).

[26] J. Chadwick, Proceedings of the Royal Society of London **A136**, 692 (1932).

[27] E. Fermi, Zeitschrift für Physik **88**, 161 (1934).

[28] H. Bethe and R. Peierls, Nature **133**, 532 (1934).

[29] F. Reines and C. L. Cowan, Nature **178**, 446 (1956).

[30] M. Goldhaber, L. Grodzins, and A. W. Sunyar, Phys. Rev. **109**, 1015 (1958).

[31] R. Davis, D. S. Harmer, and K. C. Hoffman, Phys. Rev. Lett. **20**, 1205 (1968).

[32] G. Danby, J.-M. Gaillard, K. Goulianos, L. M. Lederman, N. Mistry, M. Schwartz, and J. Steinberger, Phys. Rev. Lett. **9**, 36 (1962).

[33] F. J. Hasert et al. (Gargamelle Neutrino), Phys. Lett. **B46**, 121 (1973).

[34] M. L. Perl, G. S. Abrams, A. M. Boyarski, M. Breidenbach, D. D. Briggs, F. Bulos, W. Chinowsky, J. T. Dakin, G. J. Feldman, C. E. Friedberg, et al., Phys. Rev. Lett. **35**, 1489 (1975).

[35] K. Kodama et al. (DONUT), Phys. Lett. **B504**, 218 (2001).

[36] J. N. Bahcall, Phys. Rev. Lett. **12**, 300 (1964).

[37] B. T. Cleveland, T. Daily, J. Raymond Davis, J. R. Distel, K. Lande, C. K. Lee, P. S. Wildenhain, and J. Ullman, The Astrophysical Journal **496**, 505 (1998).

[38] J. N. Bahcall, M. H. Pinsonneault, and G. J. Wasserburg, Rev. Mod. Phys. **67**, 781 (1995), URL `http://link.aps.org/doi/10.1103/RevModPhys.67.781`.

[39] D. O. Gough, A. G. Kosovichev, J. Toomre, E. Anderson, H. M. Antia, S. Basu, B. Chaboyer, S. M. Chitre, J. Christensen-Dalsgaard, W. A. Dziembowski, et al., Science **272**, 1296 (1996), ISSN 0036-8075, `http://science.sciencemag.`

`org/content/272/5266/1296.full.pdf`, URL `http://science.sciencemag.org/content/272/5266/1296`.

[40] J. Christensen-Dalsgaard, W. Däppen, S. V. Ajukov, E. R. Anderson, H. M. Antia, S. Basu, V. A. Baturin, G. Berthomieu, B. Chaboyer, S. M. Chitre, et al., Science **272**, 1286 (1996), ISSN 0036-8075, `http://science.sciencemag.org/content/272/5266/1286.full.pdf`, URL `http://science.sciencemag.org/content/272/5266/1286`.

[41] K. S. Hirata et al. (Kamiokande-II), Phys. Rev. Lett. **63**, 16 (1989).

[42] P. Anselmann et al. (GALLEX), Phys. Lett. **B285**, 376 (1992).

[43] A. I. Abazov, O. L. Anosov, E. L. Faizov, V. N. Gavrin, A. V. Kalikhov, T. V. Knodel, I. I. Knyshenko, V. N. Kornoukhov, S. A. Mezentseva, I. N. Mirmov, et al., Phys. Rev. Lett. **67**, 3332 (1991).

[44] K. S. Hirata et al. (Kamiokande), Phys. Lett. **B205**, 416 (1988).

[45] R. Becker-Szendy, C. B. Bratton, D. Casper, S. T. Dye, W. Gajewski, M. Goldhaber, T. J. Haines, P. G. Halverson, D. Kielczewska, W. R. Kropp, et al. (IMB), Phys. Rev. D **46**, 3720 (1992).

[46] T. J. Haines, R. M. Bionta, G. Blewitt, C. B. Bratton, D. Casper, R. Claus, B. G. Cortez, S. Errede, G. W. Foster, W. Gajewski, et al., Phys. Rev. Lett. **57**, 1986 (1986), URL `http://link.aps.org/doi/10.1103/PhysRevLett.57.1986`.

[47] S. P. Mikheev and A. Yu. Smirnov, Sov. J. Nucl. Phys. **42**, 913 (1985), [Yad. Fiz.42,1441(1985)].

[48] L. Wolfenstein, Phys. Rev. **D17**, 2369 (1978).

[49] Q. R. Ahmad et al. (SNO), Phys. Rev. Lett. **89**, 011301 (2002), `nucl-ex/0204008`.

[50] Y. Fukuda et al. (Super-Kamiokande), Phys. Rev. Lett. **81**, 1562 (1998), `hep-ex/9807003`.

[51] M. H. Ahn et al. (K2K), Phys. Rev. **D74**, 072003 (2006), `hep-ex/0606032`.

[52] P. Adamson et al. (MINOS), Phys. Rev. Lett. **110**, 251801 (2013), `1304.6335`.

[53] P. W. Anderson, Phys. Rev. **130**, 439 (1963), URL `http://link.aps.org/doi/10.1103/PhysRev.130.439`.

[54] G. Aad et al. (ATLAS), Phys. Lett. **B716**, 1 (2012), `1207.7214`.

[55] J. H. Christenson, J. W. Cronin, V. L. Fitch, and R. Turlay, Phys. Rev. Lett. **13**, 138 (1964), URL `http://link.aps.org/doi/10.1103/PhysRevLett.13.138`.

[56] T. D. Lee and C.-N. Yang, Phys. Rev. **105**, 1671 (1957).

[57] B. Pontecorvo, Sov. Phys. JETP **7**, 172 (1958).

[58] Z. Maki, M. Nakagawa, and S. Sakata, Prog. Theor. Phys. **28**, 870 (1962).

[59] L. Stodolsky, Phys. Rev. **D58**, 036006 (1998), `hep-ph/9802387`.

[60] K. Eguchi, S. Enomoto, K. Furuno, J. Goldman, H. Hanada, H. Ikeda, K. Ikeda, K. Inoue, K. Ishihara, W. Itoh, et al. (KamLAND Collaboration), Phys. Rev. Lett. **90**, 021802 (2003), URL `http://link.aps.org/doi/10.1103/PhysRevLett.90.021802`.

[61] T. Araki et al. (KamLAND), Phys. Rev. Lett. **94**, 081801 (2005), `hep-ex/0406035`.

[62] S. Abe, T. Ebihara, S. Enomoto, K. Furuno, Y. Gando, K. Ichimura, H. Ikeda, K. Inoue, Y. Kibe, Y. Kishimoto, et al. (The KamLAND Collaboration), Phys. Rev. Lett.

100, 221803 (2008), URL `http://link.aps.org/doi/10.1103/PhysRevLett.100.221803`.

[63] F. P. An et al. (Daya Bay) (2015), `1505.03456`.

[64] M. H. Ahn et al. (K2K), Phys. Rev. **D74**, 072003 (2006), `hep-ex/0606032`.

[65] P. Adamson et al. (MINOS), Phys. Rev. Lett. **112**, 191801 (2014), `1403.0867`.

[66] S.-H. Seo, Nucl.Phys.Proc.Suppl. **237-238**, 65 (2013).

[67] Y. Abe et al. (Double Chooz), JHEP **10**, 086 (2014), [Erratum: JHEP02,074(2015)], `1406.7763`.

[68] S. E. Kopp (2005), `physics/0508001`.

[69] NUMI Technical Design Handbook (2002), `http://www-numi.fnal.gov/numwork/tdh/tdh_index.html`.

[70] R. M. Zwaska et al., IEEE Trans. Nucl. Sci. **50**, 1129 (2003), `hep-ex/0212011`.

[71] D. Indurthy, S. Kopp, M. Proga, and Z. Pavlovic, AIP Conf. Proc. **732**, 341 (2004), [,341(2004)], `physics/0405021`.

[72] P. Adamson et al., Nucl. Instrum. Meth. **A806**, 279 (2016), `1507.06690`.

[73] K. T. McDonald (2001), `hep-ex/0111033`.

[74] Alex Himmel., *The NuMI beam simulation with Flugg*, MINOS internal docdb-6316.

[75] G. Battistoni, S. Muraro, P. R. Sala, F. Cerutti, A. Ferrari, S. Roesler, A. Fasso, and J. Ranft, AIP Conf. Proc. **896**, 31 (2007).

[76] C. Andreopoulos et al., Nucl. Instrum. Meth. **A614**, 87 (2010), `0905.2517`.

[77] Jerome Verbeke and others, *Cosmic-ray Shower Library (CRY)*, `http://nuclear.llnl.gov/simulation/doc_cry_v1.7/cry.pdf.`

[78] S. Agostinelli et al. (GEANT4), Nucl. Instrum. Meth. **A506**, 250 (2003).

[79] J. T. Sobczyk, AIP Conf. Proc. **1405**, 59 (2011), `1108.0506`.

[80] T. Yang, C. Andreopoulos, H. Gallagher, K. Hoffmann, and P. Kehayias, Eur. Phys. J. **C63**, 1 (2009), `0904.4043`.

[81] L. Popova and G. Kamberov, Nuclear Physics B - Proceedings Supplements **75**, 287 (1999), ISSN 0920-5632, URL `http://www.sciencedirect.com/science/article/pii/S0920563299002686`.

[82] T. Sjostrand, S. Mrenna, and P. Z. Skands, JHEP **05**, 026 (2006), `hep-ph/0603175`.

[83] Luke Vinton, *Tech note: Calorimetric Energy Scale Calibration*, NOνA internal docdb-13579.

[84] Evan Niner, *Tech note: Timing Calibration*, NOνA internal docdb-13579.

[85] Michael Baird, *Tech note: Slicing Module*, NOνA internal docdb-9195.

[86] Mark Messier, *Tech note: Elastic Arms*, NOνA internal docdb-7530.

[87] Evan Niner, *Tech note: FuzzyK Vertex*, NOνA internal docdb-7648.

[88] Michael Baird, *Ph.D. Thesis*, NOνA internal docdb-14249.

[89] Evan Niner, *Ph.D. Thesis*, NOνA internal docdb-13902.

[90] Joao Coelho and Barnali Chowdhury, *Tech note: Good data selection*, NOνA internal docdb-13546.

[91] Tian Xin and Jianming Bian, *Tech note: Selection Cuts for* ν_e *Appearance Analysis*, NOνA internal docdb-13592.

[92] Jianming Bian, Kanika Sachdev and Evan Niner, *Tech note: Likelihood-based* ν_e *Identifier (LID)*, NOνA internal docdb-13590.

[93] Christopher Backhouse, *Tech note: The Library Event Matching* ν_e *PID*, NOνA internal docdb-13588.

[94] Evan Niner, *Position paper: Far Detector Exposure Accounting*, NOνA internal docdb-13556.

[95] Hongyue Duyang and others, *Tech note: Cosmic and Rock Muon-Induced EM Shower*, NOνA internal docdb-13594.

[96] Alexander Radovic et al., *Tech note: The Derivation and Size of NuMI Flux Uncertainties Used in the First NO*ν*A Analyses*, NOνA internal docdb-13584.

[97] Sarah R. Phan-Budd and Lisa Goodenough, *Tech note: NO*ν*A Beam Monitoring*, NOνA internal docdb-13572.

[98] C. N. Chou, Phys. Rev. **87**, 904 (1952), URL `http://link.aps.org/doi/10.1103/PhysRev.87.904`.

[99] V. I. Tretyak, Astropart. Phys. **33**, 40 (2010), `0911.3041`.

[100] Chris Backhouse, *NO*ν*A Light-leven/Hit-efficient Systematics*, NOνA internal docdb-13686.

[101] Ji Liu, *NO*ν*A Rock Muon*, NOνA internal docdb-13563.

[102] Hongyue Duyang et al., *Tech note: The derivation and size of NUMI flux uncertainties used in the first NO*ν*A analyse*, NOνA internal docdb-13584.

[103] Nicholas Raddatz, *Tech note: Fiducial mass systematic*, NOνA internal docdb-13237.

[104] G. J. Feldman and R. D. Cousins, Phys. Rev. D **57**, 3873 (1998), URL `http://link.aps.org/doi/10.1103/PhysRevD.57.3873`.